PB81-120800

Feasibility Study for an Asbestos Aerosol Monitor

Vermont Univ.
Burlington

Prepared for

Environmental Sciences Research Lab.
Research Triangle Park, NC

Dec 80

U.S. Department of Commerce
National Technical Information Service
NTIS

TECHNICAL REPORT DATA

(Please read Instructions on the reverse before completing)

1. REPORT NO. EPA-600/2-80-200	2.	3. RECIPIENT'S ACCESSION NO. PB81 120800
4. TITLE AND SUBTITLE FEASIBILITY STUDY FOR AN ASBESTOS AEROSOL MONITOR		5. REPORT DATE December 1980 Issuing Date. 6. PERFORMING ORGANIZATION CODE
7. AUTHOR(S) Robert W. Detenbeck		8. PERFORMING ORGANIZATION REPORT NO.
9. PERFORMING ORGANIZATION NAME AND ADDRESS Physics Department University of Vermont Burlington, VT 05405		10. PROGRAM ELEMENT NO. 1AD712 BA-32 (FY-79) 11. CONTRACT/GRANT NO. R804562
12. SPONSORING AGENCY NAME AND ADDRESS Environmental Sciences Research Laboratory - RTP, N.C. Office of Research and Development U. S. Environmental Protection Agency Research Triangle Park, N. C. 27711		13. TYPE OF REPORT AND PERIOD COVERED Final 7/76 - 6/78 14. SPONSORING AGENCY CODE EPA/600/09

15. SUPPLEMENTARY NOTES

16. ABSTRACT

The feasibility of discriminating and counting asbestos-fiber aerosol particles by means of their shapes, using a two-detector, optical, aerosol counter was determined. The assymmetry of their optical diffraction patterns would distinguish fibers from other, more regular aerosol particles. A laboratory prototype was designed, constructed, tested, modified and retested. The feasibility of counting fibers by means of their optical diffraction patterns, using two detectors, was demonstrated. In the latest version the aerosol fibers were aligned by a combination of fluid-velocity-gradient and electric fields. A description of the latest version, its capabilities and limitations, and a theoretical model of the alignment process are presented.

17. KEY WORDS AND DOCUMENT ANALYSIS

a. DESCRIPTORS	b. IDENTIFIERS/OPEN ENDED TERMS	c. COSATI Field/Group
Air pollution Aerosols *Asbestos *Monitors Development Light scattering Diffraction	Chrysotile	13B 07D 11E 20N 20F

18. DISTRIBUTION STATEMENT RELEASE TO PUBLIC	19. SECURITY CLASS *(This Report)* UNCLASSIFIED	21. NO. OF PAGES 143
	20. SECURITY CLASS *(This page)* UNCLASSIFIED	22. PRICE

EPA Form 2220-1 (Rev. 4-77) PREVIOUS EDITION IS OBSOLETE

PB81-120800

EPA-600/2-80-200
December 1980

FEASIBILITY STUDY FOR AN ASBESTOS AEROSOL MONITOR

by

Robert W. Detenbeck
Physics Department-Cook Building-A405
University of Vermont
Burlington, Vermont 05405

Grant No. R-804562

Project Officer

Jack Wagman
Emissions Measurement and Characterization Division
Environmental Sciences Research Laboratory
Research Triangle Park, North Carolina 27711

ENVIRONMENTAL SCIENCES RESEARCH LABORATORY
OFFICE OF RESEARCH AND DEVELOPMENT
U. S. ENVIRONMENTAL PROTECTION AGENCY
RESEARCH TRIANGLE PARK, N. C. 27711

REPRODUCED BY
NATIONAL TECHNICAL
INFORMATION SERVICE
U.S. DEPARTMENT OF COMMERCE
SPRINGFIELD, VA 22161

DISCLAIMER

This report has been reviewed by the Environmental Sciences Research Laboratory, U.S. Environmental Protection Agency, and approved for publication. Approval does not signify that the contents necessarily reflect the views and policies of the U.S. Environmental Protection Agency, nor does mention of trade names or commercial products constitute endorsement or recommendation for use.

FOREWARD

Airborne fibers, whether natural or man-made, have been of concern because of the possible risks they may pose to occupational and public health. In the case of asbestos, occupational exposures have been found to induce mesothelioma of the pleura and peritoneum, as well as cancer of the lung after latent periods of about 20 to 40 years.

The Environmental Sciences Research Laboratory has conducted a comprehensive program to advance the state-of-the-art of asbestos fiber detection and measurement. One of the major studies in this program has produced a provisional optimum electron microscope procedure for use as a research or reference method (EPA Report 600/2-77-178, June 1978). Another project has demonstrated the feasibility of a new x-ray diffraction method with a potential for about a ten-fold cost savings over electron microscopy (EPA Report 600/2-78-194, August 1978).

This report describes a research project to design, fabricate and test an instrument capable of real-time continuous monitoring of airborne asbestos fibers. This type of instrument should be a useful tool for rapid screening and problem assessment, and for verifying the effectiveness of emission control measures.

Alfred H. Ellison
Director
Environmental Sciences
  Research Laboratory
Research Triangle Park, N. C.

ABSTRACT

This research project was initiated to determine the feasibility of discriminating and counting asbestos-fiber aerosol particles by means of their shapes, using a two-detector, optical, aerosol counter. The asymmetry of their optical diffraction patterns would distinguish fibers from other, more regular aerosol particles. A laboratory prototype was designed, constructed, tested, modified and retested. The feasibility of counting fibers by means of their optical diffraction patterns, using two detectors, was demonstrated. In the latest version the aerosol fibers were aligned by a combination of fluid-velocity-gradient and electric fields. A description of the latest version, its capabilities and limitations, and a theoretical model of the alignment process are presented in this report. Only the beginnings of tests of this version under controlled conditions had been made by the end of the project period.

This report was submitted in fulfillment of Grant R-804562 by the University of Vermont under the partial sponsorship of the U. S. Environmental Protection Agency. This report covers a period from July 1, 1976, to June 30, 1978, and the experimental work was completed as of June 30, 1978. The theoretical model was developed during the writing of this report, after the project period.

TABLE OF CONTENTS

FOREWARD iii

ABSTRACT iv

FIGURES vi

ACKNOWLEDGMENT vii

SECTIONS

1. INTRODUCTION 1
2. CONCLUSIONS 4
3. RECOMMENDATIONS 8
4. THE DEVICE 12
    - GENERAL PRINCIPLES 12
    - AIRFLOW 19
    - LIGHT SOURCE 30
    - PHOTODETECTORS AND PHOTON-COUNTING INTERFACE 38
    - DATA PROCESSING 45
5. THEORETICAL BACKGROUND 55
    - ALIGNMENT OF FIBERS 55
    - LIGHT SCATTERING AND PARTICLE DIMENSIONS 71
6. TESTING 83

REFERENCES AND FOOTNOTES 100

APPENDICES 107

A. THE IMITATION OF A FIBER BY TWO SPHERES 108

B. A TEST OF FAYLEIGH-GANS-DEBYE THEORY 118

FIGURES

Number Page

1. Diffraction pattern of a fibrous aerosol particle 13
2. The two-detector fiber counter 13
3. Simplified diagram of the airflow system 14
4. Scattering geometry for two detectors 14
5. Aerosol-sampling head 16
6. Block diagram of photon counters. 16
7. The microcomputer and interface 18
8. Data printout 18
9. Airflow system 20
10. Geometry in the region of the sample volume 21
11. Fluid velocity in the sample inlet and sheath tubes 23
12. Scattering geometry in an aerosol counter. 31
13. Laser light source 35
14. Photomultiplier-tube mount 39
15. Photon-counting interface 41
16. Flow chart of fiber-counting program. 47
17. Flow chart of calibration program 52
18. Map of memory allocations 54
19. Orientation of a fiber 57
20. Geometry of combined viscous and electric torques 62
21. Competition of viscous and electric torques 64
22. Fractional alignment of dielectric spheroids 67
23. Fractional alignment of conducting spheroids 68
24. Three spheroids 73
25. Scattering from a spheroid 73
26. Comparison of RGD and Mie scattering for a sphere 76
27. The (length, diameter) plane for model fibers 79
28. Size thresholds for model fibers 82
29. Temporal decay of particle count in aerosol-storage chamber 85
30. Vibrating-bed, dry aerosol generator 87
31. SEM photograph of Rhodesian chrysotile sample 89
32. Pulse-height distributions from latex spheres 92
33. Distribution of intensity ratios for latex spheres 93
34. Distributions of temporal widths of light pulses. 95
35. Fiber-counting efficiency (alignment) *vs* high voltage . . . 97

ACKNOWLEDGMENT

The airflow systems for aerosol generation and sampling were largely the work of the Co-Investigator on this project, Dr. David R. Hemenway of the Department of Civil Engineering at the University of Vermont (UVM).

The exact numerical calculations in Appendix B were carried out by Dr. Cavour Yeh of EMtec Engineering, Inc., and the University of California at Los Angeles. He also provided a critical reading and discussion of Appendix B.

The idea of using the inlet and outlet tubes as electrodes for the alignment field came from Dr. Malcolm Whatley (Department of Physics, UVM), who also provided valuable discussions and criticisms of the analysis of the combined flow and electric-field alignment of the fibers.

Dr. James Chlipala (Department of Physics, UVM) provided the initial versions of several of the microcomputer routines for data recording and analysis.

The Academic Computing Center of UVM provided partial support for numerical computations used in this research. The Department of Physics of UVM provided partial support for machine-shop services.

The Project Director gratefully acknowledges generous hospitality and computer support from the Department of Atmospheric Science, State University of New York at Albany (SUNYA), while he was there on sabbatical leave, preparing an initial joint proposal for this research. Many contributions of Mr. Frank Giovane and Dr. J. Mayo Greenberg of the Dudley Observatory and SUNYA remained in the final version of the proposal from UVM alone.

SECTION 1

INTRODUCTION

Airborne, respirable asbestos fibers are known to constitute a health hazard to human beings. Therefore, there exists a need for a means of monitoring the concentration of asbestos-fiber aerosols, in environments where the potential for such a hazard exists.

This report describes a study of the feasibility of using one type of asbestos-fiber-aerosol monitor. The fibrous aerosol monitor under study is characterized by (a) a continuous sampling of the ambient air; (b) passage of the sampled air through a small sensitive volume, illuminated by an intense beam of light; (c) alignment of fibrous aerosol particles in the sensitive volume by a combination of flow-velocity-gradient and electric fields; (d) simultaneous measurements of the pulses of light scattered in different directions, when an aerosol particle traverses the sensitive volume, by two or more photo-multiplier tubes; (e) classification of each particle as a fiber or nonfiber on the basis of the ratios of intensities of light scattered in different directions; and (f) display of the current fiber concentration with only a few seconds delay. The device described here would detect fibers with a reduced counting efficiency if they were randomly aligned, and the original proposal was to do so. However, it was discovered late in the project period that the combination of flow and electric-field alignment was both effective and convenient, and it offers enormous advantages in interpreting the data produced by the instrument, as well as greatly increased efficiency in counting fibers.

The reader may be familiar with another fibrous aerosol monitor, the GCA/Scientific Model FAM-1, developed more or less contemporaneously under a NIOSH contract (1). The two devices, developed independently to serve similar functions, are descended historically from different initial ideas. The GCA instrument evolved from a fiber-rotation method (1), and the UVM (University of Vermont) device described here evolved from a light-scattering method for randomly-oriented particles (2). Although the functions of the current versions of both devices are similar, each has its own advantages and disadvantages.

It is already clear from the description above that a light-scattering fibrous aerosol monitor counts all types of fibers in the appropriate size range, and not only asbestos. Therefore, it can give conclusive zero readings, but a positive fiber count might be due to any fiber. Given the state of knowledge about the mechanisms of asbestos pathology, it would be wise to treat any fiber, such as fiberglass (3, 4), of respirable dimensions with caution. Because the light-scattering fibrous aerosol monitor is nonspecific, however, it will be used mainly in situations where there is an *a priori* reason to suspect the presence of a particular kind of fiber, or where the detailed identification of fibrous aerosols as asbestos, glass, etc. can be carried out by other means. At present these "other means" involve collecting samples on filters and subjecting the filters to tedious preparation and examination procedures with a phase-contrast-optical or electron microscope. The nearly continuous readings of a real-time fiber counter, such as the one described herein, can be used as an alarm to trigger more detailed analytical procedures, which are too slow and expensive for routine use in continuous monitoring. Of course, where a potential asbestos hazard, such as a possible filter leakage, is known to exist, some sort of immediate warning is a necessity. In such cases a fiber counter is a great improvement in selectivity over a conventional aerosol-particle counter.

By its very nature an optical fiber counter can operate properly only within a certain range of particle sizes and concentrations. If the particles are too small, the instrument may not be sufficiently sensitive to detect them. If they are too large, they may overload the instrument or be mechanically trapped in the inlet. Low fiber concentrations may take too long to measure, depending upon the instrument's air-sampling rate. High dust concentrations may cause coincidence errors when two particles are in the sensitive volume simultaneously. Measurements of low fiber concentrations in high background concentrations of amorphous dust are doubly difficult. This study, and the design of the resulting fiber counter, have been aimed at extending the lower limit of reliably detectable fiber sizes, and at detecting small numbers of fibers among much larger numbers of background dust particles.

Certain quantitative characteristics of each aerosol particle are measured directly by a multiple-detector, light-scattering counter of the type described in the report. Briefly, they are intensities, and ratios of intensities, of light scattered in selected directions. With some reservations and assumptions, discussed in the report, these can be interpreted in terms of the dimensions (sizes and shapes) of the particles. In addition to a separation into fibers and nonfibers, measurement and display of the distribution of fiber volumes seems to be feasible with this instrument.

In the body of the report attempts are made to distinguish between those fundamental limits of performance determined by the basic method of measurement, and the accidental limits of performance determined by particular design choices in the present instrument. The conclusions in Section 2 present a quick progress report of what has been achieved in the initial tests of the most recent design, although it must be emphasized that the tests are still quite incomplete.

The UVM device described in this report grew out of a line of basic research not originally related to asbestos. The author had already for several years been interested in multiple-point intensity correlations in the light scattered from aspherical particles, when he applied for and received an exploratory grant, AP-01263 from the National Air Pollution Control Administration (DHEW), for an automatic means of monitoring the average shape properties of an aerosol. This grant was continued under the Environmental Protection Agency as R-800864, ending in the summer of 1973. By that time, it had become clear that a counter to monitor airborne asbestos fibers was a national need. This meant a change in approach, because it required the selection of a few fibrous particles out of a much more numerous aerosol background, but it built upon the previous results (2). A joint proposal was submitted in 1974 by the University of Vermont and the Dudley Observatory of Albany, New York, for the development of "An Automatic Monitor for Airborne Asbestos Fibers", to a large number of federal agencies. The Environmental Protection Agency responded with a suggestion for a feasibility study, but by that time the Dudley Observatory had withdrawn. This report gives the results of a feasibility study by the University of Vermont during the period 7/1/76-6/30/78 funded by EPA Grant R-804562.

SECTION 2

CONCLUSIONS

A device that discriminates and counts airborne asbestos fibers in a more numerous background of amorphous aerosol particles has been constructed and operated successfully. Its operation demonstrates the feasibility of using simultaneous measurements of the light scattered in two different directions by an aerosol particle to differentiate between fibers and more symmetrically shaped respirable particles.

The UVM device samples the ambient air at a rate of 5 cm^3/sec. (.01 CFM). At this rate a fiber counter can measure the OSHA Threshold Limit Value (TLV) of 2 fibers/cm^3 (5) to 10 percent accuracy in 10 seconds. In the UVM device the sensitive volume, within which a fiber is counted, is about 1 mm^3. Therefore, the background dust concentration can be as high as 100 total particles/cm^3 before coincidence errors reach 10 percent. The electronic dead time of the UVM instrument, associated with analyzing each particle's shape, is in the range 1-5 msec (depending on the amount of output data requested). The dead time introduces no counting errors, because the total clock time is increased for a given sampling time in order to compensate for it. For the case described above, the 100 particle/cm^3 background might lengthen the clock time for the measurement to 30 seconds. As a worst case example: the instrument could measure the low concentration of 0.02 fibers/cm^3 in a background of 100 nonfibrous particles/cm^3 to about 15% accuracy in a one-hour measurement. Several methods of decreasing the coincidence error rate at high background dust concentrations are discussed in the report.

This study, and the design of the resulting fiber counter, were aimed at extending the lower limit of reliably detectable fiber sizes well below the limits of practical optical microscopy, 5 micrometer minimum length and 0.5 micrometer minimum diameter (6), in the membrane-filter method specified in the OSHA-TLV (5). The minimum detectable fiber size for the UVM instrument is limited by signal to noise considerations, related to the background scattered light when there are no aerosol particles. In the proposal it was estimated that one could achieve a minimum-detectable-fiber volume of 0.02 μm^3. Despite a long battle against background light, it has been possible so far to achieve reliable fiber discrimination only down to a volume of 0.06 μm^3. For a cylinder of 5 μm length, this corresponds to a diameter of slightly over 0.1 μm. The tests of the UVM device were made with a choice of scattering angle that selected fibers having lengths exceeding 2 μm, for which length this volume sensitivity corresponds to a diameter of about 0.2 μm. A modest improvement in the minimum volume detectable with the present instrument may be possible merely by selecting a large scattering angle (appropriate to fibers of shorter lengths), where the background light will be less. The project terminated before this could be tried. Background light will probably always remain the major impediment to detecting fibers of very small volume, with the principle used in the UVM instrument. Nevertheless, a scattering chamber redesigned to minimize background light, rather than the ease of making changes and adjustments emphasized in the present version, should permit achieving the minimum fiber volume of 0.02 μm^3 originally proposed, on the basis of Rayleigh scattering from the 1 mm^3 of air in the sensitive volume. A further improvement would follow from reducing the scattering volume and carefully restricting the fields of view of the light detectors.

The present version of the UVM fiber counter is limited by its electronics to a maximum intensity of scattered light. The resulting limitation on maximum fiber size is not fixed, but rather one of the range of sizes ("dynamic range") measurable at one time with the present photodetector-microcomputer interface circuits. The present design served well in the struggle to measure small fibers, because it is so flexible. However, we have only recently begun to appreciate the practical implications of the fact, that the scattered light intensity at the forward scattering angles used in this instrument varies much more widely with particle volume for fibers than it does for spheres. Even if the dynamic range of light intensities for the present interface is optimized by electronic or optical changes, it will likely be inadequate. Either multiple ranges, or (much better) an interface with a logarithmic response to light intensity, will be required to cover an adequate range of fiber sizes.

The present version of the UVM instrument was tested with aerosols made from a sample of UICC Rhodesian chrysotile (7). The concentration of particles ranged from 0-100/cm^3. About 35 percent of the total particles over a given threshold size in this aerosol were classified as "fibers" by the device. It is not known just what fraction of these chrysotile particles actually deserved to be classified as "fibers", but the fraction is probably somewhat larger than 35 percent. The discrepancy is attributed largely to the limited dynamic range of the present device; many fibers were too large to be classified properly at the high sensitivity setting used in those measurements. Unfortunately, the termination of the grant period did not allow time to explore the significance and possible improvement of the dynamic range. Whether there is a reduction of fiber-counting efficiency for chrysotile in particular, because of the curly fiber shape, was not answered because the large fibers could not be handled properly. They are the ones most likely to be curly.

The present instrument seems to discriminate adequately against latex spheres, common room dust, chalk dust, and cigarette smoke, but an inadequate number of quantitative tests have been completed to permit a definitive statement. It is especially sensitive to asbestos fibers, both in the controlled test chamber and in the open air near asbestos samples in the laboratory. It does, however, also display a sensitivity to any needlelike particles, including some commonly found in the laboratory. In the laboratory at UVM the background fiber count seems to hover about 0.02/cm^3, despite the fact that truly clean air, or an aerosol of latex spheres, gives exactly zero fiber count, to the limit of the experimenter's patience. Theoretically, a device using this light-scattering principle should also have some counting efficiency for thin, flat flakes (or very oblate spheroids), but it has not yet been possible to find a test sample of such material that is completely free of a few long, prismatic flakes, that look like "fibers" both to the counter and under a scanning electron microscope.

Several aspects of the UVM instrument were not adequately foreseen in the proposal. First, the scattering geometry of this method of fiber discrimination makes the instrument awkwardly sensitive to background light in the scattering chamber. As a result, the instrumental design was changed in the last six months of the project, to use a laser rather than an incandescent light source. This introduced the possibility of some complications, which are dealt with in Appendix A. Second, as soon as the device was working properly with the new light source, it became obvious that the fibers were exhibiting a strong preferential alignment in the sampling volume due to the airflow alone. Addition of an electric field strengthened this preferential alignment to essentially 100 percent, along the direction of flow. Whereas the proposal had merely suggested that the counting efficiency of the device, which could work with randomly oriented particles, might be increased by proper use of flow and electric fields, the final configuration, which evolved in the last few weeks of the project period, is dominated by the reinforcement of these two effects.

The alignment of the aerosol fibers within the sensitive volume, by a combination of flow and electric fields, has added a new dimension to the measuring capabilities of the instrument. At least for an ideal cylindrical fiber, the light beam is incident from a direction perpendicular to the axis of the fiber. Also, the two photomultipliers determine the scattered light intensity in an especially simple geometry. For this geometry, and for sufficiently thin fibers, the light intensity in the brighter detector is proportional to the square of the fiber volume. The proper theoretical restrictions about "how thin, how long, how straight," etc., have not been worked out completely. Nevertheless, it appears possible to obtain a distribution of fiber sizes from the instrument, as well as a simple fiber count. Because this would not have been possible for randomly oriented fibers, as originally proposed and expected until the end of the project period, the details of this possibility have not yet been adequately explored.

SECTION 3

RECOMMENDATIONS

Quantitative measurements of every optical fiber counter's response to aerosols of varying shapes, sizes and concentrations are the most important recommendations of this section. Some minor modifications of the UVM instrument should precede or accompany these tests. A better theoretical understanding of the light scattering from curly chrysotile fibers is called for. Theoretical and experimental investigations of the UVM instrument's measurements of fiber size (volume?) are recommended.

Both the UVM and GCA fiber counters should be evaluated for their contributions to an optimum solution to the problem of monitoring hazardous fibrous aerosol particles in real time, in a background of other dust. In addition to a reliable and physically well-defined discrimination between fibers and nonfibers, the optimum device would provide as much additional information as feasible, in order to characterize the fibrous component of the aerosol. It would operate in a wide range of ambient conditions: temperature, humidity, transportation, background dust (nature and concentration) and fiber sizes and shapes.

The range of dimensions of fibers detected by an optimum monitor would include not only the "long and thin" fibers currently believed to be most active pathogenically (8, 9), but also as many as feasible of the smaller fibers, which can be present in even larger numbers and may also be hazardous (10). Without meaning to imply the existence of a sharp cutoff, one can define the "long and thin" fibers as having lengths L exceeding 5 μm and diameters D less than 0.5 μm. It would seem reasonable to expect to count fibers with diameters

$$D > 0.1\ \mu m,$$

but it is probably too optimistic to hope to count chrysotile fibrils, which may have diameters down to 0.02 μm, by any optical means. Although the capabilities of the present instrument are implied to achieve the here-proposed, 0.1 μm diameter, practical limit for fibers longer than 5 μm, they still need to be improved for shorter fibers by decreasing the background light. Also, the changes which will extend the dynamic range of fiber sizes measurable at one instrument setting should be made. With the consequent ability to count both small and large fibers, the problems associated with the longer, curly chrysotile fibers should be dealt with.

The problem of interpreting the light scattering from curly chrysotile fibers will occur with any optical fiber counter. Most fibers have been modeled as simple cylindrical rods, or very elongated prolate spheroids, in scattering calculations. For many realistic fiber shapes this may be adequate, if the corrections are likely to be merely a small percentage difference between the measured fiber length or diameter and a corresponding dimension of the real fiber. However, the difference between a straight and curly fiber may affect the qualitative operation of an optical fiber counter. Although little theoretical guidance is available, it has been found in practice (1) that the GCA Model FAM-1 must use quite different settings in order to count chrysotile asbestos with full efficiency. It is likely that there will be some curly-fiber effect on the counting efficiency of the UVM instrument as well, but the available data set only a limit: the chrysotile fiber-counting efficiency certainly exceeds 35 percent. So little is known about the scattering from curly fibers that even a few theoretical calculations would provide some useful guidance. The fibers in question are many wavelengths long, despite their small diameters, and one would hesitate to use approximate methods of calculation without tests against either selected experiments or more detailed numerical calculations. Fortunately, several techniques currently in use for predicting the scattering of light by irregularly shaped particles appear promising for these tests. These include the finite-element (11) and Purcell-Pennypacker (12, 13) theoretical techniques, and microwave-analog experimental techniques (14, 15).

The ability of a fiber counter to discriminate against false fiber counts from nonfibrous background dusts needs to be established by quantitative tests, in order to establish the reliable operating limits of the instrument. The number of variable parameters in real aerosols is too large to permit detailed calculations of all the things that might lead to false fiber counts. However, two cases are especially likely to give trouble. The first case is high dust concentrations, which will be especially troublesome when most of the particles are too small to be detected individually. The probability of twofold coincidence errors leading to false fiber counts is estimated in Appendix A, but more complicated effects should be searched for experimentally, before a large effort is expended upon explaining them. The second case likely to yield false fiber counts is asymmetric particles which are still not fibers. This case was recognized in the original proposal, where it was pointed out that for certain orientations oblate spheroids (disks) might mimic the light-scattering signatures of prolate spheroids (needles). The preliminary tests of the instrument pointed out that, for realistic mineral aerosols containing particles with a range of shapes, the distinction between disks and needles is likely to be academic. Nevertheless, the question of whether biologically innocuous aerosols of irregularly shaped particles give significant numbers of fiber counts needs to be studied quantitatively and experimentally.

It is also possible that high concentrations of background dust could cause a loss of true fiber counts. Although twofold-coincidence losses can be estimated from the single-particle count rates, higher-order losses (including the possibility of complete paralysis) due to very large numbers of individually undetectable particles, need to be studied experimentally. It is known that these losses can be serious for both the GCA (1) and UVM instruments, and one must be certain that they do not occur without a noticeable warning from the device. Probably a nephelometric analog measurement of photomultiplier current is an adequate indicator of this form of overload, especially if it triggers a warning signal.

A hand-portable optical fiber counter would permit one to take full advantage of its ability to provide data in real time. The UVM device could be engineered into a portable package giving a simple fiber count, like the GCA/Scientific Model FAM-1. However, the desire for a more detailed knowledge of aerosol characteristics, such as a size distribution, is likely to conflict with the desire for small size and power requirements. Various compromises will be appropriate for different situations. If an instrument is to be portable, it must be at least moderately rugged, with respect to both breakage and stability of critical adjustments. Excepting the printer, the most fragile components in the UVM fiber counter are the phototubes and the laser. The most critical adjustment is the aiming of the laser beam to intersect the sampling airstream. With proper attention to these areas, a quite rugged portable instrument could be designed.

A portable monitor should operate properly over the ranges of temperature and humidity where people are likely to be found. The humidity limits for the UVM instrument, since it does not rely upon surface conductivity of the fibers, extend from zero percent to wherever the insulators have trouble maintaining high voltages. Lower and upper temperature limits appropriate to semiconductor technology are likely to apply, with one exception that should receive further engineering attention. The red-sensitive photomultiplier tubes suited to a helium-neon laser have larger dark currents at high temperatures. A careful study should be made of how this interacts with the search for the smallest fibers, and whether special measures will be required.

Theoretical calculations indicate that the light intensity in the brighter detector may be a useful measure of fiber volume, thus permitting a more detailed characterization of the fibrous part of the aerosol. It came as somewhat of a surprise that the exact calculations using the extended-boundary-condition-method (EBCM), of the intensity of light scattered near zero degrees in the geometry of the two-detector fiber counter, agreed so well (20 - 40%) with the predictions of the crude Rayleigh-Gans-Deybe approximation that the forward-scattered intensity is proportional to the square of the fiber volume (see App. B). This held for thin fibers whose widths are less than a wavelength, the intensity in the brighter detector will be a monotonic and therefore useful measure of fiber volume up to quite large lengths. However, there is a need for further theoretical calculations of the scattering from long, thin fibers. The finite-element technique (FET) (11, 16) may be more approximate for the calculation of such shapes than the EBCM used for App. B of this report, because the complexity of the FET increases with particle volume, while the complexity of the EBCM increases with surface area.

SECTION 4
THE DEVICE

GENERAL PRINCIPLES

The two-detector, aerosol-fiber counter exploits the optical principle illustrated in Fig. 1. In the figure a light beam is incident from the left on a fiber, oriented with its long dimension perpendicular to the beam. The fiber is a fraction of a micron in diameter, comparable to the wavelength of light and many microns long. Some of the light is scattered and forms a diffraction pattern on a distant screen placed as indicated in the figure. The bright pattern is wider in the equatorial plane of the fiber, and narrower in the plane which contains the long dimension of the fiber and the incident beam. If a photodetector were placed at position 1 on the screen, it would measure a higher light intensity than one placed at location 2, even though both points are equally distant from the center of the diffraction pattern. This would not be true for a spherical particle, and the principle can be used to distinguish fibers from spheres and near spheres. Fibers of known orientation are most easily detected, but even randomly oriented fibers can be detected with a certain probability.

Figure 2 shows a photograph of the developmental model used in the feasibility study. This model emphasizes flexibility and adjustability, rather than portability. The sampling head, airflow system, and laser light source are on the right side of the figure. A microcomputer, its interfaces, and power supplies are on the left.

A simplified schematic of the airflow system, which resembles that of many optical particle counters, is shown in Fig. 3. The sensitive volume, about 1 mm^3 in size, is the intersection of the inlet air stream and a 3 mW, circularly polarized He-Ne laser beam. The sample air is surrounded by a sheath of clean air, as it traverses the open space between the inlet and collector tubes. An additional flow of filtered purge air has been found necessary to clean the scattering chamber after startup and/or small leaks of room air. The inlet tube

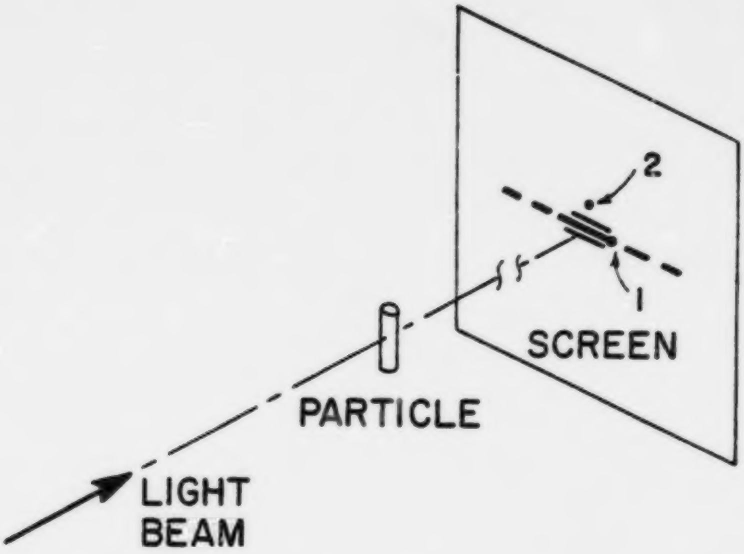

Figure 1. Diffraction pattern of a fibrous particle.

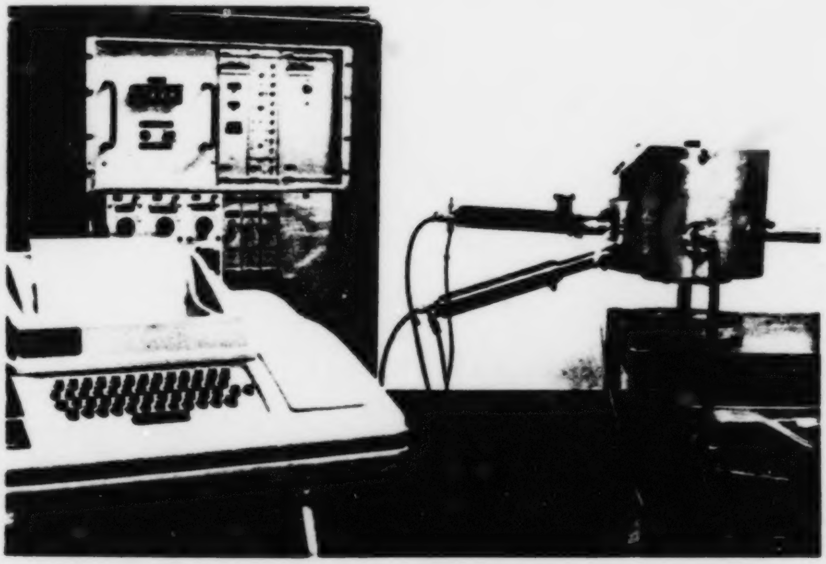

Figure 2. The two-detector fiber counter. From left to right the printer, microcomputer, and sampling head are visible.

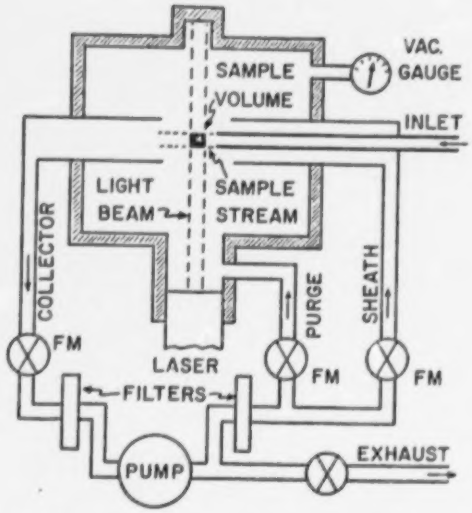

Figure 3. Simplified diagram of the airflow system. The sensitive sample volume is the intersection of the sample airstream and the laser beam.

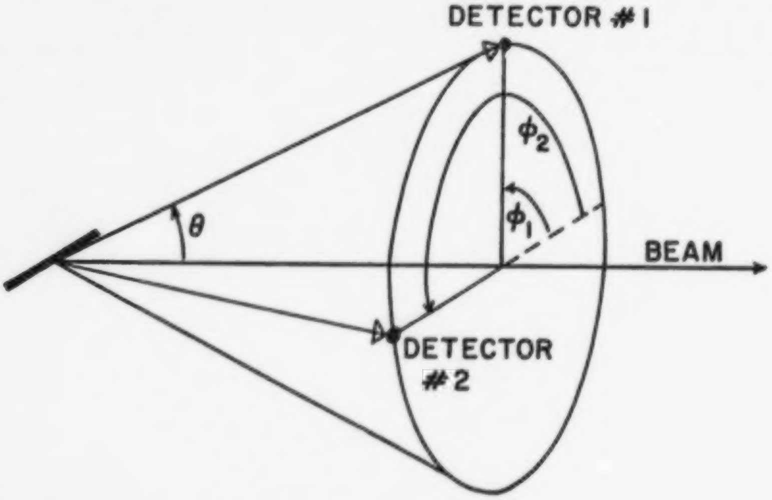

Figure 4. Two light detectors measure the intensities of the light scattered by the fiber (at the left) at a common scattering angle Θ from the incident beam, but at different azimuthal angles, ϕ_1 and ϕ_2 around the beam.

is calibrated so that the maximum air sampling rate of 5 cm^3/sec, in a laminar flow, corresponds to a vacuum of 2.5 cm (1 inch) of water in the scattering chamber, as measured by the vacuum gauge. Flow meters and associated valves, labeled FM in the figure, measure and adjust the other flow rates. Some filters have been omitted from the diagram for clarity.

The geometry for the positioning of the two photomultiplier tubes, that measure the scattered light, is shown in Fig. 4. The line from the scattering volume to detector #1, and the line of the incident beam, determine the "scattering plane" of detector #1. Although both detectors measure light scattered by the same angle Θ from the incident beam direction, detector #1, whose scattering plane is the equatorial plane of the fiber, is expected to be more brightly illuminated than detector #2, whose scattering plane includes the length of the fiber.

The photomultiplier tubes, corresponding to detector #1 and detector #2, are contained in the two long cylinders protruding from the left of the sampling head in the photograph of Fig. 5. Detector #1 is at a scattering angle, $\Theta = 20^0$, downward from the laser beam, which travels horizontally from right to left in the picture. The light trap, a pipe with a 90^0 bend, slightly obscures detector #2, which intercepts light scattered by 20^0 in a horizontal plane. The aerosol beam travels horizontally, outward from the page, and the hose in the foreground carries the air from the collector tube back to the pump. The inlet is on the other side of the sampling head. The fibers are aligned with their long axes parallel to the airflow, perpendicular to the page in Fig. 5. The sampling head is drilled to permit the use of scattering angles of 40 and 90 degrees, as well as 20 degrees.

When the light intensities are quite small, a photon-counting technique is an appropriate method of transferring the intensity measurements to a digital computer. Figure 6 shows a simplified block diagram of the intensity-measurement and microcomputer systems. Each electron, liberated by the light, from a photomultiplier's cathode is amplified to a sensible electrical pulse within the photomultiplier tube. A photon counter for each tube counts these pulses, representing single photoelectrons. Every 100 microseconds the accumulated sum is transferred to the microcomputer, and a new count is initiated by the timer indicated

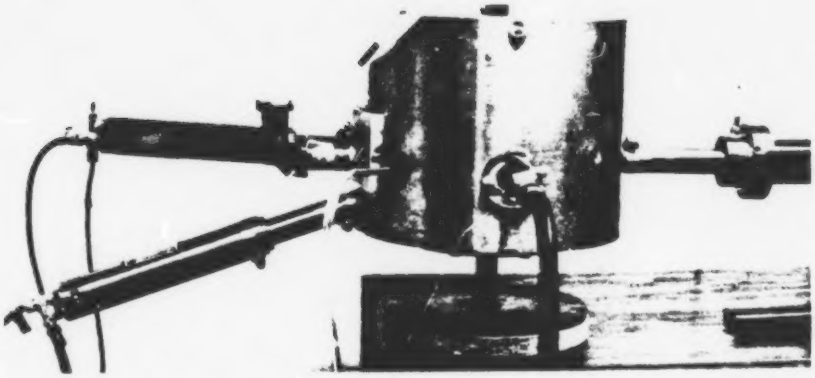

Figure 5. Aerosol-sampling head. The laser beam enters from the right, and the airflow is out of the page. Two photomultiplier tubes, in the long cylinders, measure light scattered at an angle of 20 degrees. The light trap, with a 90 degree bend, partly obscures one photomultiplier tube.

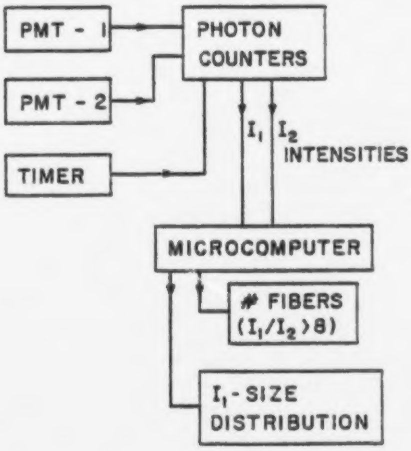

Figure 6. Simplified block diagram of the photon-counting interface and data-processing microcomputer.

in Fig. 6. The number of photoelectrons is proportional to the average light intensity during that 100 microsecond interval. When either phototube exceeds a preset level of intensity (say 25 photoelectrons in 100 microseconds), the microcomputer determines that a particle is present in the sensitive volume. If the ratio of the peak intensity (largest 100 microsecond count) from detector #1 to the peak intensity from detector #2 exceeds a preset threshold value (say 8:1), the microcomputer decides that the particle is a fiber. In that case, the fiber count is incremented by one, and the size of the brighter intensity I, is recorded by a pulse-height-analyzer subroutine as a measure of fiber size. The distribution of these intensities is available at the end of a measurement of many fibers. Other information, for both fibers and general particles, can be computed and displayed, but it is not shown in Fig. 6. It is discussed later in this section. Depending upon the amount of data analysis, the computation process occupies a time interval of 1-5 milliseconds per particle. This introduces no error in the measured particle counts, because the computer automatically extends the running time to correct for it.

A photograph of the microcomputer and its photon-counting interface is shown in Fig. 7. The light-emitting-diode display can indicate instantaneous fiber count, total particle count, or elapsed time during a measurement. However, most of the detailed information about the aerosol is presented in the form of a printout, an example of which is shown in Fig. 8.

The fiber counter would operate with randomly oriented fibers, but only a favorably oriented fraction would be counted. The counting efficiency is greatly enhanced, and a number of statistical uncertainties are eliminated, by aligning the fibers to maximize the ratio of light intensities in the two detectors. The alignment is accomplished by the fortunate reinforcement of two effects. The gradient of the airflow velocity in the sample stream causes a partial alignment of the fibers, with their long axes parallel to the streamlines. This alignment is reinforced and stablilized by an electric field, in the same direction as the flow, created by making the inlet and sheath tubes positive and the collector tube negative. See Fig. 3.

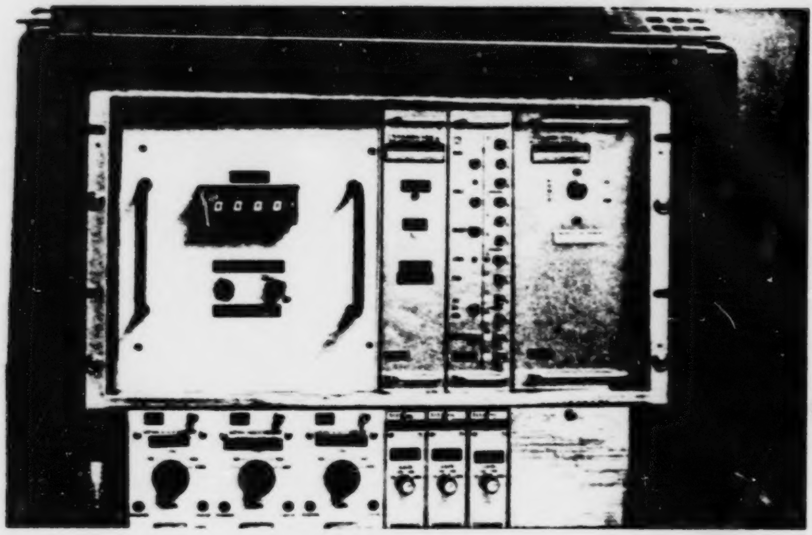

Reproduced from best available copy.

Figure 7. Front panel of the microcomputer. The top row contains, from left to right: LED data display, photon-counting interface, 12-bit microcomputer, power supply. The partly visible second row shows three high-voltage power supplies and photon-counting amplifier/discriminators.

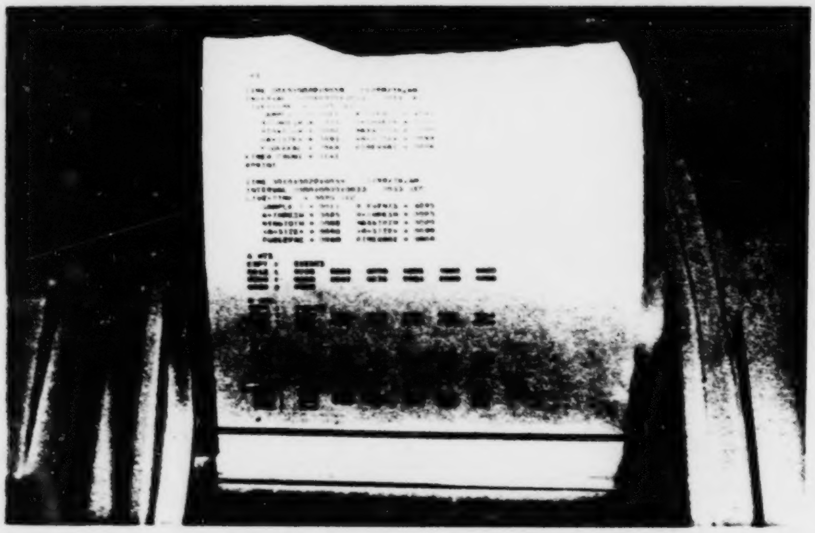

Figure 8. Typical data printout, including particle count, fiber count, clock and live time intervals, distributions of pulse heights (intensities) and widths (durations), and the distribution of intensity ratios.

AIRFLOW

The complete airflow system for the aerosol-sampling head is shown in Fig. 9. The oil-free, carbon-vane air pump (17), P in the figure, is equipped with felt inlet and outlet filters, FF1 and FF2. Although the pump is rated at 500 cm^3/sec normal operation requires only about 100 cm^3/sec for the sampling head, while 400 cm^3/sec are diverted through a copper cooling coil and the 0-400 cm^3/sec flowmeter-valve, FM1 (18). The reserve pump capacity is useful when one flushes the scattering chamber with clean air.

The aerosol sample is pulled into the inlet tube by a vacuum of 25 mm of water-equivalent in the scattering chamber, as measured by the oil manometer V (19). The constricted portion of the inlet tube, which determines the sampling flow rate for a given chamber vacuum, is about 20 cm long, with an outside diameter of 2.38 mm, and terminates in a hose connector. Most of the length has an inside diameter of 1.67 mm, but the last centimeter of the inlet tube has been constricted to an inside diameter of 0.94 mm, in order to provide a laminar flow of 5.0 cm^3/sec (.01 CFM) when the chamber vacuum is 25 mm of water-equivalent full-scale on the manometer.

The aerosol-sample stream is surrounded by a flow of clean air, the "sheath" of Fig. 9, as it enters the scattering chamber. This air has been cleaned by the membrane filter (0.2 μm pore size, 47 mm diameter) MF2 (20), and measured and controlled by the flowmeter-valve FM3 (18). The normal sheath flow rate is about 70 cm^3/sec, but the exact value is not critical. The sheath tube is coaxial with the sample tube, but is 5 mm shorter in the scattering chamber, so as not to obstruct the scattered light. The geometry in the region of the "sample volume", where the laser beam intersects the aerosol-sample stream, is shown in Fig. 10. The sample and sheath airstreams are carried across the gap in independent, laminar jet flows to a collector tube.

The parabolic velocity profile for laminar viscous flow in a long circular tube (Poisseuille flow), using parameters appropriate to the last centimeter of the inlet tube, is given by (21)

$$u = \frac{2Q}{\pi b^2} (1 - s^2), \tag{1}$$

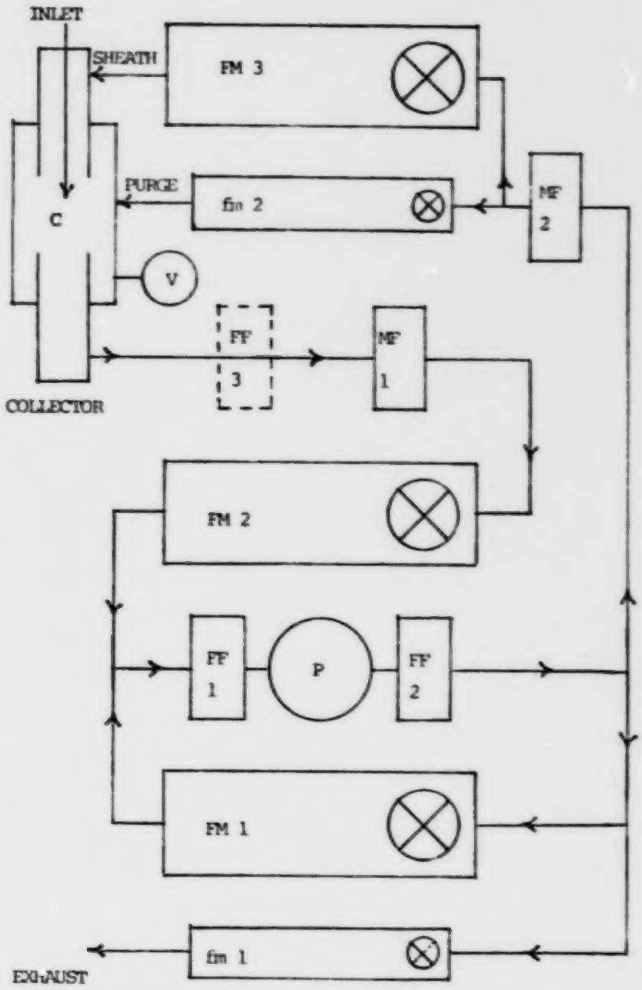

Fig. 9 The complete airflow system of the aerosol-sampling head. C = airtight scattering chamber. FF = felt filter, relatively coarse. fm = flowmeter-combination, 0-40 cm^3/sec. FM = flowmeter-valve combination, 0-400 cm^3/sec. MF = membrane filter, 0.2 μm pore size. P = carbon-vane pump. V = vacuum gauge.

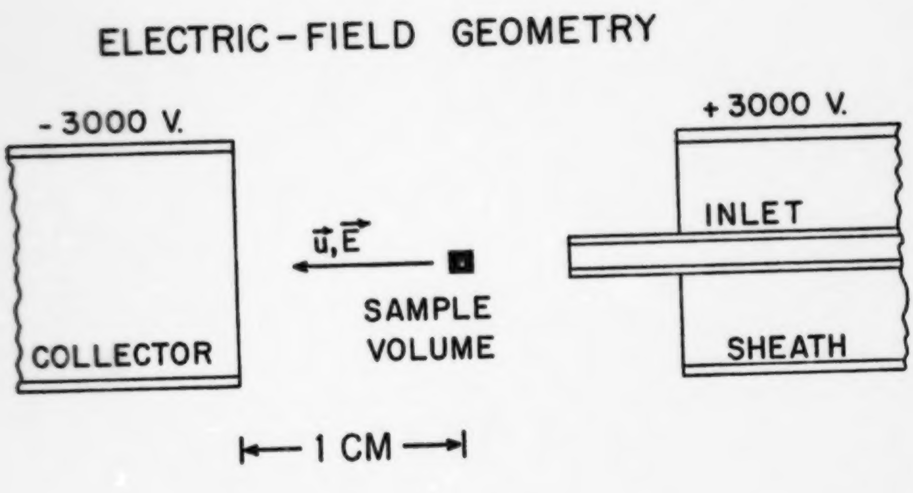

Fig. 10. The geometry in the region of the sample volume, where the velocity-gradient and electric fields align the fibers.

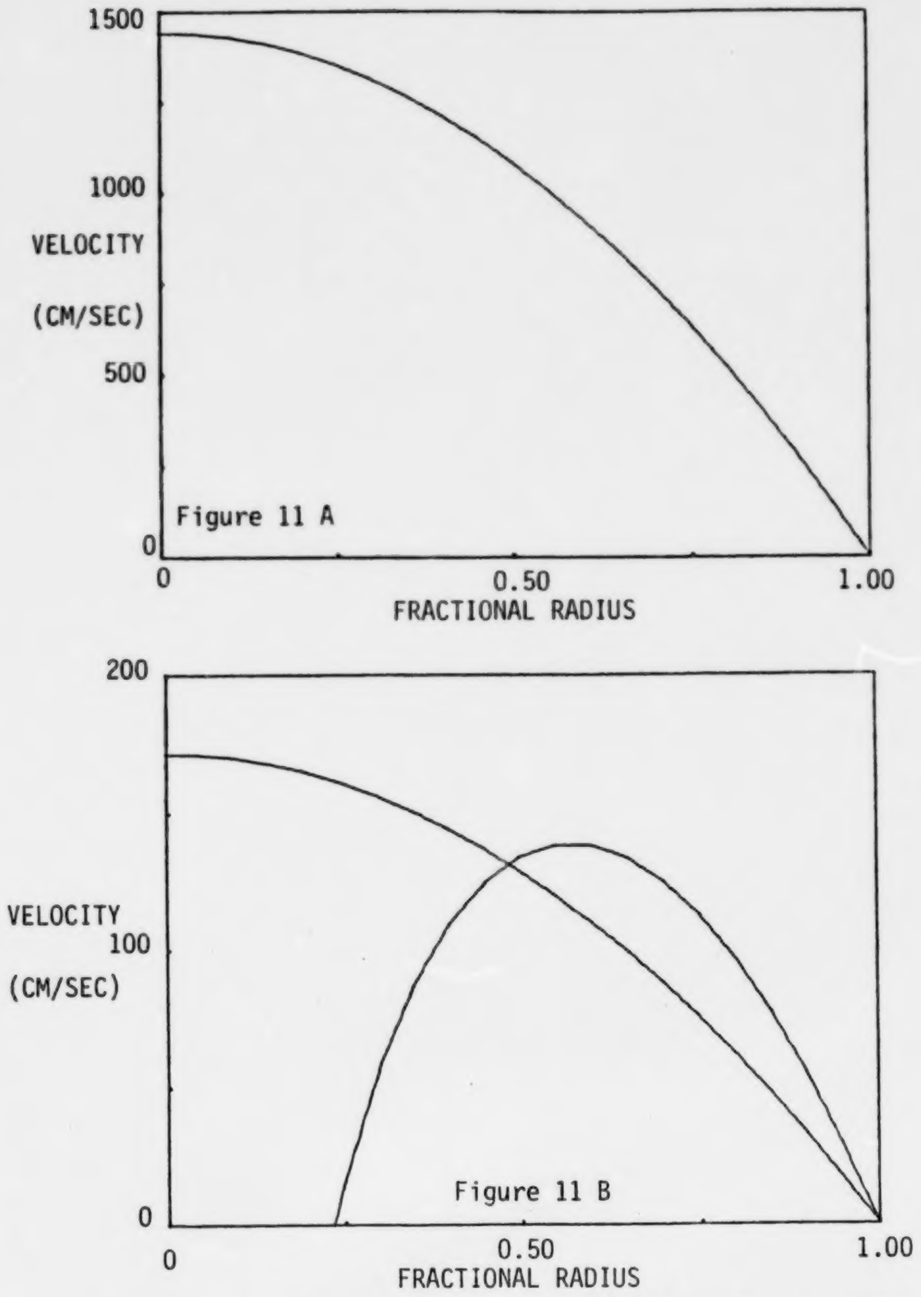

Fig. 11. Fluid velocity as a function of fractional radius for (11 A) the sample inlet tube with a flow of 5 cm^3/sec. The solid curve in B assumes a fraction 0.23 of the radius to be blocked by the inlet tube, and the dashed curve assumes no inlet tube.

in which u is the velocity at a distance r from the centerline, $b = 0.047$ cm is the interior radius of the inlet tube, $s = r/b$, and $Q = 5.0\ \mathrm{cm}^3/\mathrm{sec}$ is the volume flow rate. The maximum velocity is $u(0) = 1400$ cm/sec, and the corresponding Reynolds number for Poisseuille flow is (21)

$$N = \frac{2\,Q\,\rho}{\pi b \eta} = 450 \qquad (2)$$

for the numbers above, taking values of the density, $\rho = 1.20 \times 10^{-3}\ \mathrm{g/cm}^3$, and viscosity, $\eta = 1.81 \times 10^{-4}$ poise, appropriate to air at 20° C and one atmosphere. (22, 23) The flow has been approximated as isothermal and incompressible. It will be assumed in the following discussion that the velocity is given approximately by Eq. (1) at the exit of the inlet tube, although its length of 1 cm following the final constriction is barely adequate for the full development of Poisseuille flow with this high a Reynolds number. (24) A graph of Eq. (1) is shown in Fig. 11A.

The Reyolds number of a few hundreds is in the proper range to produce the type of flow required for the aerosol-sample stream, a stable laminar jet of nearly constant diameter across the gap between the inlet and collector tubes. First, the Reynolds number must be low enough to guarantee laminar flow within the inlet tube. This criterion is met for Poisseuille flow if $N < 2000$. (21) Second, the Reynolds number must be high enough so that the jet emerging from the inlet tube will persist with a nearly constant diameter across the gap, when surrounded by the still air of the scattering chamber or the relatively slowly moving sheath air. In the absence of an exact solution for the fluid flow in the relevant geometry of Fig. 10, this latter criterion will be shown to be satisfied roughly for $N > 100$, on the basis of the considerations discussed in the next paragraph.

Consider the laminar flow in the neighborhood of an axially symmetric jet emerging from an aperture in a wall, into a stationary fluid of the same material as the jet. In the limiting approximation of a point jet, this problem was solved by Schlichting. (25) His results were shown experimentally by Andrade and Tsien (26) to give a good approximation to the flow in the neighborhood of a real jet of finite diameter, providing that one calculates on the basis of a virtual point jet located not at the actual jet aperture, but at a distance z_0 before it. If the distance z is measured from the actual aperture parallel to the axis, and r is measured perpendicular to it, then the axial velocity component u can be written (26),

$$u(r,z) = \frac{3}{8\pi} \frac{J}{\eta} \frac{1}{z'} \cdot \frac{1}{(1 + \xi 2/4)^2} , \tag{3a}$$

where

$$z' = z + z_0 \tag{3b}$$

and

$$\xi = \frac{1}{4\nu} \left(\frac{3J}{\pi\rho}\right)^{\frac{1}{2}} \frac{r}{z'} . \tag{3c}$$

In Eqs. (3) η is the viscosity, ρ is the density, and $\nu = \eta/\rho$ is the kinematic viscosity of the fluid. Schlichting's derivation assumes that the pressure gradient is negligible, and therefore that the momentum crossing a plane normal to the axis of the jet per second,

$$J = 2\pi \rho \int u^2 r \, dr, \tag{4}$$

is conserved. The experiments of Andrade and Tsien were able to resolve much finer details of the flow than are needed here, where it will suffice to say that the value of z_0 required to fit their data was related to the radius b of their aperture and the Reynolds number N defined here (twice their definition) by the relation,

$$z_0/b = 0.080 \text{ N}. \tag{5}$$

The falloff of the velocity u from its central maximum in Eqs. (3) is governed by the variable ξ . Therefore, the "radius of the jet" should be defined as that value of r for which ξ has a certain value. According to Eqs. (3b) and (3c), the radius of the jet will be proportional to z', a linear function of z. One might demand that the radius of the jet should not do worse than double the value it has on leaving the aperture; i.e., $z < z_0$. Using Eq. (5), this criterion becomes

$$N > 12 \, z/b. \tag{6}$$

In the geometry of Fig. 10, the distance from the end of the tube to the scattering volume is $z = 0.5$ cm, and Eq. (6) becomes $N > 120$. The complexity of the true geometry and the presence of the slow sheath flow lead to the conclusion that the criterion of Eq. (6) is only a rough estimate, but it serves to indicate the important parameters and the order of magnitude of the numbers involved. Our own experiments with a smoke source at the inlet show that the aerosol-sample stream persists as a stable, laminar jet of nearly constant diameter across the gap between the inlet and collector tubes, for flow rates Q between 1 and 5 cm^3/sec ($N = 90$-450). Below a value of $Q = 1$ cm^3/sec the jet diverges excessively, and tends to diffuse as it enters the collector tube. The sheath flow rate is observed to have only a slight influence. This fact is explained by the relatively low sheath velocity, which makes the sheath nearly equivalent to still air. The only observations of turbulent flow in the sample jet have occurred when the jet was partly clogged by a large dust particle from the cigarette smoke used to make the stream visible.

The airflow within the sheath tube can be described as viscous laminar flow between two coaxial round tubes, and does not differ greatly from Poisseuille flow when the inlet tube is relatively small. The fluid velocity u at a distance r from the centerline is given for this case by (21)

$$(7) \qquad u = \frac{2\,Q}{\pi b^2} \; \frac{1 - s^2 - (1 - c^2)\,(\ln s)\,/\,(\ln c)}{1 - c^4 + (1 - c^2)^2\,/\,(\ln c)} \;,$$

where $b = 0.51$ cm is the interior radius of the sheath tube (exterior radius of the flow), and $s = r/b$ as before. Also, $a = 0.119$ cm is the exterior radius of the inlet tube, and $c = a/b = 0.23$ measures the relative size of the inlet tube. The volume flow rate for the sheath was typically 70 cm^3/sec. A graph of Eq. (7) is shown as the solid line in Fig. 11B, along with a dashed curve, for comparison, with the same Q but with $c = 0$. Although it is not quite legitimate to apply the Reynolds-number criteria appropriate to Poisseuille flow to the sheath flow, because they are not really dynamically similar, the maximum velocities and maximum velocity-gradients of the two curves in Fig. 11B differ by less than a factor of two. Therefore, when the application of Eq. (2) to the sheath flow gives N = 580, comfortably within the desirable range of 100-2000 for a persistent, laminar solid jet flow across the 2 cm gap between sheath and collector tubes, one can safely predict that the hollow sheath jet will also be stable in the region of the sample volume. (See Fig. 10.) Experimentally, the sheath jet is very stable within the gap, and the exact value of its flow rate is not critical.

In practice the sheath serves two simple purposes. First, it protects the scattering chamber and optics from dust particles that might escape from the sample flow. Second, the short (relative to its diameter) and therefore rather robust sheath flow serves to protect the long and more delicate sample flow from other air currents within the scattering chamber, especially the purge flow. Aside from these protective functions, the sheath has little effect upon the sample flow in this instrument, because its maximum velocity is so much less than that of the sample that it might as well be still air.

Undoubtedly, a thoughtful design effort could make better use of the sheath flow in hydrodynamically focusing the sample jet. (27) This, together with a reduction in the diameter of the inlet capillary, might succeed in reducing the diameter of the aerosol-sample stream in the scattering region to as little as 0.3 mm (28), a reduction by a factor of 3 from its present value. Consequently, the laser beam could be reduced in size, and the peak light intensity increased by a factor of $3^2 = 9$, without increasing the background light or changing the pulse-size resolution. The disadvantages of such a change might include a reduced maximum sampling rate to avoid turbulence, possible clogging of the reduced inlet aperture by long asbestos fibers, and unknown effects of the more complex air-flow patterns upon alignment of the fibers. The last possibility could require further investigation, because Andrade and Tsien (26) remark that a converging nozzle converts Poisseuille flow to a square velocity distribution, lacking the convenient velocity-gradient of the Poisseuille flow in the inlet tube, but the velocity gradient in the jet region might be adequate to orient the fibers with the help of the electric field in any case. Some advantages accompanying the reduction of sample volume are the reduced sensitivity to coincidence effects, by a factor of 3^3, and a reduction in the predicted minimum-detectable-particle volume due to molecular scattering by a factor of $3^{1.5}$. (29)

The third component of the air entering the scattering chamber is the "purge" air of Fig. 9. This flow of clean air, controlled and measured by the 0-40 cm^3/sec flowmeter-valve fm2 (30), is required primarily to clean the remote parts of the scattering chamber of background dust. If the remnant dust in the scattering chamber happens to diffuse into the sample volume of Fig. 10, it will be indistinguishable from dust entering the inlet tube. The sheath flow effectively removes this possibility from further consideration. However, remnant dust can diffuse into other parts of the light beam, that are not protected by the sheath but from which some scattered light can still reach the photomultiplier tubes. It is unfortunately true that there are some such regions where one phototube is much more brightly illuminated than the other, and remnant spherical dust particles in these regions did give false fiber counts. The most critical region, with the laser light source, is near the focal point of the spatial-filter/beam-expander lens. Therefore, in the final design the purge air is admitted via the laser optical system ahead of the lens, so as to flow around the lens and thereafter along the axis of the light beam, through the spatial-filter and other apertures. Despite the fact that this aims the purge flow of about 15 cm^3/sec directly at the side of the sheath jet, from a distance of 5-10 cm, it did not in our tests seem to affect the sheath jet adversely. Perhaps the destablilizing effect of the directed purge flow is somewhat counteracted by what has been noted to be a generally stabilizing effect of a diffused purge flow upon the sheath and sample flows in the region of the collector tube. (28) When the scattering chamber was truly vacuum tight, the time constant for cleanup of the critical regions was determined to be of the order of 5 minutes. However, even very tiny leaks of room air could produce an unacceptable background. The most troublesome one turned out to be a path through the laser housing itself. Because the region around the laser beam is so very critical, the flow of purge air along the beam is highly recommended. Also, a careful redesign of the light collection system of the photomultiplier tubes, so as to reduce their response to light scattered outside the sample volume, would reduce the demands upon the purge airflow to keep the system clean.

The inlet, sheath and purge flows are conveyed by the collector tube, whose inner diameter equals that of the sheath tube, to the membrane filter, MF1 in Fig. 9 (0.2 μm pore size, 47 mm diameter) (20), and thereafter to the pump. The flow is measured and controlled by the flowmeter-valve FM2 (18). In principle the exhaust flowmeter-valve fm1 (30) controls the sample-inlet flow, but in practice it is found that this interacts with the other valve settings. Apparently there is sufficient leakage at the pump bearings to invalidate the assumption of a zero net flow of air. Therefore, the inlet flow was determined by measuring the vacuum in the scattering chamber with manometer V. The calibration in terms of inlet flow was made with a soap-bubble flowmeter, and the proportionality constant between vacuum and flow rate was made to be convenient by adjusting the diameter of the last centimeter of the inlet tube. The additional large felt filter FF3 was required during alignment of the sample stream with cigarette smoke, in order to delay clogging of the membrane filter MF1. An additional filter would have been useful to protect the exhaust flowmeter fm1 from the carbon dust leaking through FF2.

The original intent was to use the membrane filter MF1 for microscopic fiber counting, for calibration purposes. However, the non-uniform particle distribution expected across the filter surface, coupled with the small total number of fibers expected at this point, would make statistical interpretation of such a count very difficult. It was decided instead to use an open-face filter exposed directly to the aerosol near the sample intake.

At the time that the data from the instrument indicated that the air-flow-velocity gradient was partially aligning asbestos fibers in the sample volume, it was realized that the instrument itself provided the most direct way to measure such alignments. Therefore, it was decided to proceed immediately to study the additional aligning effects of an added electric field. There was little room near the sample volume for added electrodes, but Dr. M. Whatley of the University of Vermont made the key suggestion that using the inlet and sheath tubes as electrodes would be simple, and it would provide an electric field in the proper direction to to reinforce the alignment due to the velocity gradient. Within a few days, the tubes had been insulated, the electric field was applied, and the complete fiber alignment due to the combined fields was verified experimentally, all during the last week of the grant period. Figure 10 shows the geometry of the field electrodes. The sheath tube and inlet tube are connected together, insulated from the scattering chamber, and raised to a potential of +3000 volts relative to the chamber ground. The collector tube is likewise insulated, and connected to -3000 volts. Protective series resistors prevent dangerous shocks. The detailed electric-field configuration for the geometry of Fig. 10 has not been calculated, but it seems reasonable to say that the electric field E in the region of the sample volume is about 3000 volts/cm.

Several parameters of the flow in the sample volume, taken for simplicity to be approximately the same as the Poisseuille flow in the inlet tube, are needed for the later discussion of fiber alignment. Because various quantities, such as the velocity u, vary with distance r from the centerline, averages will be given. Two kinds of averages are appropriate to different cases:

$\overline{f(r)}$ = the average over all volume elements in a length L of fluid, at a fixed time

$$= \int_0^b f(r)\, 2\pi r L\, dr / (\pi b^2 L) = 2 \int_0^1 f(sb)\, s\, ds$$

$\langle f(r) \rangle$ = the average over all volume elements passing a fixed cross section in a time interval T.

$$= \int_0^b f(r)\, u(r)\, 2\pi r\, T\, dr / (QT)$$

$$\langle f(r) \rangle = 4 \int_0^1 f(sb)\, (1 - s^2)\, ds \qquad (8)$$

The velocity profile of Eq. (1) has been assumed in obtaining the explicit forms of Eq. (8) needed for the evaluations below. In addition to the velocity u, the velocity gradient,

$$g = -du/dr, \qquad (9)$$

will be required. The maximum velocity is denoted by U, and the maximum gradient by G. For the values of parameters associated with normal operation (e.g., Fig. 11),

(10) $U = 1440$ cm/sec

(11) $G = 61000$ sec^{-1}

(12) $\langle r \rangle = .025$ cm

(13) $\langle u \rangle = 960$ cm/sec

(14) $\langle g \rangle = 33000$ sec^{-1}

(15) $E = 3000$ volts/cm.

LIGHT SOURCE

Two different light sources were tried for this device, a tungsten-filament source and a He-Ne-laser source. The tungsten source was favored for its broad wavelength spectrum, but the laser source was so superior in reducing stray light at forward scattering angles that it was finally adopted.

The scattering process may be described by the following average parameters, some of which are illustrated in Fig. 12.

I = the incident intensity;

$\overline{\lambda}$ = the average wavelength λ of the incident light;

$\overline{\Theta}$ = the average scattering angle Θ;

$\overline{\phi}$ = the average azimuthal angle ϕ;

$\overline{\sigma}$ = the average differential scattering cross section $\sigma(\lambda, \Theta, \phi)$;

$\Delta\Theta$ = the vertex half-angle of the detector's acceptance cone;

$\Delta\gamma$ = the vertex half-angle of the incident beam's cone, or its half-width at half-maximum intensity;

$\Delta\lambda$ = the half-width at half-maximum intensity of the effective intensity spectrum $F(\lambda)$ presented to the scatterer.

The effective intensity spectrum $F(\lambda)$ is the product of the intensity spectrum $I(\lambda)$ of the source and the sensitivity $S(\lambda)$ of the detector:

(16) $F(\lambda) = I(\lambda)\ S(\lambda)$.

In order to compare the intensities of two spectrally different sources and/or detectors one must find a common reference. This can be done by defining the effective integrated intensity I_e presented to the scatterer in terms of the number of photoelectrons per second released at the photomultiplier-tube cathode:

(17) $I_e = \int I(\lambda)\ S(\lambda)\ d\lambda$ photons cm^{-2} sec^{-1}.

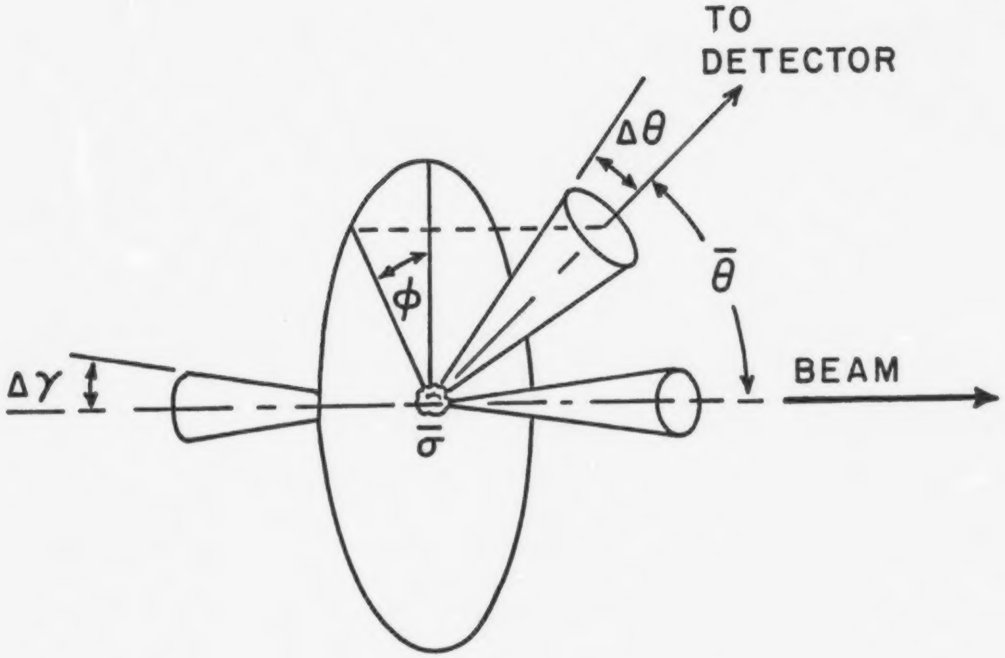

Fig. 12. Scattering geometry in an aerosol counter, defining the half-angle $\Delta\gamma$ of the beam-convergence cone, and the half-angle $\Delta\theta$ of the detector-acceptance cone, for a scattering cross-section $\bar{\sigma}$ at average polar angles $\bar{\theta}$, $\bar{\phi}$.

The counting rate in the detector, dn/dt, is then given by

(18) $$dn/dt = I_e \bar{\sigma} \pi (\Delta\Theta)^2.$$

When a thermal source is focused upon a target area, the maximum effective intensity attainable is determined by the source temperature and emissivity and the cone angle $\Delta\gamma$. For a fixed value of $\Delta\gamma$ it is independent of the size of the illuminated area and the size of the source, provided only that the source is large enough so that its image covers the target area.

When a laser source illuminates a target area, the integration of Eq. (17) can be performed trivially, but the effective intensity depends upon the size of the illuminated area A, as well as the rated power P of the laser:

(19) $$I_e = P\ S/A.$$

The cone angle $\Delta\gamma$ is commonly too small to be a consideration for a laser source.

The initial design assumed an illuminated area $A = 1\ mm^2$, appropriate to the inlet-tube design, and a maximum cone angle $\Delta\gamma = 5^0$, limited by the scattering geometry at small angles. The thermal source was to be a 100 watt, tungsten-filament lamp with a halogen-filled quartz envelope (31), operating with a filament temperature of about 3000 K. The phototube to be used with this source was a type 9824B with a bialkali cathode (32). Integrating a black-body spectrum (33) multiplied by a constant emissivity of 0.42 for tungsten in the visible region (34) for $I(\lambda)$, and the published sensitivity $S(\lambda)$ of the phototube (32), produced an effective intensity presented to the scatterer of $I_e = 1.6 \times 10^{16}$ photons $cm^{-2}\ sec^{-1}$. Using the maximum rated filament temperature of 3300 K would approximately double the intensity, but would shorten the lamp's lifetime. For the thermal source the peak of the effective intensity spectrum occurs at about $\bar{\lambda} = 500nm$, and the curve is nearly symmetric with a half-width $\Delta\lambda = 80$ nm. This bandwidth is advantageous in two ways. First, it avoids interference between the amplitudes of light scattered by two particles that happen to be in the scattering volume simultaneously, a potentially serious coincidence error that will be discussed later. Second, it helps to average out any deep, sharp minima in the scattering cross section of a nearly symmetric particle that might cause it to be accidentally classed as a fiber. The thermal source has a spectrum that extends sufficiently far into the blue to take advantage of the low dark current of a bialkali cathode in the photomultiplier tube.

The laser source was a linearly polarized, 4 mW He-Ne laser (35), followed by a quarter-wave plate to give circularly polarized light, equivalent for scattering purposes to the unpolarized light from the tungsten filament. The red laser necessitated the use of a different photomultiplier tube, and a type 9798A with S-20 photocathode (32) was chosen. The effective intensity on a 1 mm^2 target area, calculated for a quantum efficiency of 5 percent at a wavelength $\lambda = 633$ nm, is $I_e = 6.3 \times 10^{16}$ photons/(cm^2 sec).

Under the conditions above, the tungsten lamp is equivalent in intensity to a He-Ne laser with a beam-power rating of about 1 mW. If a larger angle of convergence can be used with the incandescent source, as in more conventional optical particle counters, this increases in proportion to $(\Delta\gamma)^2$. A shorter wavelength laser would give added advantage to the laser source by increasing the photomultiplier's quantum efficiency and reducing its dark current, as well as having generally beneficial effects on the scattering cross sections for small particles. However, blue lasers (e.g., cadmium or argon-ion) are prohibitively expensive and demanding of large amounts of electrical power. If a smaller target area A were to be illuminated, the laser intensity would increase proportional to 1/A. Therefore, a reduction in the aerosol-sample-stream diameter by a factor f would increase the effective intensity of a given laser source by a factor f^2, but would produce no advantage for a thermal source.

The incandescent source was the first one tried in the device. An image of the 2 mm x 4 mm lamp filament (31) was produced, by a lens system comprising two condenser lenses of 3 cm focal length each, on a circular aperture about 1 mm in diameter. This aperture was then imaged upon the sample volume by a third lens. Operating the condenser system slightly out of focus gave a uniform beam-intensity profile with sharply defined edges. The system worked fairly well at a scattering angle of 90 degrees, but the stray background light remained excessive at small scattering angles, despite several redesigns of the beam-skimming apertures following the final lens. It appeared that the system was too sensitive to otherwise minor flaws (bubbles, scratches, etc.) in and on the lenses in the light beam. A finger print or a large piece of dust, for example, produced a serious increase in background. Why this should be so, when conventional light-scattering aerosol counters operate with incandescent sources, requires some sort of explanation. The main reason seems to lie in the small solid angles, $\pi(\Delta\Theta)^2$, required by the necessity for the detectors to be sensitive to the azimuthal direction ϕ in this device. The background light is chaotic and comes from all directions, while the signal originates within a small scattering volume. A light-focusing detector system can increase the apparent brightness of a point source in proportion to $(\Delta\Theta)^2$, while the apparent brightness of the random background remains independent of $\Delta\Theta$. (Thus, using even a simple set of binoculars permits one to see stars against the blue sky in the daytime.) Most optical aerosol counters with incandescent sources take advantage of this property in one form or another, many collecting the scattered light over an angle of 360^0 in ϕ, in order to see small particles with adequate signal-to-noise ratio. This device is limited to values of $\Delta\Theta$ in the range $5\text{-}10^0$, although an asymmetric acceptance cone for the detector could make some improvement.

With some reluctance, the incandescent source was discarded in favor of a laser source. The last configuration of the laser light source is shown in Fig. 13. After passing through the quarter-wave plate Q and a window W sealing the end of the laser snout against air leaks into the scattering chamber, the light beam was focused by the converging lens L with a 5 cm focal length upon the small aperture A1. This 1 mm circular aperture provided a crude spatial filter to remove the stray light produced by interface reflections and dust scattering on the surfaces of the laser mirror, quarter-wave plate and window. A smaller aperture would have produced an even cleaner beam, but it would have required a ticklish alignment task with the present laser mounting system. The diameter of the slightly diverging light beam in the scattering region was conveniently adjusted by sliding the laser source in or out of the side of the sampling head (see Fig. 5), varying the distance between

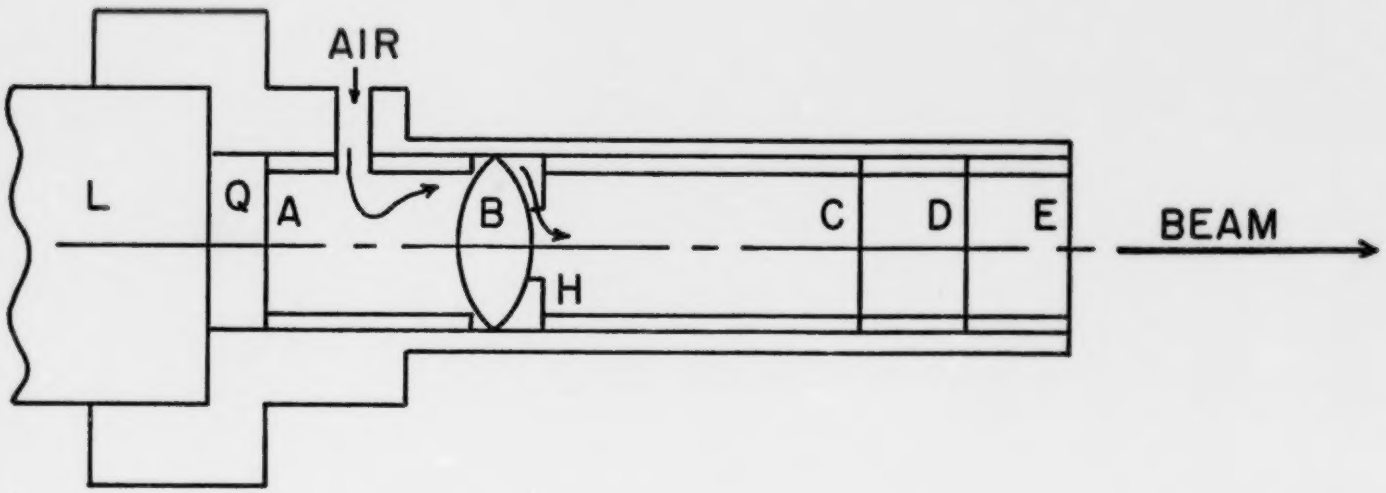

Fig. 13. Schematic diagram of the laser light source. Linearly polarized light from the He-Ne laser L passes through the quarter-wave plate Q and the sealed window A. It is focused by lens B through a 1 mm-diameter aperture C, 5 cm further along its path. The now diverging beam emerges after two more light-skimming 3 mm-diameter apertures D and E. Clean purge air enters ahead of lens B, flows around the lens through the slotted lens-holder H to the beam axis, and exits through apertures C, D, and E.

aperture A1 and the sample volume. The larger apertures A2-A4 served as beam skimmers to reduce unwanted light that might reach their areas after multiple reflections or scattering by dust particles in the beam.

Because the intensity falls off gradually at the edges, the diameter of a laser beam is not sharply defined. For lasers such as this one, which operates in the TEM_{00} mode, it is customary to specify an exit-beam diameter 2 w, where the intensity falls to e^{-2} times the central value. (36) The diameter at the half-intensity points, D' = 1.18 w, is more appropriate for comparisons with the diameter of the sample air-stream. The laser specifications (35) show that 2w = 0.81 mm, D' = 0.48mm at the output of the laser, but this is too small for the aerosol-sample beam. The optical system permits the half-intensity diameter D of the light beam in the scattering region to be adjusted between 0.5 and 1.5 mm. It was usually set to the latter value. If one approximates the sample volume as a right circular cylinder of length D = 1.5 mm and diameter d = 0.94 mm (the inside diameter of the inlet tube), the sample volume contains 1.0 mm^3. The Gaussian beam-intensity profile and finite sample-stream diameter imply that not all scattering particles will be illuminated with equal brightness. For the parameters above, the edges of the sample stream will experience a light intensity decreased by a factor of $\exp(-0.69\ d^2/D^2) = 0.76$ from the maximum value. The light intensities scattered from monodisperse spherical aerosols must have a distribution with at least this width, and the observed distributions were consistent with this expectation. Of course, the reduced intensity at the edge of the beam affects both detectors equally and does not affect the intensity ratio used to judge a particle's sphericity.

One aspect of the construction of the laser-source optics deserves another mention. Because the intensity of the laser beam is at least ten thousand times higher near the point focus than it is in the sample volume, the presence of a few stray dust particles near the aperture A1 caused serious problems, until the chamber purge air was routed along the laser beam. The purge air now enters just ahead of the lens L, flows around the lens, and then flows through A1 and down the beam path to the scattering chamber.

In the scattering volume, after all the interface reflections, etc., the laser power is about 2mW, and the beam diameter is about 1.5 mm. Therefore, the effective intensity in the scattering volume is about 1.2×10^{16} photons/(cm^2 sec) if the phototube's quantum efficiency is 5 percent.

PHOTODETECTORS AND PHOTON-COUNTING INTERFACE

The scattering chamber is made from an aluminum block, drilled with holes of 2.5 cm inside diameter that will permit mounting pairs of photodectors at scattering angles of 20^0, 40^0 or 90^0. At the angles of 20^0 and 40^0, the two detectors have azimuthal angles of 0^0 and 90^0, relative to the plane containing the incident laser beam and the airflow which aligns the fiber axis perpendicular to the beam, as shown in Fig. 4. At a scattering angle of 90^0, the two detectors can be placed either 90^0 or 180^0 apart in azimuth.

Each detector assembly includes a type 9798A photomultiplier tube mounted in a type QL-30 base and shielded housing fabricated by the tube manufacturer. (32) The 23 mm diameter of the photocathode is restricted to a sensitive area 6 mm in diameter by a circular aperture drilled in a thin piece of black phenolic plastic. This aperture must be made of electrically insulating material, because it touches the tube envelope near the end-window photocathode, which is operated at minus 1450 volts relative to ground. The aperture is preceded by a long-pass red glass filter with a cutoff wavelength around 600 nm (37) to attenuate the blue discharge light that accompanies the red output of most He-Ne lasers. An image of the same volume is projected upon the aperture by a converging lens at the front of the detector mount, as shown in Fig. 14, in one of two different configurations. In one configuration, more appropriate for the 20^0 scattering angle, the converging lens has a focal length of 5 cm, and must be placed at a distance 8.3 cm from the sample volume for an acceptance half-angle $\Delta\Theta = 6.5^0$. In the other configuration, more appropriate for the 90^0 scattering angle, the converging lens has a focal length of 3 cm, and must be placed at a distance of 4.0 cm from the sample volume, for an acceptance half-angle $\Delta\Theta = 13^0$. See Fig. 12.

It will be seen later that the 90^0 scattering angle is more appropriate for the smallest particles, and that the extra factor of 4 in the light-gathering power of the 3 cm lens will be useful. However, the 20^0 angle is appropriate for the most interesting range of fiber sizes, and all of the fiber data, and most of the calibration data, were recorded there with the 5 cm lens, giving each detector an acceptance solid angle of 0.04 steradians. The machining necessary to provide the

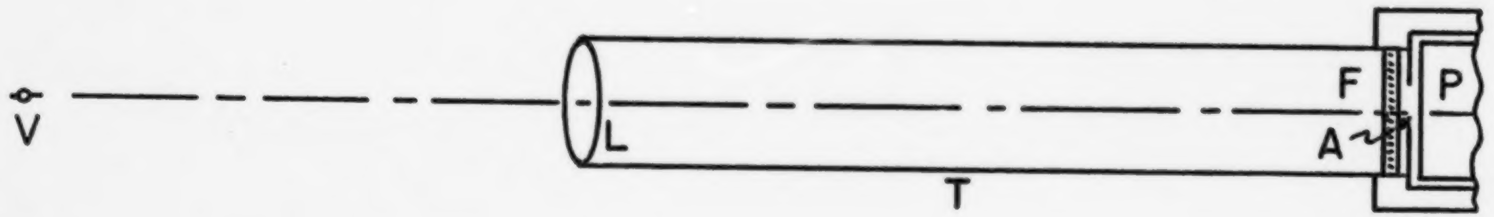

Fig. 14. The light-collection system of one photodetector. For scattering at an angle of 20 degrees, the lens L had a focal length of 5 cm and projected onto aperture A, of 6 mm diameter, an image of the scattering volume V. The red filter F preceding the aperture reduced sensitivity to the blue background light from the laser discharge or room light. The tubing T was lined with black felt to reduce reflections of stray light. The photomultiplier tube P behind the aperture had a cathode of 23 mm and could accommodate larger apertures, which might be appropriate to other scattering angles and/or distances.

fiber alignment most advantageous for the 90^0 ports was not completed until after the grant period had terminated.

The photomultiplier-tube bases contained voltage dividers for the dynodes, and impedance-matching resistors for the 50 ohm coaxial cables carrying the output signals, but no active electronic circuits. The phototubes were operated at a gain of about 10^6, so that each electron leaving the cathode would produce a pulse of about 10^{-4} volts in amplitude and 3×10^{-8} seconds in width (32) at the input to the photon-counting amplifier-discriminator (38). See Fig. 15. The amplifier operated with a gain of about 10^3, and the discriminator threshold was about 10^{-1} volts. The output of the discriminator was a standard TTL pulse about 40 nanoseconds wide, which was fed to a pulse-counting circuit in the computer interface. Thus, each photon which was successful in liberating an electron from the photocathode (about 5 percent of the incident photons) would be counted. The power in watts of the light falling on the photocathode was converted to a counting rate of so many photons per second, with a stable conversion factor. The conversion factor, essentially the sensitivity of the photon counter, is only slightly dependent upon the gain of the phototube and, hence, much more stable than the sensitivity of circuits which might use the integrated phototube current and an analog-to-digital converter at the computer interface.

The interface circuit contained its own clock, and its main function was to present up to three simultaneous photon counts every 100 or so microseconds to the computer. It was treated as an asynchronous input device; a flag, set when the data were ready, was tested under program control. The interrupt lines of the computer were reserved to signal the detection of a data error or a 60 Hz real-time-clock pulse.

The integrating time of the intensity-measuring system must be comparable to the transit time of a dust particle across the light beam, say 100 microseconds. This is accomplished in the following manner. Each phototube-amplifier-discriminator combination feeds standardized pulses into its own binary counter in the computer-interface circuit, which accumulates counts at a rate proportional to the instantaneous light intensity. A clock in the interface turns off the counter after 100 microseconds, and during the next 2 microseconds the count is transferred to

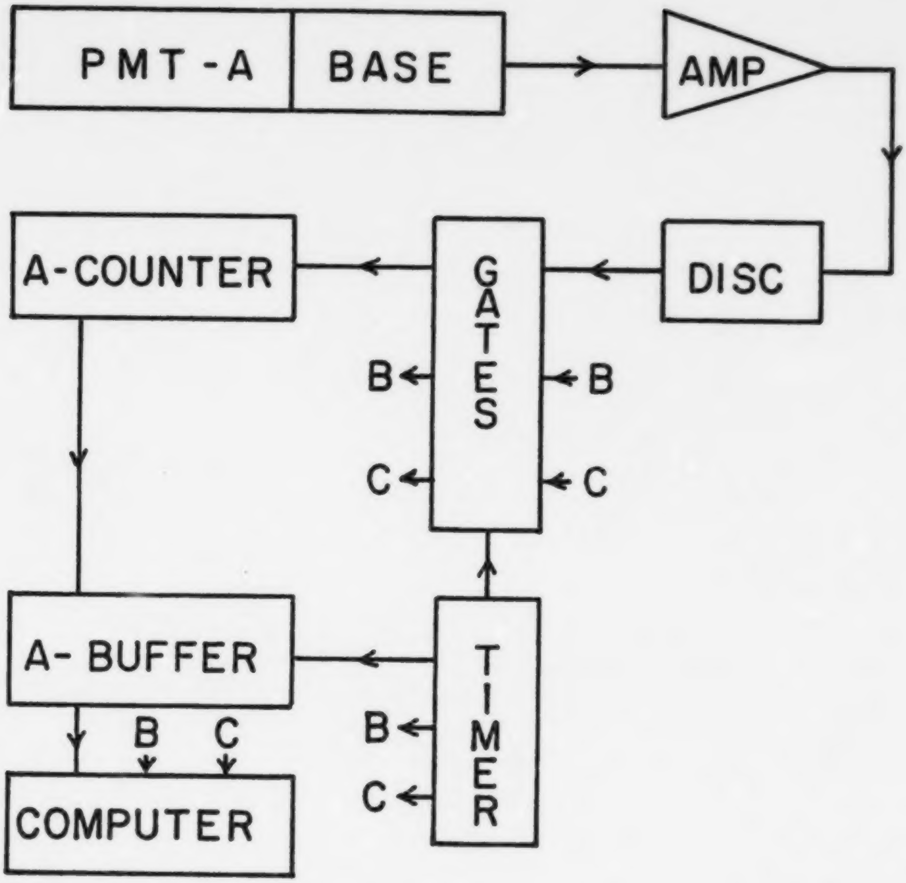

Fig. 15. Block diagram of photon-counting interface for input A. The photomultiplier tube and base are a single unit. The amplifier and discriminator are another unit, mounted in the instrument rack. The interface card within the microcomputer case contains the timer and gates shared by inputs A, B, and C, along with a counter and buffer for each of the three inputs. The timer opened the gates simultaneously for one sampling interval (usually about 100 microseconds), then latched the data in the buffer during a 2 microsecond interval, for transfer to the microcomputer itself.

temporary buffer storage, while the counter is cleared and the data flag is set to notify the computer. Then, a new counting interval of 100 microseconds is initiated, during which the computer can read the previous data from the buffer, before new data are presented. In this manner, the computer is presented with a succession of light-intensity measurements every 102 microseconds, each averaged over a 100 microsecond interval. Up to three phototubes can be monitored simultaneously in three separate binary counters. The exact length of the counting interval is under program control, in 10 microsecond steps. Because several different computer programs were used, the interface had provisions for detecting data that might be lost because a particular program did not permit the computer to get back in time to collect it. The most commonly used calibration program was quite complex and required 110 microseconds to complete its cycle. The other data-processing functions, aside from the timing of the counts, were relegated to the stored-program computer.

The photon-counting technique provides naturally a digital output for measuring light intensities. It was chosen because it had been decided early in the project's design to use a stored-program digital computer for data processing, for reasons of flexibility. The technique is simple, direct, and flexible, capable of measuring the lowest light levels with the best possible signal-to-noise level, and also capable of providing a linear response to a wide range of light intensities. The photon-counting interface uses a 12 bit binary counter to match the word length of the microcomputer, and therefore can record intensities from 1 to 4095 in units of counts, with a "dynamic range" of about 4000:1. The dynamic range is important because it limits the size range of fibers that can be measured with one sensitivity setting of the instrument. Of course, one can measure larger fibers by reducing the instrument's sensitivity but that is inconvenient. For the smallest fibers the intensity in the more brightly illuminated detector is proportional to the square of the particle volume when the detectors are in the forward direction. The dynamic range above corresponds to a ratio of 64:1 in the volumes of the largest and smallest fibers. For a fixed diameter, this corresponds to a length ratio of 64:1; for a fixed length, it corresponds to a diameter ratio of only 8:1; and for a fixed aspect ratio (shape), it corresponds to a diameter ratio of only 8:1; and for a fixed aspect ratio (shape), it corresponds to a linear-size ratio of only 4:1. It is not possible to increase the upper intensity limit by merely increasing the number of bits in the photon counter, and thereby increase the dynamic range, because in practice another set of considerations governs the attainable dynamic range.

The lowest photon count rate is set by either the background light in the chamber, 8×10^4 counts/sec in the current device or 8 counts in a typical 100 microsecond interval, or the dark current of the photomultiplier tubes, which is strongly temperature-dependent but might be 5×10^3 counts/sec when they become warm. The highest photon count rate is set by the temporal resolution of the phototube or the electronics, about 2×10^7 counts/sec for the current version of the device. Thus, when the present device is set to detect the smallest fibers consistent with an adequate signal-to-noise ratio, the maximum count rate limits the upper fiber size that can be measured without reducing sensitivity, say by reducing the size of the detector apertures. Reducing the background light and selecting a phototube with a lower dark current can reduce the lower limit and thereby increase the dynamic range by perhaps a factor of 10. The maximum count rate can be extended to 1×10^8 counts/sec by a better choice of photomultiplier and counting electronics. Thus, the dynamic range might be extended slightly beyond 10^4:1 with the photon-counting technique. A linear analog technique would be limited to a similar dynamic range by the resolution of the analog-to-digital converter. For a forward-scattering instrument the range of possible scattered intensities is so great that this is still inadequate. A change of method is required, rather than a mere improvement of the numbers. The best solution to this problem seems to be the suggestion of Gebhart et al.(30) to use a detector-interface combination with a logarithmic rather than a linear response to light intensity for forward scattering optical particle counters. This qualitative change in the nature of the instrumental response would have the added benefit of simplifying the calculation of the ratio of intensities by converting it into a subtraction of two quantities. A rather cursory search has revealed that there are several ways of designing a logarithmic interface with commercially available components at moderate cost.

DATA PROCESSING

The intensity measurements were controlled, collected and analyzed by a 12 bit microcomputer with a magnetic-core memory of 4096 words. (39) The magnetic-core memory was particularly convenient for instrument development because it retained programs while the instrument was turned off, but it permitted alterations of parts of the programs during the debugging process. A final model would undoubtedly use a combination of read-only memory with a fixed program and a smaller amount of read/write memory for data. Programs for the fiber counter were written and assembled on another computer with a more elaborate operating system, and were transferred to the device either by paper tape or through a data link to the larger machine. Although the data link could operate in both directions, it was never considered necessary to use the larger computer for data analysis. A combined printer/keyboard/paper-tape-reader (40) served to print the rather elaborate data required from each experiment for diagnostic purposes and permanent records, accept control statements from the operator, and read programs previously stored on punched paper tape. In a final model a much more compact device, such as one of the printers used in hand-held calculators, could serve adequately. A 4 digit LED display provided a single piece of real-time data to the operator when it was required during the course of a measurement; e.g., current fiber count or live time.

When the computer is turned on, the already resident operating program requests initial parameters from the operator: time of day, boundaries for histograms, sampling interval for the photon-counting interface, etc. It would be usual to begin with a calibration run measuring a spherical aerosol, in order to determine the factor f, which corrects for the ratio of the sensitivities of the two detectors. This factor has been remarkably stable at $f = 1.11 \pm 0.05$ for a period of about a month, but it is reassuring to have it remeasured regularly. Room air is adequately spherical (within $\Delta f \simeq 0.05$) in practice, despite the unavoidable alignment of any aspherical particles in the sample airstream, because f is to be compared with a typical factor of 8 used for fiber discrimination.

The simplified flow chart in Fig. 16 shows that the operator has entered several important parameters before the beginning of a fiber count.

These include the factor f just discussed, the threshold sensitivities a for detector A and b for detector B, and the threshold ratio of intensities r that defines a fiber. The termination of a measurement in the flow diagram is controlled by a maximum particle count n, or a maximum measuring time, whichever occurs first. The detectors are identified here as A and B, rather than as 1 and 2 as in the earlier discussions, to emphasize that this program will operate even with the detectors interchanged or with randomly oriented fibers.

The program operates with photon counts A or B in the same way that an electronic analog discriminator might operate with current or voltage levels proportional to light intensity. The computer awaits a data flag to signify the next photon count at appropriate points in the program. Within the first decision diamond in Fig. 16, the following criteria must be met. First in time, both A and B must be below their respective thresholds in order to assure that the device is not beginning a measurement in the middle of a pulse. Later, either A or B must exceed a threshold in a new photon count. This combination, determining an upward crossing of the threshold, defines the start of a "pulse" over threshold. The first-over-threshold and all subsequent photon counts of A and B are stored in a buffer section of the memory, until both A and B have crossed below their respective thresholds again. That crossing defines the end of a "pulse", in the second decision diamond of Fig. 16. At that point in the program, the computer stops accepting data and begins analysis of the previous pulse. The "dead time" that passes while it is doing this sort of thing is not included in the "live time" used in determining count rates.

The peak counts A and B are subsequently determined by searching the buffer area devoted to the pulse in memory. (One could have chosen the sum of counts to represent the pulse height instead of the peak, but it was felt at the time of the original design that the peak count would be less affected by possible alignment errors that might slightly truncate one detector's pulse. In practice little difference was noted when both

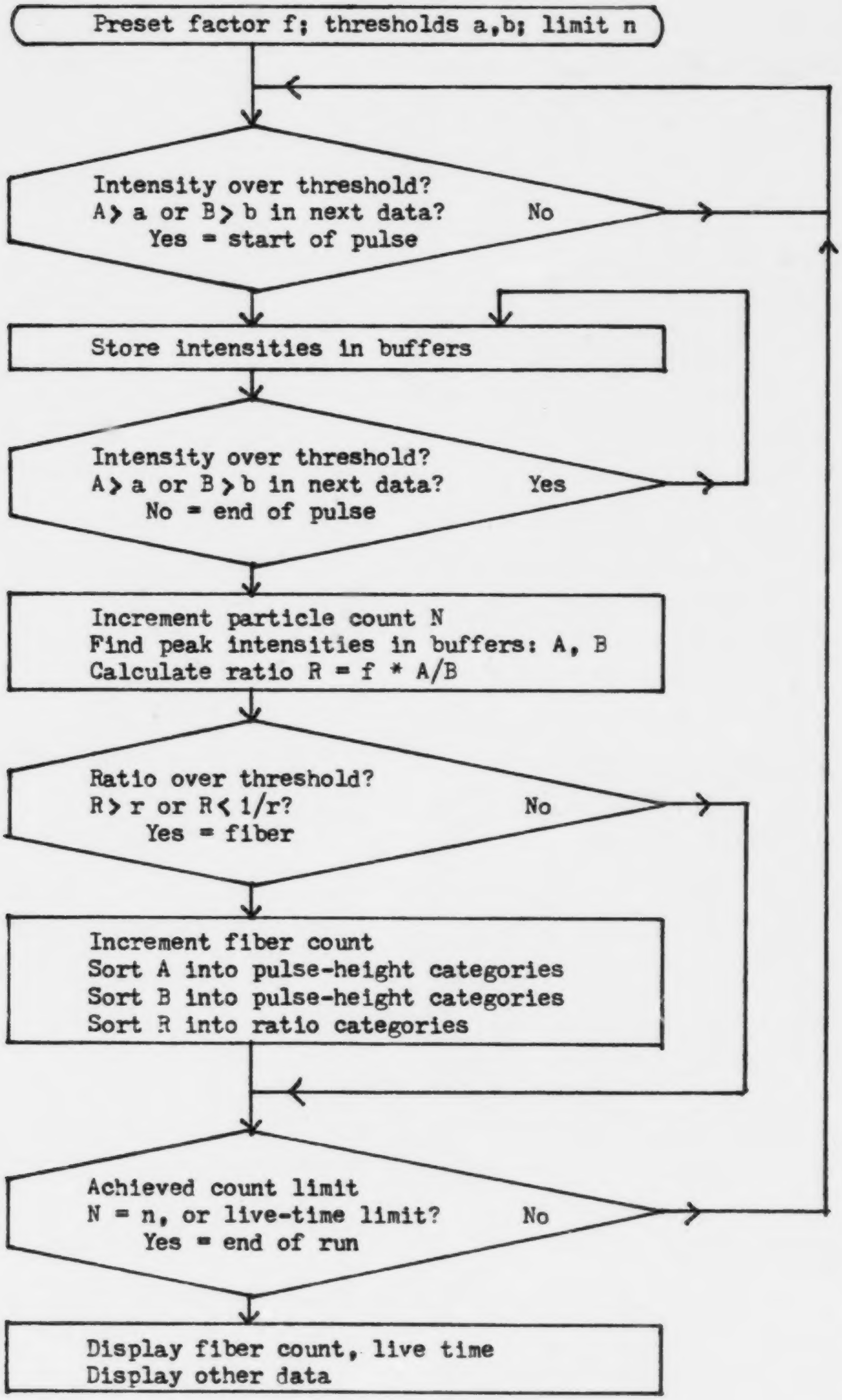
Preset factor f; thresholds a,b; limit n
Intensity over threshold?
A > a or B > b in next data?
Yes = start of pulse
No
Store intensities in buffers
Intensity over threshold?
A > a or B > b in next data?
No = end of pulse
Yes
Increment particle count N
Find peak intensities in buffers: A, B
Calculate ratio R = f * A/B
Ratio over threshold?
R > r or R < 1/r?
Yes = fiber
No
Increment fiber count
Sort A into pulse-height categories
Sort B into pulse-height categories
Sort R into ratio categories
Achieved count limit
N = n, or live-time limit?
Yes = end of run
No
Display fiber count, live time
Display other data

Fig. 16. Flow chart of fiber-counting program.

methods were tested.) The ratio of intensities R = f * A/B, corrected for detector sensitivities, should be near unity for a symmetric particle and quite different from unity for a fiber. Depending upon which detector was more brightly illuminated by the fiber, a value of R exceeding the threshold r, or less than its reciprocal 1/r, defines a fiber. Some early calculations for randomly oriented fibers indicated that r = 8 was a good choice, providing about a 25 percent counting efficiency for a collection of randomly oriented prolate spheroids having aspect ratios exceeding 4:1 and almost no sensitivity to aspect ratios less than 2:1. Rough tests with aligned fibers in the current device have indicated that r = 8 remains a good choice for aligned fibers, but it does not appear to be critical. Extensive tests with controlled aerosols have not been performed to optimize the choice of r, but the final value will probably lie in the range between 4 and 16.

Those pulses classified as due to fibrous particles are analyzed further. For each fiber the peak intensity A is sorted into one of 20 categories of pulse height, and the number stored in the appropriate bin is incremented by one. The bin boundaries, in units of photon counts, are adjustable under program control, or the bins can be made logarithmic, each one corresponding to a factor of 2 in peak intensity. When the data for a run are displayed, this results in a histogram of frequency of occurrence _vs_ pulse height, with the confusing axis units: photon counts for the abscissa and fiber counts for the ordinate. The histogram may be either linear or semi-logarithmic. The semi-logarithmic display was found to be more useful in general, because of the wide range of pulse heights encountered in forward scattering. The peak intensity B is sorted and its distribution printed in a similar manner. The ratio R of pulse heights is also sorted, and its distribution is printed. Thus, one can examine the effects of various choices of the threshold ratio of intensities r within a single run by examining the numbers in the histogram of ratios. Also, one can tell the frequency with which either detector A or detector B provided the brighter pulse in the fiber ratio. This provided a sensitive measure of fiber alignment. It was possible to tell that, with flow and maximum-electric-field alignment, detector A was never brighter (quantitatively, less than 0.1 percent of the time, etc.) than detector B for a fiber. It was also possible to see the shift in the pulse-height distribution in the brighter detector as the aligning electric field was increased.

The pulse-height distribution in the brighter detector, assumed to be in the forward lobe, is a good measure of particle volume for the smaller aligned fibers. Moreover, the size of this pulse is in itself a fair indicator of when it is a valid indicator of particle volume. Therefore, this feature of the detailed data analysis is likely to remain in a final model. The transformation to a logarithmic scale should probably precede the digitization in order to increase the dynamic range, and of course with aligned fibers only the brighter detector's pulse-height distribution needs to be displayed. This would be detector #1 in the previous discussions of scattering geometry. A distribution of ratios R is probably useful only in a developmental model or a very special application.

Proper timing is essential to the operation of the program of Fig. 16 in two senses. The data are presented asynchronously, with a data flag sent every (say) 102 microseconds to the computer, on the assumption that it is ready and waiting for the flag. Therefore, the previous data must have been read and tested for threshold criteria, and the proper program branches executed to store or clear the old data, before the new data arrive. During this process, a clock interrupt might occur (60 times each second), and the internal clock would need to be serviced without losing any data. The greatest difficulty in achieving sufficiently fast program timing is the internal, interrupt-driven clock routine, which probably should be replaced by an external clock. To avoid losing data without a trace, the photon-counting interface provides an error-interrupt signal if any data are not read. For the program of Fig. 16, which treats both detectors symmetrically, the shortest sampling time which permits proper operation is 110 microseconds. Another program, which takes advantage of knowing which detector would have the higher intensity, could shorten this interval appreciably.

The clock routines, which cause so much timing trouble, are essential to the correct operation of the instrument. The total fiber count must be divided by the live time, discussed earlier, in order to obtain a fiber count rate which can be converted to a concentration. The "live time" is the total time during which the fiber counter is able to accept a new fiber. The real-time duration of a measurement includes "dead time", during which the instrument is too busy to accept and count another fiber. When it takes a few milliseconds to process each particle, the live-time correction is not negligible, but it can be made accurately and automatically by some additions to the program of Fig. 16. These additions are present in the actual program used in the fiber counter. During the period when the computer is cycling through background-intensity measurements, waiting for an upward crossing of the threshold, the 60 Hz clock pulses are routed to a live-time clock. This occurs within the top diamond of Fig. 16, after the intensity has dropped below threshold. Once the presence of a pulse has been detected, whether it is a fiber or just a particle, the instrument is no longer open for business, and any clock pulses occurring after the diamond at the top of Fig. 16 are routed to the dead-time clock. This dead time continues until the program cycle gets back to the top diamond and at least one intensity measurement is below threshold. The 60 Hz clock rate is too slow to correct each particle's dead time, but it corrects a total measurement statistically. Dead-time losses are avoided. The penalty paid for dead time is merely a lengthened real-time duration of a measurement for a given live time. However, coincidence errors and serious effects of sub-threshold particles must be considered separately. One effect of a very dense cloud of sub-threshold particles should be discussed here. If such a dense cloud effectively holds the light intensity continuously above threshold, the instrument will be paralyzed in the dead-time regime. The live time will not be incremented, and in a laboratory situation no erroneous readings will result, although the experimenter's patience may be tried. In a field situation, where the device might be operating as an unattended fiber alarm, this condition would go undetected unless some sort of conspicuous warning signal were provided. The paralysis has been produced in laboratory tests by holding a lighted cigarette right at the intake tube.

In the actual programs corresponding to both Figs. 16 and 17, a measurement can be terminated by any one of three conditions: operator intervention, achievement of a preset maximum live time, or achievement of a preset total particle count n. In every case the correct live time for calculating fiber or particle concentrations is printed in the data display.

The factor f, needed to correct the quotient A/B to the ratio R of intensities, was measured by the calibration program whose flow diagram is shown in Fig. 17. The same program was used to test and debug many features of the optical and flow systems in the fiber counter. Actually this program shares many features with the fiber-counting program of Fig. 16, because they are coresident in the computer memory and use common subroutines. One difference is that the calibration program measures the characteristics of every pulse. Thus, the distributions of A and B pulse heights and of the ratio R pertain to the entire particle sample. A total fiber count can be extracted from the distribution of R, but the pulse-height distributions of all particles are inextricably mixed by this program. The calibration program calculates f as the ratio of the sum of all B pulse heights to the sum of all A pulse heights. If the calibration measurement has been made on a sample of either spherical or randomly aligned particles, the resulting factor f can be used in subsequent runs for calculating the ratio R. It was found in practice that turning off the electric field and using room air gave a value of f differing by only about 5 percent from that measured for polystyrene latex spheres, and that this was adequate. The instrument is, therefore, self-calibrating when the memory contains this program as well as the fiber-counting program.

A feature that helped in debugging the developmental model is the ability to display a distribution of "pulse widths" W. The integer W is the number of sampling intervals for which the intensity exceeds threshold, measuring the temporal duration of the light flash in units of (typically) 100 microseconds. For simplicity this feature was omitted from the flow chart of Fig. 16, even though it was present in the program. A criterion

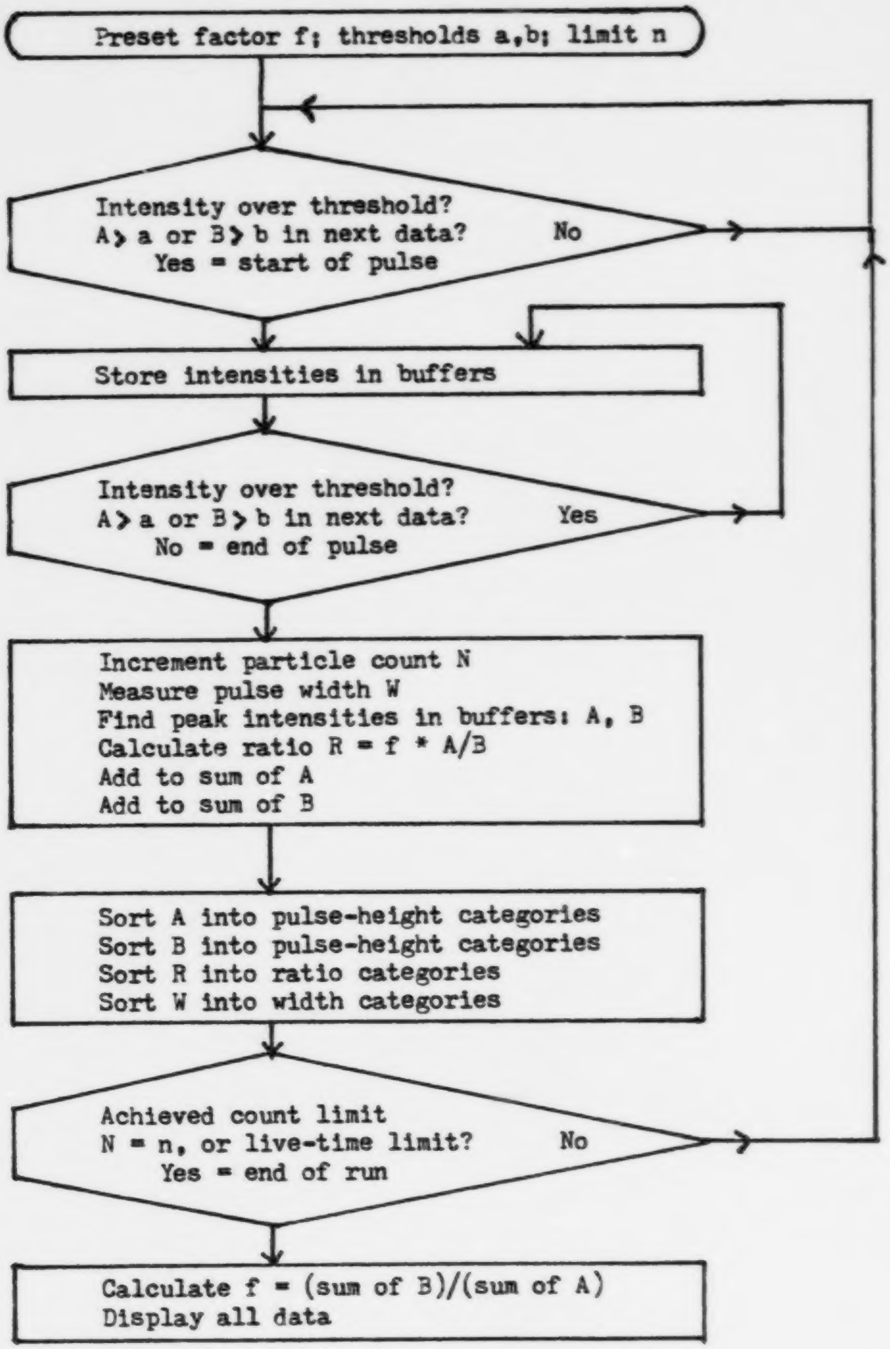
Preset factor f; thresholds a,b; limit n
Intensity over threshold?
A> a or B> b in next data?
Yes = start of pulse
No
Store intensities in buffers
Intensity over threshold?
A> a or B> b in next data?
No = end of pulse
Yes
Increment particle count N
Measure pulse width W
Find peak intensities in buffers: A, B
Calculate ratio R = f * A/B
Add to sum of A
Add to sum of B
Sort A into pulse-height categories
Sort B into pulse-height categories
Sort R into ratio categories
Sort W into width categories
Achieved count limit
N = n, or live-time limit?
Yes = end of run
No
Calculate f = (sum of B)/(sum of A)
Display all data

Fig. 17. Flow chart of calibration program.

for acceptable pulses, not shown in either flow diagram but accessible to both programs, can be a restriction on the value of W. Under the usual conditions, W lies in the range 1-10. Setting a requirement that W be at least 2, rejected most of the spurious events ascribable to statistical fluctuations in the background count rate when the threshold had to be set very close to the background level, but kept most of the particles. Similarly, during the difficult period when the remnant dust particles drifting through quiet air in the laser beam outside the sample volume were causing problems, a requirement that W should not exceed 20 rejected most such particles, while keeping all legitimate ones.

A map of the computer memory as it was usually configured is shown in Fig. 18. The space allocations give a crude idea of how many features can be coresident in a memory of 4096 twelve-bit words.

7777(8)		4095(10)
	Paper-tape program loader	
7700		4032
7577		4031
	Data-link program loader	
7600		3968
7577		3967
	Input/output and clock subroutines	
4000		2048
3777		2047
	Calibration and fiber-counter programs and subroutines	
0200		0128
0177		0127
	Common variables and pointers	
0000		0000

Fig. 18. Map of memory allocations in the MP-12 computer. The numbers in the left-hand column are octal, while those in the right-hand column are decimal. The total memory size is 4096(10) twelve-bit words.

SECTION 5

THEORETICAL BACKGROUND

ALIGNMENT OF FIBERS

Aerosol fibers are aligned in the sampling volume of the instrument by a combination of the airflow and an applied electric field. It is convenient to discuss these influences separately before combining them.

The motion of long rods in fluids in the presence of a velocity gradient has been studied experimentally by Mason and his co-workers (37), and for Reynolds numbers closer to those in this instrument by Harris (38). Their work is based upon the original theoretical studies by Jeffery (39) of the motion of ellipsoidal particles in a viscous fluid. In this section of the report the theoretical work of Jeffery is combined with a long-known expression for the torque on a dielectric ellipsoid in a uniform external electric field, found in the textbook by Becker and Sauter (40).

The fibers will be modeled hereafter as long circular cylinders (rods) or equivalent prolate spheroids. The experimental work (37,38) shows this equivalence to be reasonable for the motions of particles in a viscous fluid. Because the fibers in realistic situations are not ideal shapes, the differences between models are probably less significant than those between either model and a real fiber.

The geometrical variables, for describing the orientation of a rod or an equivalent prolate spheroid, are illustrated in Fig. 19. Inertial effects are neglected, and the origin of the coordinate system rides with the center of the fiber at the average velocity of the fluid in the region. The y axis is chosen to point in the direction of the fluid velocity $\vec{u}$. The x axis is chosen to point in the direction of increasing fluid speed u, with values of the speed u and velocity gradient g similar to those of Eqs. (10)-(14) at the end of Section 4. Let $\vec{v}$ be the velocity of the fluid relative to the particle's center. Then, the relative velocity field (v_x, v_y, v_z) in the immediate neigborhood of the particle can be written in the simple form,

$$(16) \qquad v_x = 0,\ v_y = g\,x,\ v_z = 0,$$

where g is a positive number, the radial velocity gradient in the sample inlet tube, defined by Eq. (9) of Section 4. For a fiber in the sample inlet tube, +y is directed downstream along the axis of the tube, and +x is directed radially inward toward that axis. The angular coordinates of the particle's assumed axis of rotational symmetry are Θ, measured from the z axis, and ϕ, measured from the x axis to the projection in the xy plane. The length of the cylindrical rod is labeled 2a', and its diameter is 2b'. The corresponding prolate spheroid has its semimajor axis denoted by a, and equal semiminor axes, $b = c < a$. Unfortunately, these conventions are not universal in the literature. The choice of fiber models having reflectional symmetry forces the solutions for their motions to be invariant to the transformation: Θ to $(\pi - \Theta)$ and ϕ to $(\pi + \phi)$.

For a prolate spheroid in the geometry of Fig. 19, when inertial effects are negligible compared to viscous effects, Jeffery gives the angular velocities of the particle as solutions to the differential equations,

$$(17) \qquad \frac{d\phi}{dt} = \frac{g(a^2 \cos^2 \phi + b^2 \sin^2 \phi)}{(a^2 + b^2)} ,$$

$$(18) \qquad \frac{d\Theta}{dt} = \frac{g(a^2 - b^2) \sin\Theta \cos\Theta \sin\phi \cos\phi}{(a^2 + b^2)} .$$

If $\phi = 0$ and $\Theta = \Theta_0$ at $t = 0$, then

$$(19) \qquad \tan\phi = \delta \tan\left(\frac{g\delta t}{\delta^2+1}\right) ,$$

$$(20) \qquad \tan\Theta = \frac{C\delta}{\sqrt{\delta^2 \cos^2\phi + \sin^2\phi}} .$$

The dimensionless constants in the solution are the aspect ratio,

(21) $\delta = a/b$,

and the orbit constant,

(22) $C = \delta \tan \Theta_0$.

The solution for ϕ is independent of Θ. The nature of the solution for Θ depends upon the initial conditions, described by the orbit constant C. If $C = 0$, then $\Theta = 0$ and ϕ is irrelevant; the spheroid's axis is

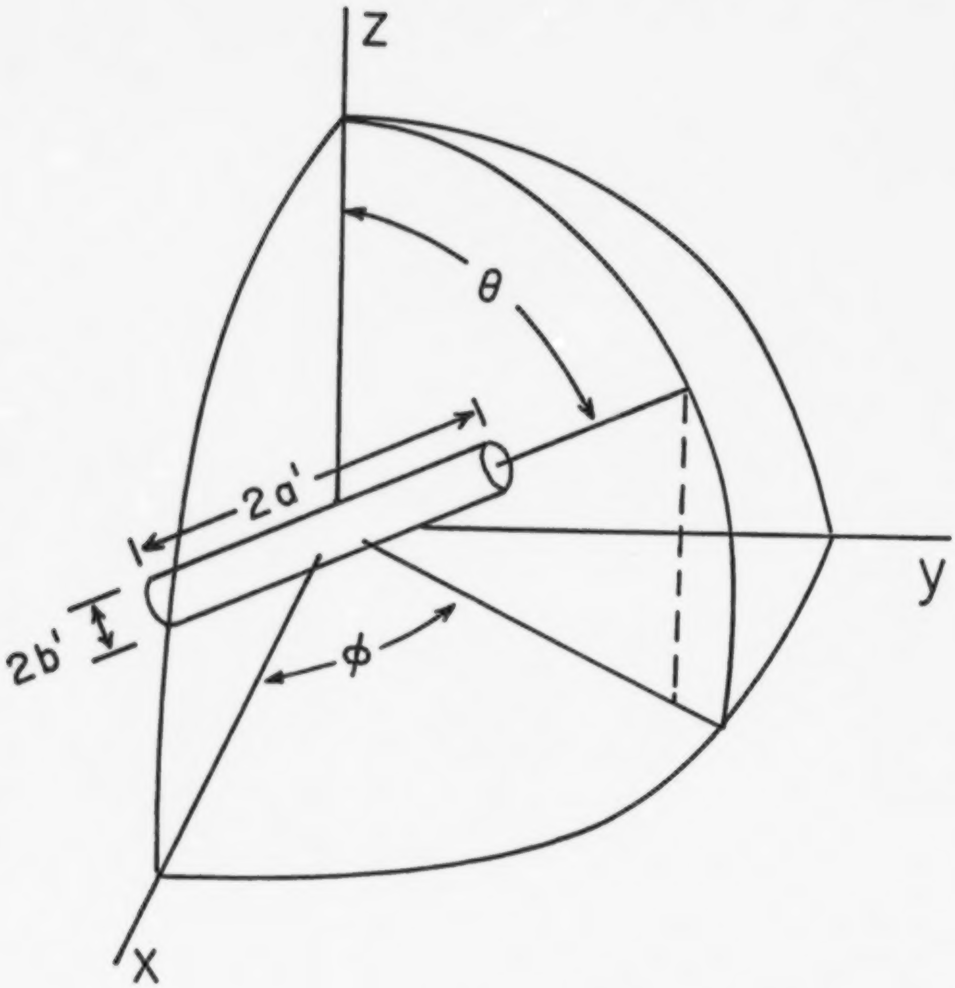

Fig. 19. The orientation of a long, circular cylinder in a coordinate system related to the velocity and electric fields. The fluid velocity is in the positive y direction, and the speed increases in the positive x direction. The electric field is parallel to the fluid velocity. A similar figure pertains to prolate spheroids.

stable along the z axis. On the other hand, if $C = \infty$, then $\Theta = \pi/2$, and the axis rotates according to Eq. (19) in the xy plane. This simpler planar solution exhibits much of the interesting physics, and will be discussed in connection with an applied electric field.

Two extreme cases give some insight:

A) the sphere ($\delta = 1$),

(23) $\phi = \omega t, \omega = g/2, \Theta = \Theta_0$,

with a period of rotation,

(24) $T = 2\ (2\pi/g)$;

B) the long, thin needle ($\delta >> 1$),

(25) $\tan\ \phi = \delta \tan(gt/\delta)$,

(26) $T = \delta\ (2\pi/g)$.

The sphere rotates with constant angular velocity g/2 around the z axis. The long, thin needle rotates in spurts, being nearly stationary at $\phi = \pi/2$ and rotating rapidly at $\phi = 0$; it tumbles. Because the needle spends most of its time where its angular velocity is low, near $\phi = \pi/2$, there is a statistical preference for that orientation in a random collection of such particles. The three-dimensional nature of the problem challenges one's visualizing abilities, but a simplifying restriction to the planar solution ($C = \infty$) should permit one to see from Eqs. (17 and (18) that an extremely thin particle ($\delta >> 1$) is nearly in an equalibrium position when it is aligned with the flow ($\phi = \pi/2$). A more careful inspection of these equations reveals that this is also the case for other values of C and $\phi = \pi/2$.

The qualitative conclusion of this analysis is that straight, long, thin fibers should be preferentially but not completely aligned in a steady-state Poisseuille airflow like that in the sample inlet tube. A comparison of the speed, about 10^3cm $\sec^{-1}$, with the velocity gradient, about 10^4 $\sec^{-1}$, indicates that this preferential alignment should be well established within one cm of flow along the tube.

When inertial effects are negligible, the force on a stationary point particle in a moving fluid is the same as the force on that particle moving in a stationary fluid; velocities are additive and only the relative velocities of particle and fluid significant. Therefore, one could derive the torque on a fiber, held stationary in a viscous fluid with a velocity gradient, from the angular velocity of the free fiber at the same orientation. If the inertial effects in the fluid are to be negligible, the Reynolds number N must be small. For this case,

$$(27) \qquad N \sim \frac{v\,a\,\rho}{\eta} = \frac{a^2\,g\,\rho}{\eta} ,$$

where v is the relative velocity of the air, ρ is its density, η is its viscosity, and g is the velocity gradient. If $g = 3 \times 10^4\ \mathrm{sec}^{-1}$ and a = 10 micrometers, N has a value less than unity, and one can safely conclude that inertial effects in the fluid are small. If the inertial effects in the particle are negligible, the damping time for the rotational velocity must be much less than the period of rotation. A commonly used expression for the torque on a prolate spheroid, rotating about the short b axis, in the approximation $\delta > 5$, is given by Tanford (41):

$$(28) \qquad t' = -\,\zeta\omega$$

with

$$(29) \qquad \zeta \simeq \frac{16\,\pi\eta\,a^3}{3(-1+2\,\ell n\ 2\delta)}$$

where ω is the angular velocity relative to the fluid and t' is the viscous torque. One remarkable aspect of Eq. (29) is the very weak dependence upon the value of the aspect ratio, δ , for $\delta > 5$. The viscous drag coefficient ζ depends primarily upon the length a. Also, if one compares spheroids of equal aspect ratio δ, ζ is exactly proportional to the volume. The moment of inertia of the spheroid about the b axis is, for $\delta \gg 1$, and a particle of density 1 gm cm^{-3},

$$(30) \qquad I = \frac{4\pi\ a^5}{15\delta^2} .$$

Combining Eqs. (28)-(30) gives a characteristic time, in which the angular velocity about the b axis decreases to 1/e of its departure from equilibrium:

$$(31) \qquad T' = \frac{I}{\zeta} = \frac{a^2(-1 + 2\ell n\ 2\delta\ )}{20\ \eta\ \delta^2} .$$

For a = 10 micrometers and $\delta = 10$, this gives $T' = 1.4 \times 10^{-5}$ sec, which is much smaller than the rotational period $T = 2 \times 10^{-3}$ sec, obtained from Eq. (26) with these parameters and $g = 3 \times 10^4$ sec^{-1}. Therefore, one can conclude that the inertial effects of the particle are also negligible and Jeffery's analysis is applicable. This was of some concern here, because the cited experimental work (37, 38) verifying the applicability of Jeffery's analysis, was done with smaller gradients in water, which has a higher viscosity than air.

The discussion will now be limited to planar rotations for simplicity ($C = \infty$). Since one can think interchangeably of the rotation of either the particle or the fluid, the torque on a stationary spheroid with $\delta > 5$ and orientation ($\Theta = \pi/2$, ϕ) is given in the velocity field of Eq. (16) by combining Eqs. (17), (28) and (29):

$$(32) \qquad t' = + \zeta\dot{\phi} \ ,$$

$$(33) \qquad t' = \frac{16\pi\eta\, a^3 g(\sin^2\phi + \delta^2 \cos^2\phi)}{3(-1 + 2\,\ell n\, 2\delta)\ (1+\delta^2)} \ .$$

It is this torque which must be opposed by an externally applied electric field if the fibers are to be locked into complete alignment near $\phi = \pi/2$, with no tumbling.

Asbestos fibers in an external electric field are modeled by prolate spheroids made of a uniform dielectric material in a uniform electric field. The magnitude of the induced electric dipole moment is largest, and therefore the potential energy of the particle in the electric field is lowest, when the long dimension of the spheroid is aligned parallel to the field. The differences between this model and reality are believed to be no worse than the differences between one fiber and another.

The torque t" on a prolate dielectric spheroid placed in a uniform electric field E, with an angle ψ between the symmetry axis and the field, is obtained from Becker (40) after conversion to SI units:

$$(34) \qquad t'' = \frac{-2\pi\, \chi^2\, \varepsilon_0\, ab^2\, (B-A)\, E^2 \sin 2\psi}{3(1 + \chi A)\ (1 + \chi B)}$$

when a is the semimajor axis and b is the semiminor axis of the spheroid. If κ is the relative dielectric constant, then χ is equal to $\kappa-1$, and ε_0 is as usual the permittivity of free space. The dimensionless quantities A and B are related to the depolarization factors along the principal axes of the spheroid:

$$(35) \qquad A = \frac{ab^2}{2} \int_0^\infty \frac{d\lambda}{(a^2 + \lambda)3/2(b^2+\lambda)} \quad ,$$

$$(36) \qquad A + 2B = 1.$$

When the aspect ratio, $\delta = a/b$, exceeds 5, one may write

$$(37) \qquad A(\delta) \simeq (\ln^2\delta - 1)/(\delta^2 - 1).$$

In terms of the size parameter a, the aspect ratio δ, and the function $A(\delta)$, the torque can be written

$$(38) \qquad t'' = \frac{-\pi\varepsilon_0 a^3 (1-3A) E^2 \sin 2\psi}{3\delta^2 \left[A + 1/\chi\right] \left[\tfrac{1}{2}(1-A)+1/\chi\right]}.$$

In the absence of other torques this would produce a stable equilibrium at $\psi = 0$, and an unstable equilibrium at $\psi = \pi/2$. The maximum torque would occur at $\psi = \pi/4$.

The discussion now centers on a combination of viscous and electric torques. The electric field $\vec{E}$ is applied parallel to the fluid velocity $\vec{u}$, in the +y direction. For simplicity only fibers rotating in the xy plane are considered. Both t' of Eq. (33) and t" of Eq. (38) are then torques about the z axis. The angle ψ of Eq. (38) can be identified with $(\phi - \pi/2)$, as in Fig. 20. The net torque is $t = t' + t''$:

$$(39) \qquad t = \frac{4}{3}\pi a^3 \left\{ \frac{4\eta g\left[1 + (\delta^2-1)\sin^2\psi\right]}{(-1 + 2\,\ell n\, 2\delta)(1+\delta^2)} - \frac{\varepsilon_0 (1-3A) E^2 \sin 2\psi}{4\delta^2 \left[A + 1/\chi\right] \left[\tfrac{1}{2}(1-A)+1/\chi\right]} \right\}$$

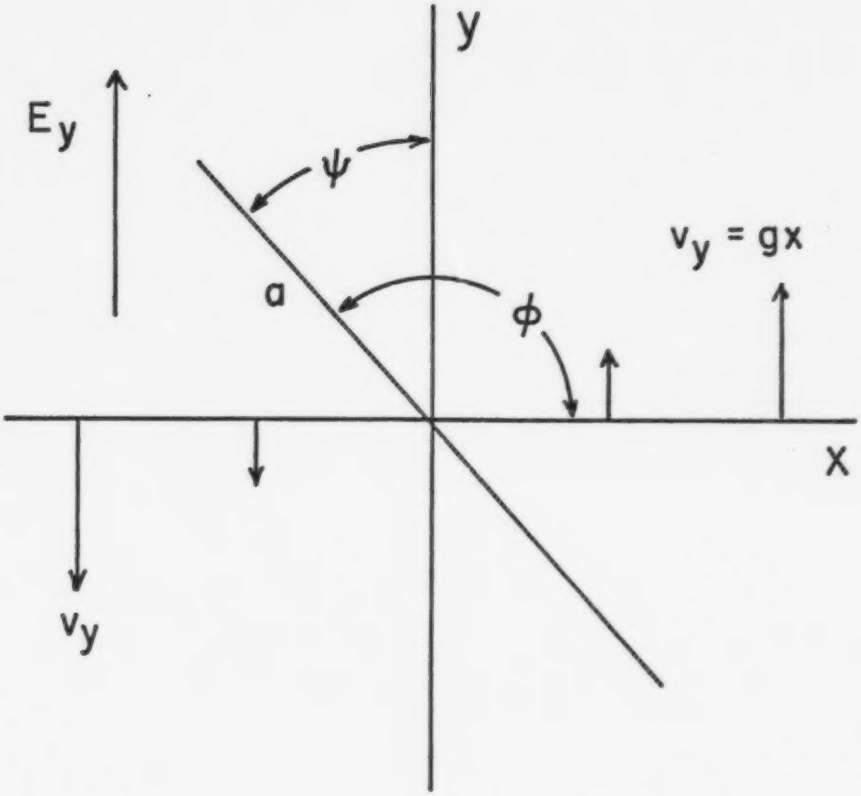

Fig. 20. The geometry for the combined viscous and electric torques on a prolate dielectric spheroid of semimajor axis a, in an electric field ($E_y = E$) and a flow field ($V_y = g\ x$).

This equation has the form $t = C_1 [1 + (\delta^2 - 1) \sin^2 \psi] - C_2 \sin 2\psi$. For negative values of the angle ψ, both viscous (C_1) and electric (C_2) terms tend to decrease $|\psi|$, and thereby to maintain an alignment near $\psi = 0$. For zero and small positive ψ the electric torque (proportional to C_2) is a restoring torque, but the viscous torque tends to increase ψ. The competition between these two terms is illustrated in Fig. 21, where the electric term dominates between the angles ψ_1 and ψ_2 for the particular values of C_1, C_2 and δ^2 chosen in the figure. In a case like that in Fig. 21, there will be a stable equilibrium orientation at the angle ψ_1. Particles having angles larger than ψ_2 will be flipped all the way to $\psi = \pi$ (equivalent to $\psi = 0$), where they, too, will find an equilibrium orientation. Whether an equilibrium orientation exists, depends upon whether the two curves of Fig. 21 cross; i.e., upon the parameters in Eq. (39). The experiments with the fiber counter indicate that a stable alignment can be produced in the instrument with fields of a few kilovolts per centimeter.

Consider the dependence upon the length 2a and the aspect ratio δ. The net torque in Eq. (39) is proportional to a^3, the only size dependence. For a fixed aspect ratio, the competition between electric and viscous torques is independent of the length of the spheroid. Consider next the dependence of the factor within curly brackets { } upon the aspect ratio. For large values of δ, both viscous and electric terms have factors of δ^2 in their denominators. However, for large angles ψ, the viscous term has a contribution of $\delta^2 \sin^2 \psi$ to its numerator, which dominates weaker (essentially logarithmic when χ is finite and δ is large so that $A << 1/\chi$) dependences upon δ, of the remaining factors multiplying δ^{-2} in each term. Therefore, at large angles particles with aspect ratios much larger than unity will tend to be dominated by the viscous torque and to flip quickly to $\psi = \pi$, as implied by Eq. (17). For small angles, on the other hand, where an equilibrium orientation might be established by a cancellation of the two torques before the $\delta^2 \sin^2 \psi$ term takes over, the competition between the viscous, constant, term and the electric, $\sin 2\psi$, term is controlled by the logarithmic dependences upon δ, and is not strongly dependent upon the aspect ratio.

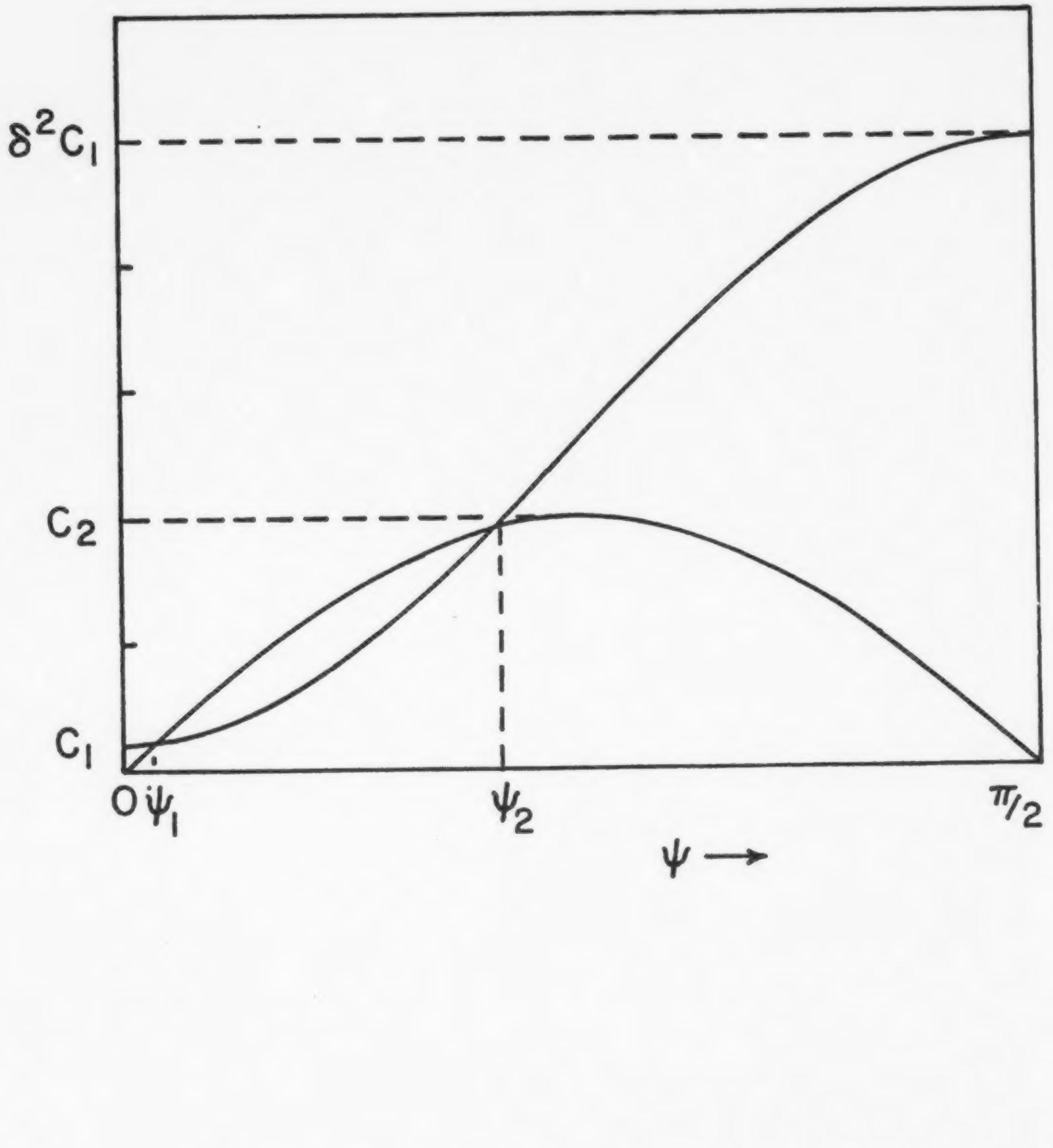

Fig. 21. Graphs of the viscous torque, $C_1 \left[1 + (\delta^2 - 1) \sin^2 \psi\right]$, and the negative of the electric torque, $C_2 \sin 2\psi$, for a fictitious case where $C_1 = 1$, $C_2 = 10$, and $\delta = 5$. Particles with orientations between 0 and ψ_2 will be rotated to a stable equilibrium at ψ_1.

Using SI values for η (air) = 1.81×10^{-5} and $\varepsilon_0 = 8.85 \times 10^{-12}$, the operating parameters of the real fiber counter are most conveniently expressed in the following units:

$$a' \ (\mu\mathrm{m}) = 10^6 \ a \ (\mathrm{m}), \qquad (40)$$
$$g' \ (\mathrm{msec}^{-1}) = 10^3 \ g \ (\mathrm{sec}^{-1}),$$
$$E' \ (\mathrm{kV/cm}) = 10^5 \ E \ (\mathrm{V/m}).$$

Then, Eq. (39) becomes

$$t = 10^{-20} \ (a')^3 \ g' \left\{ \frac{30.3 \left[1+(\delta^2-1)\sin^2\psi\right]}{(-1 + 2 \ \ell n \ 2\delta)(1+\delta^2)} - \frac{9.26 \ F(1-3A) \ \sin 2\psi}{\delta^2 \left[A + 1/\chi\right]\left[\tfrac{1}{2}(1-A)+1/\chi\right]} \right\} \qquad (41)$$

where the relative strengths of the flow and electric fields are specified by

(42) $F = (E')^2/g'$ in the (here) convenient units of $(\mathrm{kV/cm})^2$ msec.

One might choose typical values of $E' = 3$ and $g' = 33$ from the description of the device in Section 4; then $F = 0.27$. For these values, Eq. (41) does not predict an equilibrium orientation for values of the susceptibility χ less than about 20. The best estimate from the literature seems to be $\chi = 6$ (43); yet the observed alignment was essentially complete. It might therefore be concluded that some sort of conductivity of the fibers raised the effective susceptibility above that of macroscopic samples, even though the humidity was very low. If one explores the alignment predicted by Eq. (41) for a conducting fiber ($\chi = \infty$) having an aspect ratio of about $\delta = 10$, he finds that a fluid flow with $g' = 33$ msec^{-1} requires an E' of about 2 kv/cm to produce an equilibrium orientation. If one considers that the fibers are already statistically aligned by the flow field, then perhaps the augmenting effect of the electric field would be significant, even for fields too small to lock the fibers into one orientation.

A study of the statistical alignment predicted by Eq. (41), even when an equilibrium orientation is not achieved, can be made within the limits of the planar-rotation model. By comparing the times spent by a freely rotating particle in different angular intervals, one can show that in a large ensemble of identical particles the probability dP of finding the orientation within the interval ψ to $\psi + d\psi$ is inversely proportional to the angular velocity $\dot{\psi}$. In the regime of negligible inertia considered here, the angular velocity $\dot{\psi}$ of a rotating particle will be proportional to the torque $t(\psi)$ that would be felt if it were held stationary at that orientation:

$$(43) \qquad dP = p(\psi)\, d\psi \propto d\psi / t(\psi).$$

Probability distributions were generated numerically from Eqs. (41)-(43) for various values of F, χ and δ.

Figure 22 shows the fraction of particles having ψ less than 20 degrees, for spheroids with $\chi = 6$ and two values of δ, plotted as a function of F. Notice that there is a strong alignment, as an equilibrium orientation is established at a small angle, for F about 0.8 in these units. For $\chi = 6$ the critical value of F is not very sensitive to δ, as expected from the previous discussion. Also, the fractional alignment is not much affected by the electric torque below F = .5; the onset of the equilibrium alignment is quite sudden. The critical value of F = .8 corresponds to an electric field strength of E' = 5 kV/cm if g' = 33 msec.^{-1} Either this estimate of g' is too high, or the susceptibility is higher than 6, because the experiments showed a definite effect of the electric field well below E' = 3 kV/cm.

Figure 23 shows an extreme case that illustrates the effect of a high susceptibility. The figure shows the fraction of particles having ψ less than 20 degrees for spheroids having $\chi = \infty$ (equivalent to conducting spheroids) and two values of δ. Notice that the critical field ratio F is now lower for large values of δ, and drops to about 0.07 at $\delta = 10$. Thus, this is a possible explanation for the observed alignment in low fileds; but the low humidity in the experiment makes a surface conductivity unlikely. The GCA instrument, which takes advantage of a surface conductivity to hold the fibers perpendicular to the flow field, has some problems with operation below 20 percent relative humidity (1).

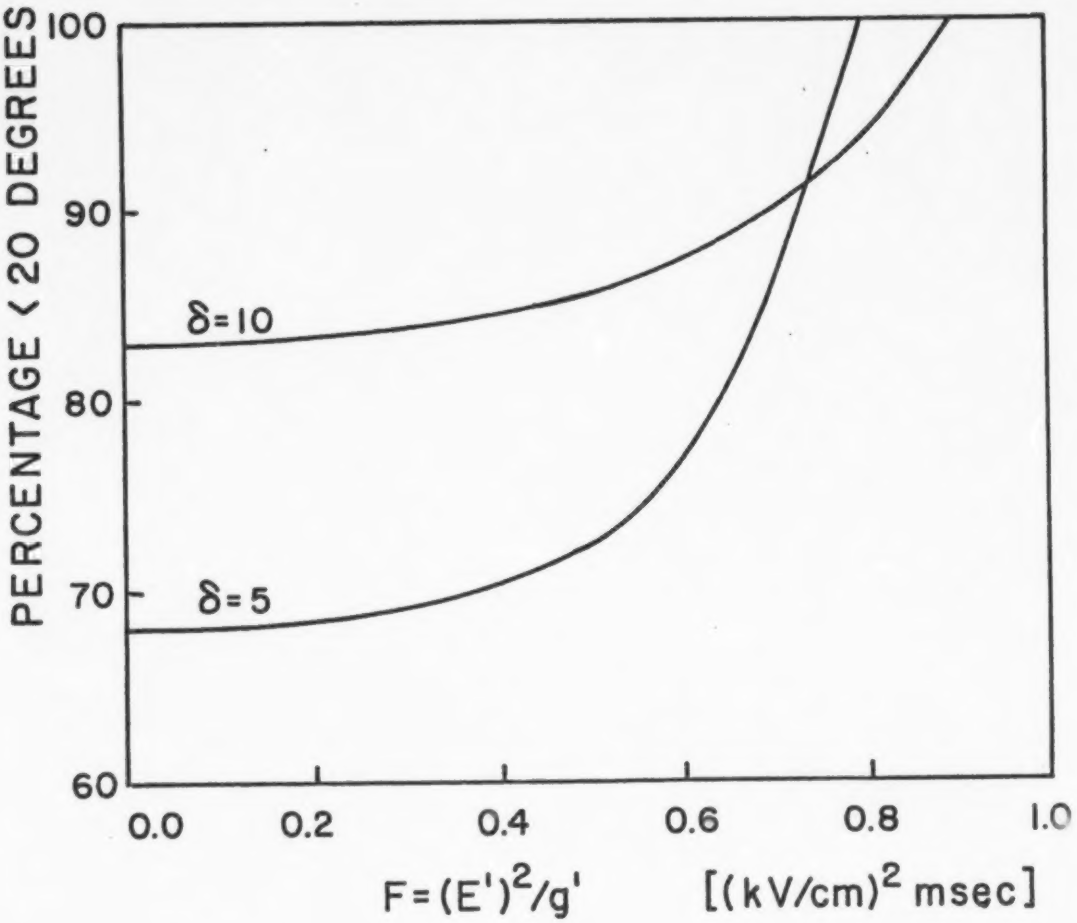

Figure 22. The fractions of spheroids with axes making an angle ψ less than 20 degrees with the electric field direction, for a susceptibility of $\chi = 6$ and two aspect ratios δ, as functions of the ratio F of electric to viscous field strengths. The unusual units of F are appropriate to the actual fiber counter.

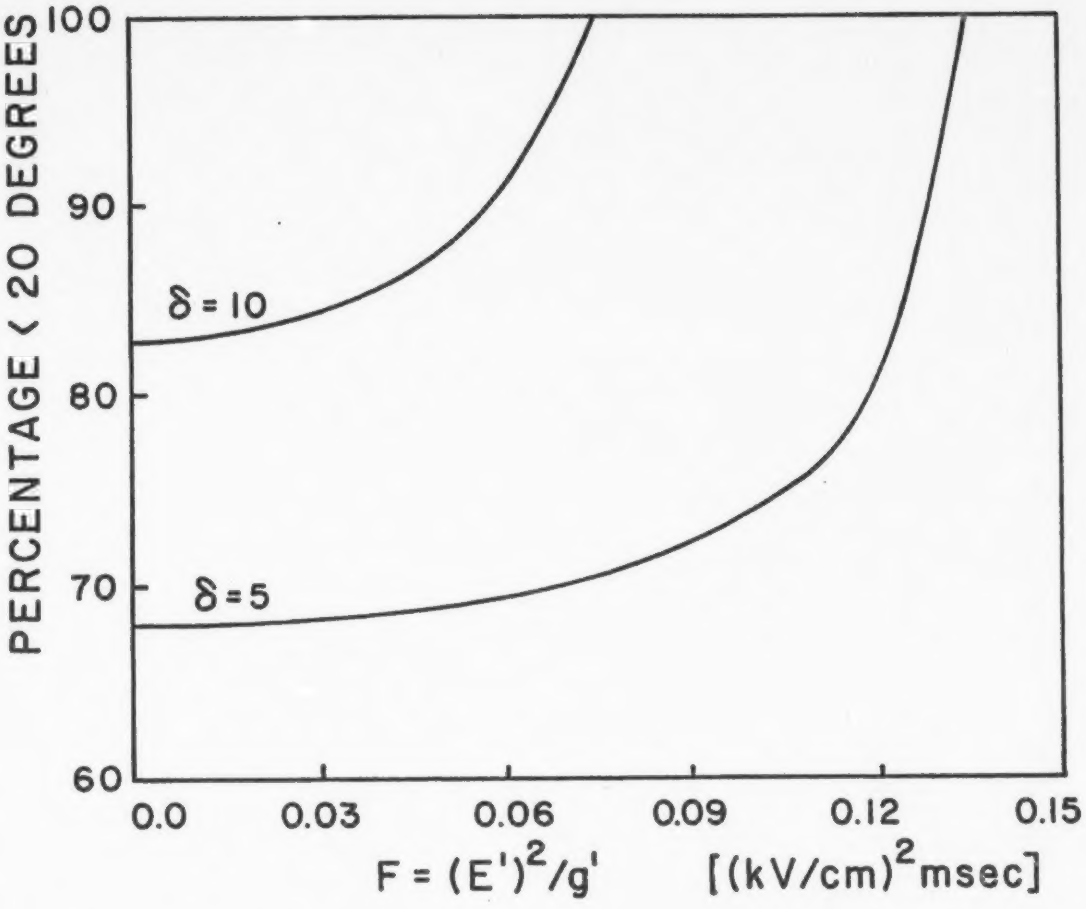

Fig. 23. The fractions of spheroids with axes making an angle ψ less than 20 degrees with the electric field direction, for a susceptibility of $\chi = \infty$ (conducting spheroids) and two aspect ratios δ, as functions of the ratio F of electric to viscous field strengths. The unusual units of F are appropriate to the actual fiber counter

One effect that has not yet been considered is that the velocity gradient in the free-jet region of the sampling volume is likely to be considerably less than it is in the sample inlet tube. Not only is the jet wider there, but the regions of highest gradient near the capillary walls are most quickly altered from their values in the tube as they sweep up adjacent air. The treatment of the free jet in Section 4, based on the theory by Schlicting (25), as modified to fit the experiments of Andrade and Tsien (26), is probably only approximately applicable, but it does have the advantage of providing an analytic expression for the velocity gradient, in Eqs. (3)-(6) of Section 4. In terms of the values for this instrument at the scattering volume, these become:

(44) $$z' = z + z_0 = 0.5 + 0.080\ N\ b = 2.2\ \text{cm},$$

(45) $$J = \rho \langle u \rangle = 1.16\ \text{gm cm sec}^{-1},$$

(46) $$\xi = \frac{1}{4\nu}\left(\frac{3J}{\pi\rho}\right)^{\frac{1}{2}}\frac{r}{z'} = 23\ r,\ \text{for } r \text{ in cm},$$

(47) $$u(r,z) = \frac{347}{(1 + 132\ r^2)^2}\ \text{cm sec}^{-1}.$$

Notice that the central velocity has dropped from its value of 1400 cm/sec. in the tube by a factor of four. The total airflow is then:

(48) $$Q = 2\pi\int_0^\infty u(r)\ r\ dr = 8.2\ \text{cm}^3\ \text{sec}^{-1},$$

indicating the entrainment of air at the edges of the flow, since $Q = 5\ \text{cm}^3\ \text{sec}^{-1}$ in the tube. J, not Q, is conserved in this theory. The velocity gradient, averaged over all volume elements passing a fixed cross section in a given time interval is, in analogy to the expression of Eq. (8) within the tube,

(49) $$\langle du/dr \rangle = 2\pi\int_0^\infty u\ (du/dr)\ r\ dr/Q\ .$$

This expression has been evaluated for the values above, appropriate to a flow of 5 $\text{cm}^3\ \text{sec}^{-1}$ in the sample tube, at a sample volume 5 mm beyond the end of the tube,

(50) $$\langle du/dr \rangle = 650 \text{ sec}^{-1}, \text{ or } g' = 0.65 \text{ msec}^{-1}.$$

The ratio of strengths of the two torque terms depends upon F. A reduction of g' from 33 to 0.65 msec^{-1} in the sample volume would correspond to a critical field E' of only 0.7 kV/cm when the susceptibility has the reasonable value, $\chi = 6$. Of course, quantitative agreement is not to be expected, since this discussion has dealt with average values in a very approximate theory, but this reduction in the average velocity gradient on leaving the sample inlet tube is a reasonable explanation of the observed alignment effects at electric fields of a few kV/cm, which does not require any assumption of surface conductivity in the fibers at low humidities.

The true mixture of χ, δ, g, and E throughout the sample volume is not likely to be known, and in any case the model is oversimplified. The treatment here is designed to show that complete alignment of all fibers, as observed in the experiment, could have been predicted from reasonable parameters applied to an approximate model. It is not likely to be useful as a means of predicting selective alignment of some fibers without a great deal more work.

LIGHT SCATTERING AND PARTICLE DIMENSIONS

Measuring the dimensions of small particles by means of the ratio of the intensities of light scattered in two directions is an unusual but not entirely new technique. It was proposed by Hodkinson (44) and used by Gravatt (45) and others. What is required for the application of this technique to an asbestos fiber counter is a theory that makes quantitative the fiber discrimination implied by Fig. 1 in the geometry of Fig. 4. We do not need a detailed, exact theory of the light scattering from particles of arbitrary shape, but rather an approximate, semiquantitative theory of scattering that can provide an adequate answer to the question, "What does it measure?"

It will be necessary for simplicity to calculate as though all fibers were needlelike (long, straight and thin). Reservations about realistic shapes will be inserted from time to time, especially concerning chrysotile fibers, but the reader may have to remind himself that we are talking about a model of real particles. Definite values of dimensions refer to "equivalent needles" in the belief that such an equivalence exists for a class of particles not too far from the ideal. Even within this restriction the answer to the question of what the instrument measures is not simple. The best answer seems to have two parts.

1) The choice of scattering angle is the main determinant of the minimum length of a "thin" particle that will be counted as a fiber, or the maximum diameter of a "long" particle that will be counted as a fiber.
2) For the smallest fibers, the intensity of light scattered into the brighter of the two detectors is primarily a function of fiber volume and index of refraction. For larger fibers, the brighter of the two intensities is a complicated function of many parameters, probably not truly monotonic with respect to particle size, but still useful as a crude criterion of size.

The criteria are clearest for straight fibers of small diameter, and become progressively less definite with increasing diameter and complexity of shape. For purposes of discussion we choose as a model shape the ellipsoid of revolution shown in Fig. 24, which becomes a sphere when its aspect ratio of length L to diameter D is unity. These spheroids are slightly more convenient than what might seem to be a more appealing circular-cylinder model. The difference between these models is almost certainly less significant than the fact that the real asbestos fibers are neither circular cylinders nor spheroids.

Let us now restrict ourselves to prolate spheroids, whose aspect ratios exceed unity, $L/D > 1$. Such a particle is assumed to be oriented with its length perpendicular to the incident beam of light. One detector (#1) views the light scattered at an angle Θ in the equatorial plane of the particle, as shown in Figs. 1 and 4. The other (#2) views the light scattered, at the same angle Θ, in the plane containing the long axis of the particle and the direction of the incident beam. A certain threshold-ratio of the two intensities, say $I_1/I_2 \geq r = 8$, is demanded in order that the particle be classified and counted as a "fiber".

The dependence of the relative intensity upon L or D can be seen in Fig. 25, calculated from the Rayleigh-Gans-Debye (RGD) approximation (46, 47) for spheroids:

$$I(\Theta) = I_0 \left[3 (\sin u - u \cos u)/u^3\right]^2, \tag{51}$$

where I_0 is the forward-scattered intensity,

$$u_1 = kD \sin \tfrac{1}{2}\Theta = 10\, D \sin \tfrac{1}{2}\Theta, \text{ for detector \#1,} \tag{52}$$

and

$$u_2 = kL \sin \tfrac{1}{2}\Theta = 10\, L \sin \tfrac{1}{2}\Theta, \text{ for detector \#2.} \tag{53}$$

When D and L are in microns, the convenient value of 10 per micrometer is about right for the wave number k of the incident laser light. The RGD approximation works best for particles much less than a wavelength across and having a low index of refraction, but the shape of the curve for thin fibers exceeding one micrometer in length and having a refractive index near 1.5 has been verified by numerical calculations

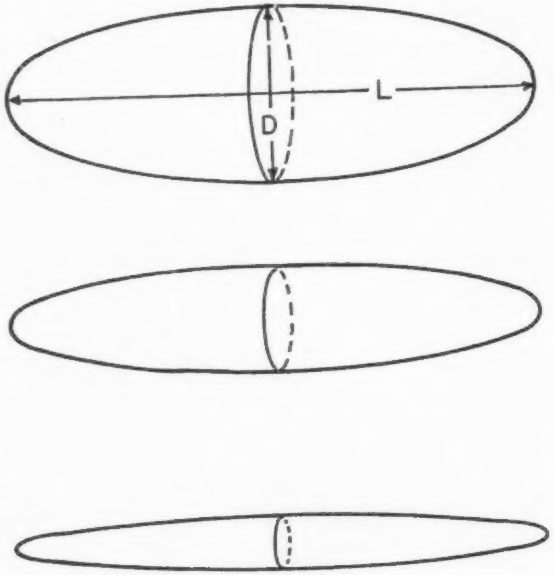

Figure 24. Three ellipsoids of revolution having the same length L and different diameters D. All are prolate spheroids.

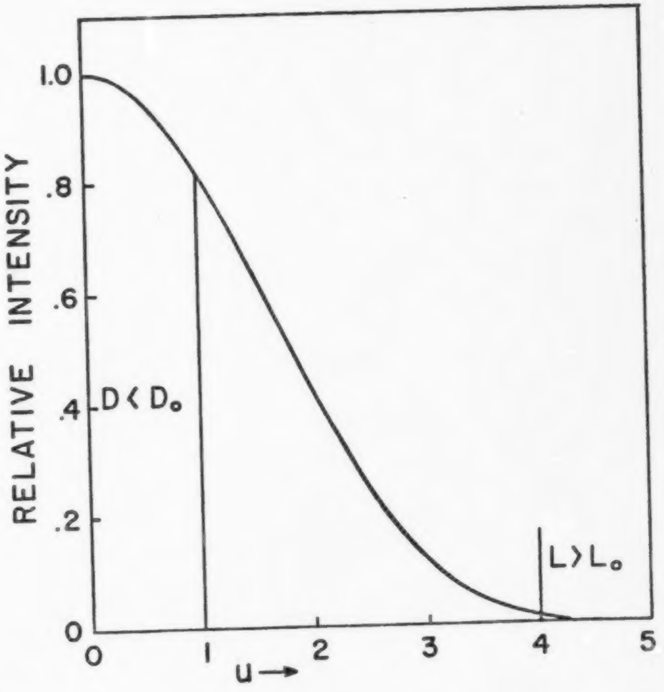

$$u = 10 \left\{ \begin{matrix} L \\ \text{or} \\ D \end{matrix} \right\} \sin(\theta/2)$$

Figure 25 The relative intensity of scattered light, normalized to unity in the exactly forward direction, for a spheroid particle, in the RGD approximation of Eq. (51).

described in Appendix B. The RGD approximation predicts the shape of the graph, of intensity vs scattering angle, well only in the range of angles within the first diffraction minimum:

(54) $$0 \leq u = 10 \text{ L} \sin \tfrac{1}{2} \Theta \lesssim 4.5.$$

By the "shape" of the curve $I(\Theta)$, as opposed to its absolute magnitude, we mean the graph of relative intensity, normalized to one at $\Theta = 0$. It is this normalized intensity that determines the performance of an instrument that measures particle dimensions by means of the ratio of intensities in two different directions. In Eq. (51) the normalized intensity is $I(\Theta)/I_0$. It is well known that the RGD approximation does not give good results for the absolute magnitude of the scattered intensity of light of wavelength 0.63 μm, for spheres of index 1.5, whose radii are several μm. However, Fig. 26 shows by a comparison with exact Mie calculations (46, 47) that the normalized intensity is fairly well predicted by the RGD approximation for this case, for angles within the first minimum of intensity. Similar calculations for nonspherical particles can be performed on large digital computers, but the number of parameters describing a particle's orientation increases from zero for spheres to two for cylindrically symmetric particles to three for particles of arbitrary shape, and the number of cases quickly becomes prohibitive. In Appendix B there are described a few calculations for spheroids, with an index of refraction appropriate to asbestos fibers, up to three wavelengths long. For the cases covered there, these calculations support our use of the RGD approximation as a guide.

For any value of the scattering angle Θ, there are a few special particles whose dimensions bound particular regions of fiber discrimination. First, consider a "thin" particle, modeled by a prolate spheroid for which the intensity in the brighter detector is almost as large as it would be at $\Theta = 0$, I_0. Referring to Fig. 25, we somewhat arbitrarily choose $u = 1$ as the upper limit on the diameter of such a particle, corresponding to about 80 percent of the maximum forward intensity. If D_0 is the diameter of the largest "thin" particle, Eq. (52) implies for "thin" particles the inequality of Eq. (55):

(55) $$D < D_0 \simeq \frac{1}{10 \sin \frac{1}{2} \theta}$$, defines a "thin" particle.

When the threshold-ratio of intensities is $r = 8$, we can see from Fig. 25 that, for a "thin" particle, detector #2 will measure an intensity less than the threshold value that will trigger a fiber count if u_2 is larger than approximately 3. Then, this defines the minimum length of a "thin" fiber as L_{thin}, given by Eq. (56):

(56) $$L > L_{thin} \simeq \frac{3}{10 \sin \frac{1}{2}\theta}$$, defines the minimum length of a "thin" fiber. The minimum aspect ratio for a "thin" fiber is $L_{thin}/D_0 = 3$.

Next consider a "long" particle, modeled by a prolate spheroid for which the scattered intensity in the unfavored detector #2 is very small, near or beyond the first diffraction minimum at $u \cong 4$ in Fig. 25. When u_2 is beyond this minimum, it defines for our purposes a "long" particle, of minimum length L_0.

(57) $$L > L_0 \cong \frac{4}{10 \sin \frac{1}{2}\theta}$$, defines a "long" particle.

For realistic "long" particles the intensity in detector #2 cannot be well predicted by any practical theory, but when selecting fibers with a threshold-ratio of intensities, $r = 8$, it seems safe to say that "long", "thin" particles having both $L > L_0$ and $D < D_0$ will certainly be counted as fibers. Also, "long" particles with slightly larger diameters, up to some $D_{long} > D_0$, can give intensity ratios as high as eight. However, the simple theory cannot predict the diameter limit for "long" particles to be classed as fibers, and a more realistic theory would also have to deal with more realistic shapes. Then,

(58) $D < D_{long}$ $(> D_0)$, defines the maximum diameter of a "long" fiber.

Realizing the limits of these approximations, we might conservatively combine the inequalities of Eqs. (55)-(58) into the following

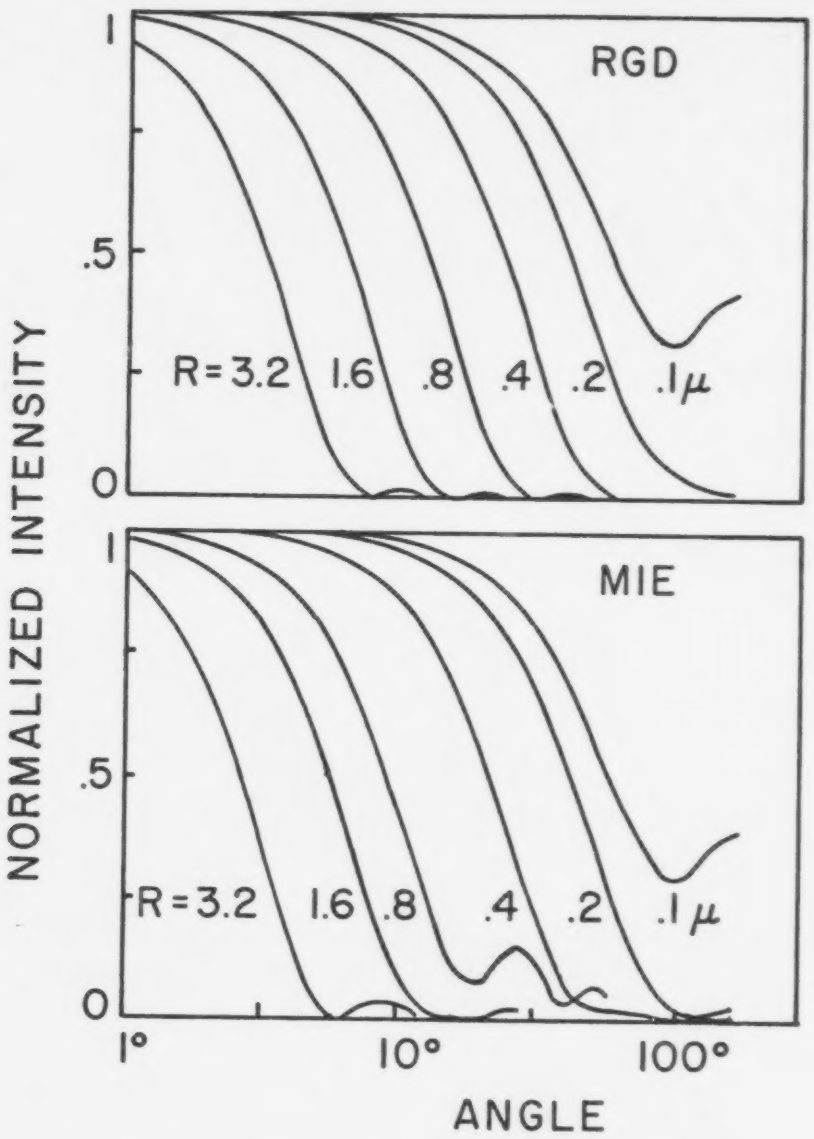

Figure 26. A comparison of the relative intensities, normalized to unity at a scattering angle of zero degrees, predicted by the exact Mie calculations and the RGD approximation for incident light of wavelength 0.63 μm on a sphere with an index of refraction of 1.5 and various radii. Note that the angle scale is logarithmic in order to display a factor of 32 in radii.

statement. Particles of longer lengths than

(59) $L_0 = 0.4/\sin \tfrac{1}{2}\Theta$ ($\overset{\sim}{=}$ 2.4 µm at the instrument's $\Theta = 20^0$),

and smaller diameters than

(60) $D_0 = 0.1/\sin \tfrac{1}{2}\Theta$ ($\overset{\sim}{=}$ 0.6 µm at the instrument's $\Theta = 20^0$),

will certainly be classed as fibers. There will also be some "thin" fibers counted with slightly shorter lengths ($L_{thin} = 0.3/\sin \tfrac{1}{2}\Theta$) and "long" fibers counted with somewhat larger diameters ($D_{long} > D_0$), but the difference does not seem worth retaining in such an approximate model. The "landmark" particle (L_0, D_0) will always be classified as a fiber. It has an aspect ratio of four. Its size depends upon the choice of scattering angle; larger angles are appropriate to smaller particles. This particle will be classed as a fiber for a wide range of choices of the threshold-ratio of intensities r. The exact choice of r affects mainly the borderline cases with L less than L_0 or D greater than D_0. These criteria are most strongly asserted for particles that are not too large (i.e., that are comparable to the "landmark" particle in size) and more weakly for particles of nonideal shapes.

On a two-dimensional, log-log plot of possible spheroid dimensions, each particle corresponds to one point. The point (L_0, D_0) discussed above is plotted as fiber F_0, at the intersection of the lines $L = L_0$ and $D - D_0$, in Fig. 27A which is appropriate to a scattering angle of 20 degrees, as used in the actual instrument. For this angle $L_0 \simeq 2.4$ micrometers and $D_0 \simeq 0.6$ micrometers. A particle having a longer length and smaller diameter, like F_1 ($L_1 = 5$, $D_1 = 0.5$), would certainly be classified as a fiber, whereas a particle like N_2 ($L_2 = 1$, $D_2 = .2$) would certainly be classified as a nonfiber by reason of its short length. For this particle, $u_1 = 0.3$, $u_2 = 1.7$, $I_1/I_2 = 0.25$. Therefore, these regions of the plane have been labeled with the letters F for fiber and N for nonfiber. Because it is impractical to predict the shape of the intensity distribution as a function of angle outside the forward diffraction maximum, a particle like P_3 (L_3 = 30, D_3 = 3) cannot be analyzed with such assurance. Most large fibers like P_3 would produce a large ratio of scattered intensities, because the ratio of the scattered intensity in a particular direction to that in the forward direction is a generally decreasing function of the maximum dimension of the cross section of the particle in the scattering plane. However, depending upon the detector geometry, there may be some unexpected parts of the region P (for probable) where the intensity ratio is less than r. Of course, the intensity ratio is bound to approach unity as the aspect ratio L/D approaches one. Thus, the counting efficiency for fibers falls off in region P, from 100 percent at the boundary $D = D_0$, $L > L_0$, to zero for spherical particles like S_4, in a manner which seems hopeless to predict from theory.

The potential of the intensity-ratio technique for discriminating fibers of different dimensions at various scattering angles is illustrated in Fig. 27B which shows the rough boundaries of the regions N, F and P for scattering angles of 20, 40 and 90 degrees. This illustration ignores the very real problems of signal-to-noise ratio for small particles.

The absolute scattered intensity, as well as the variation with direction, is important to the operation of a fiber counter. Not only does it possibly (and in fact) determine the size of the smallest detectable fiber, but also it may give information about fiber sizes if it can be interpreted properly.

Rayleigh scattering theory predicts that, for particles whose sizes are much less than the wavelength λ of the incident radiation, the scattered intensity in all directions will be proportional to the square of the particle volume for any shape (46,47). This appears in conventional optical aerosol-particle counters as a proportionality of scattered intensity to the sixth power of the diameter d for very small spheres, $d \ll \lambda$. It is perhaps less often remarked that the Rayleigh-Gans-Debye (RGD) approximation predicts the same dependence upon the square of the particle volume for forward scattering at $\Theta = 0$, independent of particle shape, within its range of validity (small size, index near unity) (46, 47). Moreover, the proportionality of the intensity

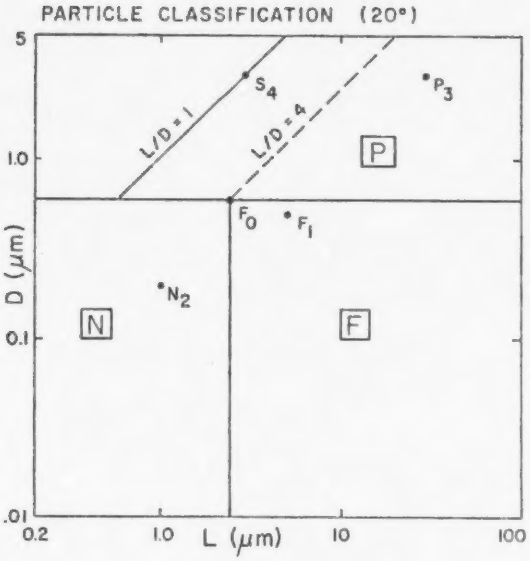

Figure 27 A

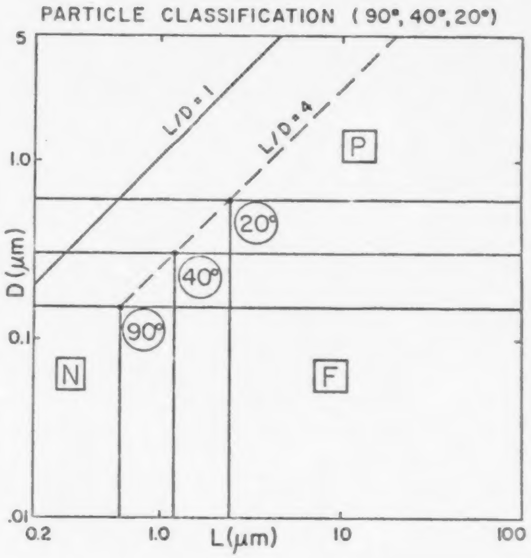

Figure 27 B

Fig. 27. The (L, D) or (length, diameter) plane for prolate spheroids or model fibers. Particles like F_1 in the region F will be classified as fibers by means of their light-scattering signatures, and those in the region N will be classified as nonfibers because they are too small. Particles in region P near the boundary of F will be classified as fibers, and those with high aspect ratio elsewhere in P will probably be counted as fibers, but the fiber-counting efficiency in P must necessarily fall off as one approaches spherical particles like S_4. Fig. 27 A - the boundaries of these regions for a scattering angle of 20 degrees, corresponding to the landmark fiber F_0: $(L_0, D_0) = (2.4\ \mu m, 0.6\ \mu m)$. Fig. 27 B - the classification boundaries for scattering angles of 20, 40 and 90 degrees, ignoring problems of signal-to-noise ratio.

to such a high power of the diameter for spheres does persist in exact calculations to larger diameters when the scattering angle is small (29).

Kerker (48) points out that the same proportionality to the square of the polarizable volume shows up in the scattered intensity from infinite dielectric cylinders of small diameter at perpendicular incidence. For infinite cylinders the appropriate criterion of smallness is, of course, the ratio of the short dimension, the diameter, to the wavelength. For fibers, modeled by prolate spheroids of large aspect ratio L/D in Fig. 24, the question arises as to whether both L and D must be small compared to the wavelength λ, in order for the forward-scattered intensity to be proportional to the volume, or whether

(61) $D << \lambda$

is sufficient for the validity of the RGD intensity at $\Theta = 0$. The remarkable agreement between the RGD calculations and the exact calculations in Appendix B, for the absolute intensity at zero scattering angle, supports the hypothesis that the condition of Eq. (61) on the diameter alone is adequate for prolate spheroids.

At least for the thinnest straight fibers, we shall assume that the scattered intensity in the brighter detector (essentially the same as at $\Theta = 0$) is proportional to the fiber volume V in the manner predicted by the RGD approximation (49)

(62) $$I_0 = k^4 V^2 (m-1)^2/4 \pi^2,$$

where k is the wave number of the incident light and m is the refractive index of the particle.

Neglecting the difference in refractive index between polystyrene latex spheres and asbestos fibers, we can compare the volumes of fibers (spheroids in Fig. 24),

$$V = \pi L D^2/6,$$

with small latex spheres of diameter d,

$$V' = \pi d^3/6,$$

by means of their forward-scattered intensities:

$$I_o/I'_o = (L\ D^2/d^3)^2. \tag{63}$$

This calibration was used to determine the sizes of the smallest fibers.

For any light-scattering, aerosol-particle counter there is a minimum scattered intensity for proper operation. The minimum intensity for reliably classifying particles as fibers or nonfibers in the UVM fiber counter corresponded to slightly less than the light scattered from a polystyrene latex sphere of diameter $d = 0.5$ μm (a little large for the assumed d^6 proportionality (29)). This limit was unfortunately imposed by background light in the scattering chamber. If the length of a fiber of the same volume is the minimum $L_0 = 2.4$ μm, then its diameter is less than $D = 0.2$ μm. For a longer fiber with, say, the standard minimum length of 5 μm, the diameter would be even less. These measurements were made with the UVM fiber counter set to inspect all particles for which the higher intensity exceeded that of a sphere of diameter $d = 0.4$ μm. Fig. 28 shows this particle threshold, and the corresponding, slightly higher, limit for reliable detection of small fibers superimposed on the (L, D) plane of Fig. 27A. The fiber F_1 in Fig. 28 would be counted, but F_5 ($L = 3$, $D = 0.1$) would be missed.

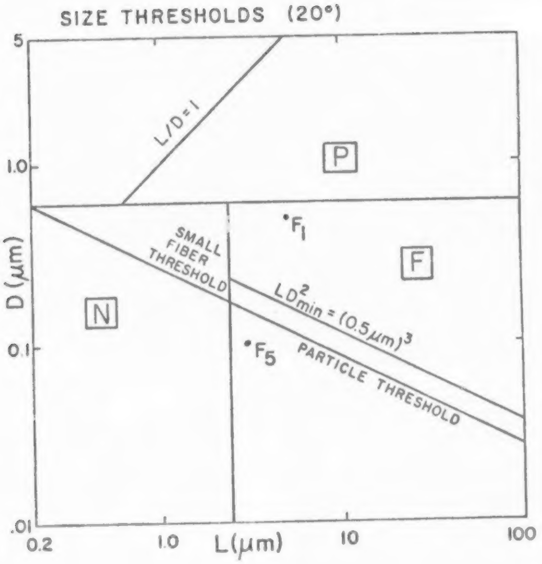

Fig 28. The (L, D) plane for prolate spheroids at a scattering angle of 20 degrees, with the present limits of sensitivity of the UVM fiber counter superimposed. The small fiber threshold represents the minimum pulse size for which the signal-to-noise ratio permits reliable fiber discrimination. The particle threshold is a typical instrument setting for the minimum size of a particle to be analyzed. Fiber F_1 would be counted, but fiber F_5 would be missed because it would not scatter enough light.

SECTION 6

TESTING

The time available for testing the UVM fiber counter during the project period was limited by the fact that the successful design was not evolved until the final few months of the project Efforts to reduce the stray light from the incandescent source had been unsuccessful, and it was finally replaced with a laser, as discussed in Section 4. The successful laser source permitted detection of the partial alignment of fibers in the sample airstream, and measurement of their complete alignment, within the final month or two. It is primarily these measurements that will be discussed here.

The test aerosols that were actually used with the fiber counter were generated by two methods. One was the nebulization of an aqueous suspension of polystyrene latex spheres (50), and the other was the mechanical agitation of a dry sample of UICC chrysotile (7). The original design of our aerosol generation and sampling system was capable of sustained production of aerosol samples over long periods of time, but its full capabilities were not used in our tests. Nevertheless, its large physical size, intended to average out variations in aerosol-generator output, turned out to be an important asset in that we could store an aerosol over a long period of time, thus permitting reproducible repetitive measurements while varying some parameter of the experiment.

The aerosol-storage chamber is a large, rectangular box made of clear acrylic plastic one cm thick. The front face is 106 cm long and 75 cm high, and the depth is 45 cm. The interior is divided into two compartments, the larger of which uses about 74 cm of the 106 cm length. An aerosol was introduced into the smaller compartment for premixing, and if necessary drying. It passed through several one cm holes into the larger chamber, which stored it with a half-life of one-half to one hour. Ports are included for the addition of clean air, addition of sample aerosols, rapid exhaust to assist in purging the chamber, connection of optical aerosol counters, collection of aerosol samples on an open-face filter, and a vacuum/pressure gauge. A small fan kept air circulating in the larger chamber. The front panel, sealed with a rubber gasket, is removable for the purpose of cleaning out the chamber. Because the inlet flow rate of an optical aerosol counter depends upon a pressure differential, it was necessary to monitor the pressure in the sample box continuously with a sensitive differential-pressure gauge (51), and to keep it within ± 0.05 inches-of-water-equivalent of ambient pressure by adjusting the airflows.

Clean air was provided to the box from the building air supply. After this air had passed through a conventional regulator, moisture trap and filter, it was conducted through a gas-drying column about 7 cm in diameter and 30 cm long. In the column the air passed upward through about 15 cm of indicating dessicant (52) to remove water vapor, followed by about 5 cm of activated charcoal to remove oil vapors. The dry air leaving the column was passed through a large membrane filter (53) and was controlled by one or more flowmeter-valve combinations before entering the chamber. The exhaust, when it was required, took place through another large membrane filter (53), and a pump, and was vented outdoors.

A normal cycle of operation began with enough flow through the system to fill it with an aerosol sample from the generator. Then, the exhaust was shut down, and clean air was admitted at a rate just adequate to replace the amount withdrawn by the various sampling devices: the fiber counter (5 cm^3/sec), a commercial optical aerosol-particle counter (54) (usually 50 cm^3/sec), and occasionally a sampling pump behind an open-face filter in the chamber. The aerosol lifetime when only the two particle counters were in operation is illustrated in Fig. 29. The half-life of an aerosol of one-micrometer particles is in the range of one-half to one hour.

The flow of clean air through the chamber could be increased to purge it of contaminants. Even so the limit on the background aerosol count in practice was the patience of the experimenter in flushing the chamber, not the cleanliness of the incoming air. The levels of cleanliness obtained were many orders of magnitude below the count rates produced by the test aerosols in every case.

During most of the tests, this large (350 liters) sample volume was filled with rather clean air (10-100 particles/cm^3 over 0.5 μm in diameter) because the fiber counter accumulated data rapidly at these

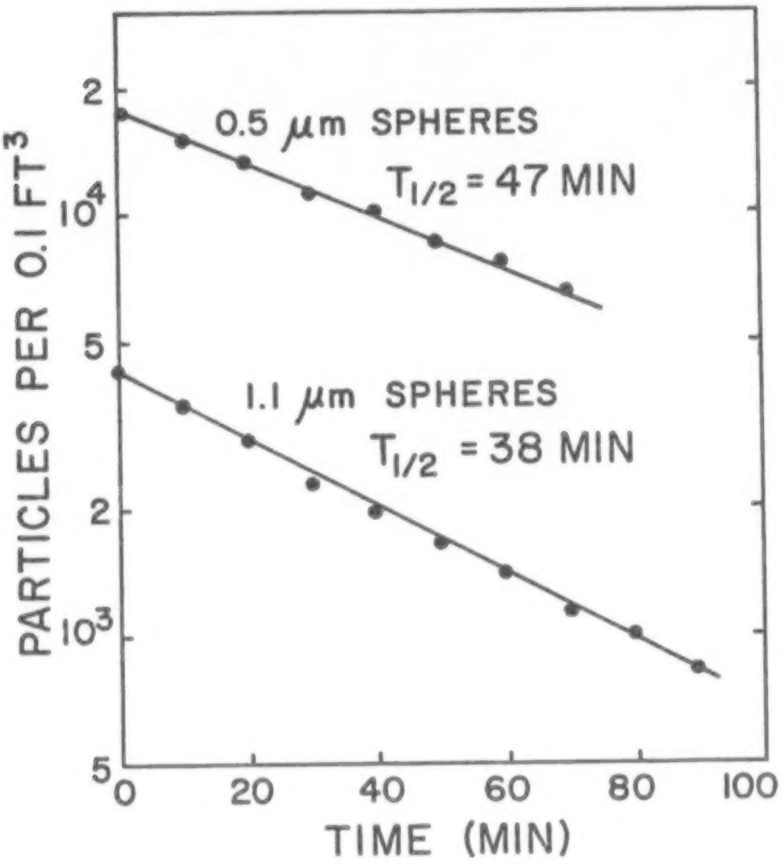

Fig. 29. The decay with time of the particle count in the 350 liter aerosol-storage chamber, for two different aerosols of polystyrene-latex spheres. The exhaust was about 50 cm/sec^3 for the aerosol-particle counters.

concentrations. This avoided any possibly confusing complications of coincidence effects, and reduced the danger of a large release into the laboratory in case of an unforeseen accident.

The polystyrene latex spheres (50) were made into test aerosols by first diluting the stock, 10 weight-percent, suspensions in distilled water. Filtration of the distilled water through a membrane filter just prior to mixing seemed to prolong the shelf life of the diluted suspension by removing microbiological contamination. Ultrasonic agitation was used to maintain a uniform suspension. Typically one drop of a 10 percent suspension of 1 μm spheres would be added to 100 ml of water, so as to produce a probability of about 0.01 for finding a sphere in a nebulizer droplet 6 μm in diameter. Under these conditions, the number of double particles was very small. Then, the diluted suspension was nebulized with either a Collison Nebulizer (55) or a simpler plastic nebulizer (56). The choice of nebulizer and operating conditions was not critical; use of the large box of clean, dry air for storage made generation of reproducible aerosols a relatively simple matter, compared to our earlier, continuous-flow methods.

Asbestos aerosols were produced from UICC samples (7) by a vibrating-bed, dry aerosol generator. The device was based upon the ideas of Spurny *et al*. (57), but our version was rather simple in construction. A modified, 25 mm membrane-filter holder was placed at the lower end of a plastic tube 11 cm long and 19 mm inside diameter. Clean air was pumped into the filter holder from below through a membrane filter, which supported a powder sample from which the aerosol was to be generated. The whole assembly was vibrated by a motor-driven eccentric arrangement, as shown in Fig. 30, in order to agitate the powder particles. The airflow was adjusted to be just adequate to levitate a particle of the largest acceptable aerodynamic diameter. At the top of the plastic tube, another crossflow of clean air carried the selected aerosol particles to the aerosol-storage chamber. This arrangement was used with talc as well as with asbestos.

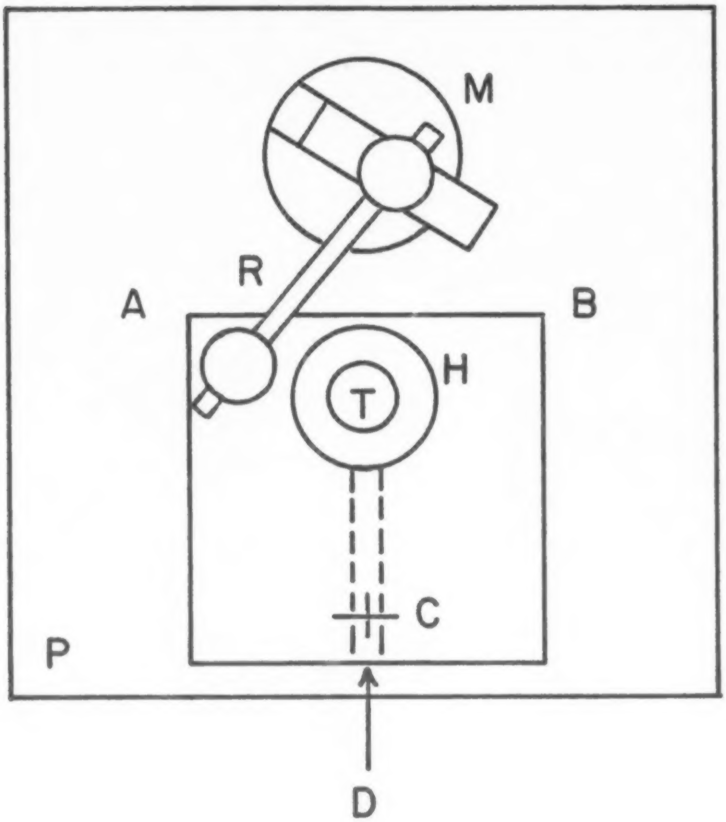

Fig. 30. A top view of the vibrating-bed, dry aerosol generator. Plastic block ABC pivots about point C on steel baseplate P, using wheels mounted at corners A and B. The block is caused to oscillate by an adjustable, motor-driven eccentric M, which is attached by rod R to a bearing at corner A. Clean air is admitted at D, to travel through a hole in the plastic block to filter-holder H. There it travels upward through a membrane filter supporting a powder sample and up tube T. Aerosol particles of sufficiently small aerodynamic diameter are agitated by the vibrating filter-holder and wafted up the tube T on the airflow. At the top of tube T, a crossflow carries them to the aerosol-storage chamber.

Normal operation of the vibrating-bed, dry aerosol generator employed an amplitude of about 2.5 mm peak-to-peak at a frequency of 25-30 Hz. The upward airflow was set to levitate particles whose aerodynamic diameters were less than about 15 micrometers. Samples of the aerosol were collected from the aerosol-storage box on open-faced membrane filters of 47 mm diameter and 0.2 micrometer pore size (20). The samples were examined in a scanning electron microscope (SEM) (58). No protocol was developed to assure statistically adequate sampling, and, therefore, the descriptions of the resulting SEM photographs must be regarded as subjective.

Two sets of measurements were made with samples of UICC Rhodesian chrysotile (7), and one with a sample of commercial powered talc, for which SEM photographs were recorded, in the last week of the project. In both cases it was clear that this aerosol generator selected and dispersed single, respirable particles from clumped, inhomogeneous powder samples. Whereas an earlier mechanical dust generator had tended to produce clumps of long fibers from UICC chrysotile samples, the vibrating-bed generator produced aerosol particles that looked like those in Fig. 31 in SEM photographs. With the talc, the larger lumps and aggregates (hundreds of micrometers across) remained behind in the generator, and only the smaller flakes (less than about 20 micrometers across) were transported into the aerosol-storage chamber. The talc sample was part of an unsuccessful attempt to see whether the fiber counter could distinguish flat plates (the dominant shapes among talc particles) from fibers. Unfortunately, both the SEM photographs and the fiber counter agreed that, especially among the respirable particles selected from the talc by this generator, there were a significant number of long, thin, flat "blades" that one could hardly avoid classifying as "fibers".

The "photon-counting" technique for measuring light intensities employs an actual count of the photoelectrons leaving the cathode of the photomultiplier tube, by amplifying each one sufficiently to register in an electronic counter. Use of this technique in an optical aerosol counter necessitated some initial tests of the technique itself. Counting the photoelectrons leaving the cathode of the photomultiplier removed the possibility of drift in analog-to-digital conversion of the photomulti-

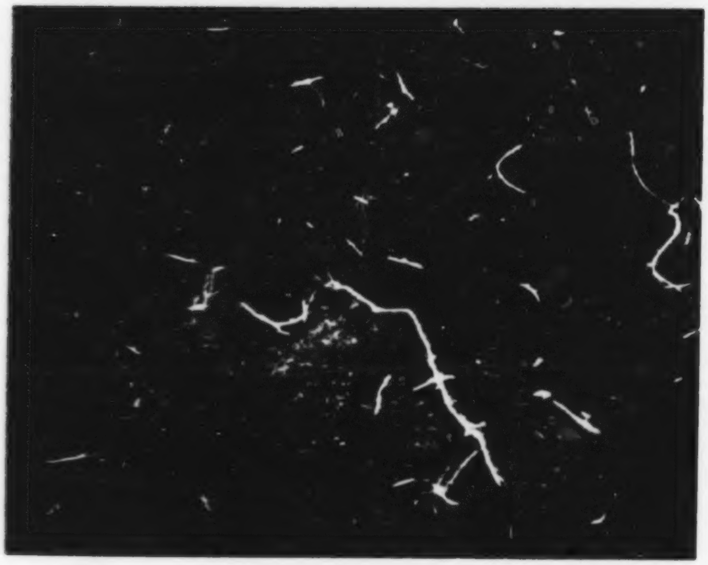

Fig. 31. SEM photograph at 1200X magnification of a Rhodesian chrysotile aerosol sample obtained on an open-faced membrane filter of 47 mm diameter and 0.2 μm pore size, recorded 6/29/78. The long dimension of the photograph corresponds to about 90 μm on the filter.

plier current at the input of the microcomputer. The ultimate limit on the measurements of low light intensities is then the dark count in the photomultipliers themselves, or if it is subtracted, then the fluctuations in this dark count. The low work functions of the red-sensitive photocathodes of the type 9798A photomultiplier tubes used with the laser led to the rather high dark-count rates of 1000-2000 per second at room temperatures, and this can be expected to rise at higher temperatures (32). However, the background light in the empty scattering chamber produced a count rate of about 80,000 counts per second, or about 8-9 photoelectron counts in a typical 110 microsecond sampling interval of the fiber counter. Because this light background was both larger and more stable than the true dark count, rather little attention was paid to the fluctuations of the photomultiplier dark current itself. Even with a steady background light, however, the emission of photoelectrons from the cathode is a statistical process, and the count in some 110 microsecond intervals can be expected to be considerably above the mean of 8-9. It was found in practice that this precluded setting the threshold, at which a particle was assumed to be present, much lower than about 25 photoelectrons. Such a large margin of safety might seem unnecessary until one realizes that the instrument samples the light intensity 10,000 times a second, and must find zero probability of a particle when none is present. This limit, it should be remarked, is a property of the quantum nature of light, and not the photon-counting technique alone.

The photon-counting technique reduces the dependence of the light-intensity calibration of the instrument upon the current gain of the photomultiplier tubes, as compared with a measurement of the anode current. During initial tests of the instrument with both the white-light source (type 9824B photomultiplier tubes) and the laser source (type 9798A photomultiplier tubes), it was found that the photon-counting system could be operated on a "plateau" of the curve of count-rate vs high-voltage, where a change of 100 volts in operating potential [representing a factor of perhaps 2 in photomultiplier gain (32)] produced a change in photoelectron count-rate of only about 10 percent. This occurred at a high-voltage of 1450 volts for the 9798A tubes used with the laser. Therefore, one can conclude that the photon-counting technique makes the intensity calibration relatively insensitive to any changes in photomultiplier gain which might reasonably be expected from high-voltage drift or temperature effects.

Unfortunately, however, the overall calibration factor of the fiber counter for scattered intensities cannot be said to be stable. Tests revealed that the principal problem is the alignment of the laser beam, and its cause is an inadequate mounting system for the laser.

Tests of the short-term particle-size resolution confirmed that the Gaussian shape of the distribution of light intensity across a laser beam, discussed in Section 4, necessitated a compromise. A too-narrow laser beam would concentrate the light where it was needed most, on the aerosol beam, but the edges of the aerosol beam would be much less brightly illuminated. Data recorded for the compromise setting used in the tests of the instrument are shown in Fig. 32. These data are for the smallest (volume) aerosol particles for which the counter was believed to discriminate fibers reliably. The clean-air background, due to scattered light in the chamber, was about one unit on the abscissa of Fig. 32. In order to register as a particle, the light intensity in at least one detector had to exceed the threshold of 25 photoelectrons marked at an abscissa of 3 units in the figure. One can see from these data that the efficiencies of the two light detectors are quite similar. These data were, in fact, recorded by the calibration program of the computer, which determined from the data that the ratio of intensities in counters A and B, I_A/I_B, should be corrected by a factor of 72/64, so as to give unity for spherical particles. This is the factor f of Section 4; the units of sixty-fourths are convenient for the MP-12 computer described in that section.

For spherical particles like the latex spheres used to obtain the data of Fig. 32, one should expect equal light intensities, not only on the average, but particle-by-particle in both detectors. Of course, the photoelectron counts, like those in many counting processes, have a Poisson distribution, and the standard deviation of the count for such a distribution is the square root of the mean, which for the data in Fig. 32 is about 9 photoelectrons, or 1 unit on the abscissa. The ratio of two such counts for one particle should be within 20 percent of unity most of the

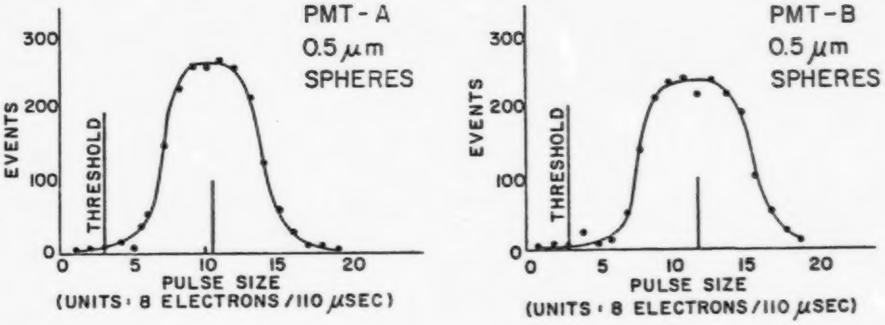

Fig. 32. Distribution of the peak light intensities scattered simultaneously into two photomultiplier tubes, A and B, from 0.5 μm diameter polystyrene latex spheres at a scattering angle of 20 degrees. The incident beam is about 2 mW of circularly polarized light of wavelength 633 nm at the sample volume. The units of intensity are "8 photoelectrons per sampling interval of 110 microseconds" because the sampling time of the instrument is normally 110 microseconds for this computer program, and bins 8 counts wide were convenient for sorting the pulses in this particular measurement. These data were recorded during the calibration run of 4:42 PM, 6/23/78.

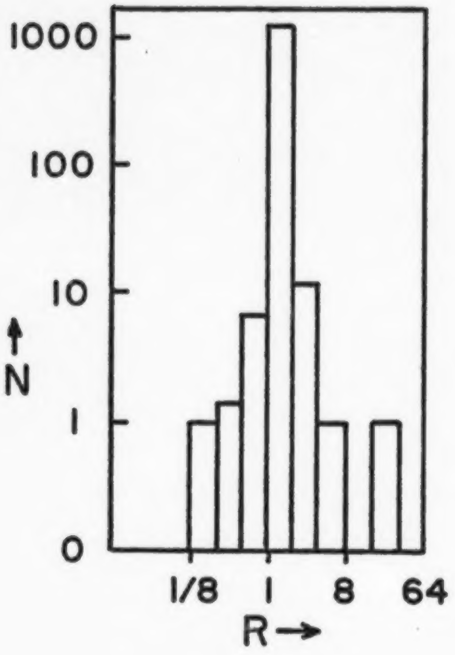

Fig. 33. The distribution of number of events N vs intensity ratio $R = I_A/I_B$, for the 0.5 μm latex spheres whose pulse-size distributions are shown in Fig. 32. The unusual log-log histogram was chosen to make visible the small wings of the distribution. The bar just to the right of R = 1 includes all events for which the product (64/<R>)R is equal to or greater than 64, but less than 128, where <R> is the average value of R from a previous run. The slight asymmetry around R = 1 results from the fact that the bar just to the right of center included the equality R = 1, and also the fact that the caule of <R> was incorrectly chosen to be 76/64, instead of the correct value of 72/64, based on a previous run where the high voltage on one photomultiplier was reduced by 50 volts. However, that does not explain the single event with R > 16, which would have been classed as a fiber by the fiber-counting program. That seems to be a unique event in the set of 15 runs, of several thousand spherical particles each, made on that day. It is probably the result of a dust particle drifting across the laser beam outside the sample volume, because the chamber had been opened to the room air only an hour earlier. Therefore, this represents in a real sense a "worse case" for spherical aerosols.

time. Fig. 33 shows the distribution of ratios of intensity for the same data run as Fig. 32, in a way that magnifies the small wings of the distribution, far from the center. Of 2022 total events recorded in 100 seconds, 2004 are within a factor of 2 of unity. The data of Fig. 33 are unusual in that they do show one event that would be classified as a fiber by the fiber-counting program, based on a threshold-ratio of intensities of 8. Since no similar count showed up in other, similar runs on the same day, this has tentatively been ascribed to a not-yet-flushed aerosol particle that crossed the laser beam outside the sample volume. The data of Fig. 33 represent a "worst case" from among the data for spherical particles.

A measurement of the relative velocities of the aerosol particles in the sample volume under different operating conditions was available directly from the calibration program in the microcomputer. The minimum scattered intensity could be set to some threshold value, usually 25 photoelectrons per 110 microsecond sampling interval, which defined a minimum particle. The number of successive intervals during which the intensity stayed above the threshold value gave a measure of the temporal width of the light pulse from one particle. The calibration program displayed a histogram of these widths. The measured width-above-threshold was a function of maximum scattered-light intensity, as well as particle velocity, so that the distribution of pulse widths is most useful for monodisperse aerosols. Some distributions recorded for 0.5 μm polystyrene latex spheres are shown in Fig. 34. For these particles the maximum light intensity is about three times the threshold value. The effects of a laser beam of nonuniform intensity, a finite threshold setting, and a radial distribution of flow velocities in the sample stream, make absolute interpretation of these widths difficult. However, the relative behavior of particle transit time is well correlated with inlet flow rate, derived from the readings of the vacuum gauge on the scattering chamber. Similar data recorded for various flow rates in the clean-air sheath showed less than a 20 percent effect for a doubling of the sheath-flow rate. Refer to Section 4 for details of the airflow in the region of the sample volume.

Alignment of fibers in the airflow alone was noticed almost immediately when the counter was first tested with a purely asbestos aerosol of Rhodesian chrysotile on June 26, 1978. Previously it had been found that

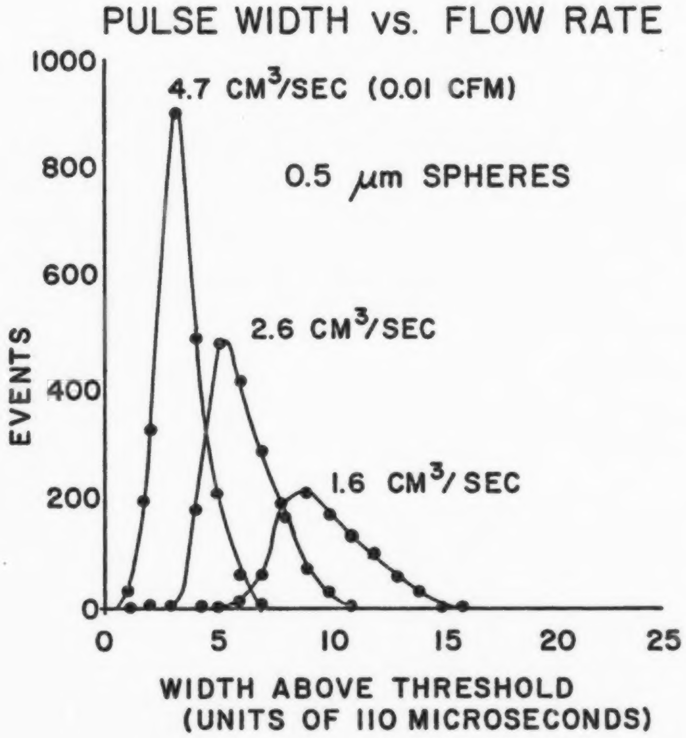

Fig. 34. Distributions of the temporal widths of the light pulses scattered at 20 degrees from a monodisperse aerosol of polystyrene latex spheres. These data were recorded on 6/23/78, for three flow rates in the sample inlet tube, as indicated by the vacuum in the scattering chamber. The highest flow rate corresponds to the design value for the fiber counter. Relative transit times in the laser beam are well correlated with flow rates. Absolute velocities could be extracte from such data only with great difficulty.

the average <R> of the intensity ratio $R = I_A/I_B$ was essentially the same whether measured with latex spheres or room air (if not adequately spherical, then presumably randomly oriented), and was quite stable over a period of days. The corresponding correction factor, f = 1/<R>, printed by the calibration program and intended to be applied as a factor to R so that spheres would give unity, had been stable at 1.06 ± 0.05 for many days of spherically symmetric calibration runs. Operation of the calibration program with an asbestos aerosol should have produced the same average correction factor if the fibers were randomly oriented, although individual fibers could be detected by large intensity ratios if they happened to be favorably oriented. The correction factor printed by the calibration program changed abruptly, however, to 1.28 as soon as the pure asbestos aerosol was introduced. This significant change in the average intensities occurred despite an orientation of the sample flow that greatly washed out the asymmetry in scattered light intensities from flow alignment. A recheck of the correction factor with room air confirmed that the original value of 1.06 was correct. A more detailed measurement of the distribution of intensity ratios for the asbestos revealed that indeed there was a marked tendency for one detector to receive a higher light intensity, and about 7 percent of the particles produced a high enough intensity-ratio to be classified as fibers.

The sample flow was immediately reoriented at 90 degrees to the laser beam and in the plane of the beam and one detector, so as to maximize the effect of any flow alignment on the asymmetry of the light scattered into the two detectors at a scattering angle of 20 degrees. The effect should be to favor the detector whose scattering plane was perpendicular to the plane of the laser and aerosol beams. The inlet and collector tubes were also insulated, so they could be used to produce an electric field of up to 3000 volts/cm in the sample region.

A large number of measurements were made of the alignment of chrysotile asbestos fibers in various electric fields. The aerosol source for these measurements was the aerosol-storage box, fed occasionally by the vibrating-bed aerosol generator. A simple, single parameter to measure fiber alignment was chosen to be the number of fibers (defined by an intensity ratio exceeding 8) detected in a fixed total count, essentially

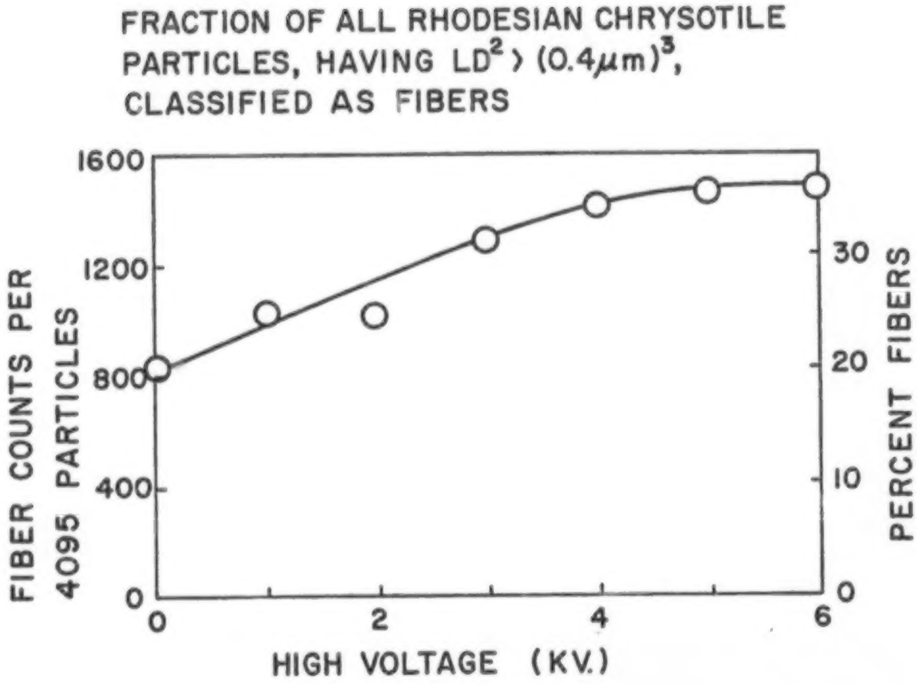

Fig. 35. The fractions of fibers detected in aerosol samples of Rhodesian chrysotile, for various values of applied high voltage, at a scattering angle of 20 degrees. The smallest particle counted in each sample of 4095 corresponds to about 30 percent of the light scattered in the same direction by a polystyrene latex shpere 0.5 μm in diameter. Saturation of the increase of fiber-counting efficiency with alignment appears to occur at an applied potential difference of 4000 volts, corresponding to an electric field of about 2000 volts/cm.

a fiber-counting efficiency. This quantity was remarkably constant for a given set of instrument settings, even from one charge to another of the aerosol-storage box, while the particle and, therefore, fiber count rate per unit time varied by a factor of at least five. The resulting data are plotted in Fig. 35. The abscissa in Fig. 35 is total potential difference applied across the gap between inlet and collector tubes, one-half of it between each one and ground. The electric field is roughly the abscissa divided by 2 cm. The ordinate in Fig. 35 is the number of fibers actually detected, per 4095 total particles above threshold (25 photoelectrons, about 30 percent of the intensity of a 0.5 μm latex sphere at the same angle). The number 4095 happens to be the largest single-precision integer in the MP-12 microcumputer. Particle concentrations were around 60 cm^{-3}. The sizes of the circles are meant to imply the reproducibility of particular points, although the scatter of some points (e.g., 2 kV) from the assumed smooth curve would indicate a little less stability.

In addition to the total fiber count, the fiber-counting program prints the distribution of intensity ratios for all particles classified as fibers. It makes no distinction as to which detector is brighter in classifying a fiber, because it was designed to operate with randomly oriented particles, but one can tell from the printout how many favored each detector. Therefore, one can count the number of fibers oriented normal to the airstream, an unfavored orientation, as a function of various parameters. With an airflow of 5 cm^3/sec, directed at 90 degrees to the laser beam, at a scattering angle of 20 degrees, and with 4095 particles of Rhodesian chrysotile passing through the sample volume, with no electric field, 824 fibers (intensity ratio exceeding 8) were counted in one of the runs. Of these, 36 were oriented so as to scatter more light into the detector in the plane of the laser and aerosol beams, while 788 favored the other detector. Some of the 4095 particles were undoubtedly fibers, oriented so that their scattered intensities happened to be symmetric in the two detectors. It can be seen, however, that there is already considerable alignment from the airflow alone. With a potential difference of 2 kV across the gap, 1042 fibers were found in 4095 particles in one measurement, and only 9 of these were oriented so as to favor light scattering into the detector in the plane of the laser beam and the aerosol beam. At a potential difference of 4 kV, 1440 fibers were found in one measurement of 4095 particles, only 1 of which was in the unfavored orientation. Data at 6 kV show no fibers in the unfavored orientation, and the change in fiber-counting efficiency between 4 and 6 kV appears from Fig. 35 to be quite small. An interpretation of these results is given in Section 5, but only qualitative and order-of-magnitude quantitative comparisons can be made because the particle shapes are nonideal and varied, and the velocity-gradient and electric fields are nonuniform and have not been calculated in detail.

Time did not permit the correction of a defect in the fiber counter that became obvious on studying the data from the Rhodesian chrysotile. Because of this defect, the roughly 35 percent maximum fiber-counting efficiency must be considered a lower limit on the fraction of aligned fibers. The data showed no intensities larger than 2000 photoelectrons in a sampling interval, but many particles near that maximum intensity. The maximum observed count rate of 2×10^7 photoelectrons/sec is in fact about the limit of the electronics. Fibers producing larger intensities in the brighter detector will saturate the electronics and produce too small an intensity ratio. Measurements at reduced laser intensities, to catch these largest fibers, were not made for lack of time in the project period.

Except for one unsuccessful attempt to produce aerosols of flat plates from talc, there was too little time left in the project period to clean the aerosol chamber and study other asbestos aerosols and nonasbestos aerosols properly. A few spot checks were made, however, with the sample inlet open to room air. These can be summarized briefly. The "fiber count" in the laboratory air hovered at about 0.02 cm^{-3}, despite the fact that readings with truly clean air or latex spheres were considerably less. No significant increase from this value was obtained from various clouds of talcum powder, chalk dust, or smoke wafted before the inlet. However, a piece of asbestos-cloth heating tape, "bumped" in front of the inlet, produced a very high fiber count. Also, it appeared that calcium sulfate crystals from the drying agent could produce a fiber count when "dusted" in front of the fiber counter. It was noted that, although, cigarette smoke did not produce any fiber counts, it could paralyze the instrument by essentially filling the sample inlet stream with a continuous haze that raised the background count, between large particles, above threshold.

REFERENCES AND FOOTNOTES

1. Lilienfeld, P. and P. B. Elterman. Development of a Prototype Fibrous Aerosol Monitor. Am. Ind. Hyg. Assoc. J., 40:270-282, 1979. See also, P. Lilienfeld and P. B. Elterman. Development and Fabrication of a Prototype Fibrous Aerosol Monitor (FAM). DHEW (NIOSH) Pub. No. 78-125, Public Health Service, Center for Disease Control, National Institute for Occupational Safety and Health, Cincinnati, Ohio, 1978.
2. Detenbeck, R. W. and E. P. Mosca. Determination of Aerosol Shape Distribution by Light Scattering. Invited paper presented at ACS Symposium on Surface and Colloid Chemistry in Air Pollution Control, Chicago, 1973.
3. Occupational Exposure to Fibrous Glass. Proceedings of a Symposium, College Park, MD., 1974. DHEW (NIOSH) Pub. No. 76-151, Public Health Service, Center for Disease Control, National Institute for Occupational Safety and Health, Cincinnati, Ohic, 1976.
4. Criteria for a Recommended Standards---Occupational Exposure to Fibrous Glass. DHEW (NIOSH) Pub. No. 77-152, Public Health Service Center for Disease Control, National Institute for Occupational Safety and Health, Cincinnati, Ohio, 1977.
5. Federal Register, Rules and Regulations, Section 1910 - Occupational Safety and Health Standards. Standard for Exposure to Asbestos Dust. Sec. 1910.93, added in Vol. 36, December 7, 1971, p. 23207, made permanent in Vol. 37, June 7, 1972, p. 11318, Redesignated Sec. 1910.1001 in Vol. 40, May 28, 1975, p. 23072.
6. Edwards, G. H. and J. R. Lynch. The Method Used by the U. S. Public Health Service for Enumeration of Asbestos Dust on Membrane Filters. Ann. Occup. Hyg. 11:1-6, 1968.
7. Timbrell, V. Characteristics of the International Union against Cancer Standard Reference Samples of Asbestos. In: Pneumoconiosis: Proceedings of the International Conference, Johannesburg, April, 1969. Oxford University Press, 1970, pp. 28-36.

8. Timbrell, V. Aerodynamic Considerations and Other Aspects of Glass Fiber. In: Occupational Exposure to Fibrous Glass. Proceedings of a Symposium, College Park, MD., 1974. DHEW (NIOSH) Pub. No. 76-151, Public Health Service, Center for Disease Control, National Institute for Occupational Safety and Health, Cincinnati, Ohio, 1976.
9. Spurny, K. R., W. Stober, H. Opiela, and G. Weiss. Size-Selective Preparation of Inorganic Fibers for Biological Experiments. Am. Ind. Hyg. Assoc. J., 40:20-38, 1979.
10. Fischbein, A., A. N. Rohl, A. M. Langer and I. J. Selikoff. Drywall Construction and Asbestos Exposure. Am. Ind. Hyg. Assoc. J., 40:402-407, 1979.
11. Yeh, C. On the Scattering from Arbitrarily Shaped Inhomogeneous Particles-Exact Solution. In: Light Scattering by Irregularly Shaped Particles, Proceedings of the Workshop, SUNYA, Albany, New York, June 5-7, 1979. (LSISP). To be published. See also Reference 16.
12. Kerker, M. Scattering by Particles with Internal Structure. In: LSISP (See Reference 11).
13. Kattawar, G. Calculation of the Phase Matrix for Electromagnetic Scattering from Two Interacting Spherical Particles. In: LSISP (See Reference 11).
14. Wang, R. Extinction Signatures of Nonspherical/Nonisotropic Particles, In LSISP (See Reference 11).
15. Zerull, R. Scattering by Particles of Nonspherical Shape. In: LSISP (See Reference 11).
16. Yeh, C., K. Ha, S. Dong, and W. Brown. Single-Mode Optical Waveguides. Appl. Optics, 18: 1490-1504, 1979.
17. Model 0211 vacuum/pressure pump. Gast Mfg. Corporation, Benton Harbor, Michigan.
18. Model FM044-40G flowmeter. Aalborg Instruments and Controls, Inc., Monsey, New York.

19. Model 125-AV inclined manometer. Dwyer Instruments, Inc. Michigan City, Indiana.

20. Polycarbonate membrane filter. Nuclepore Corporation, Pleasanton, California.

21. Pao, R. Fluid Mechanics. John Wiley, New York, 1961, pp. 183-201.

22. Kestin, J. Viscosity of Gases. In: American Institute of Physics Handbook, Gray, D. E, Ed., McGraw-Hill, New York, 1957, p. 2-207.

23. Lindsay, R. Density of Gases at Standard Temperature and Pressure. In: American Institute of Physics Handbook, Gray, D. E., Ed. McGraw-Hill, New York, 1957, p. 2-198.

24. Barr, G. A Monograph of Viscometry. Oxford University Press, London, 1931.

25. Schlichting, H. Laminare Strahlausbreitung. Zeitschr. f. angew. Math. u. Mech., 13:260-263, 1933.

26. Andrade, E. and L. Tsien. The Velocity Distribution in a Liquid-into-Liquid Jet. Proc. Phys. Soc. London, 49:381-391, 1937.

27. Heyder, J., C. Roth, and W. Stahlhofen. A Laser Spectrometer for Size Analysis of Small Airborne Particles. Aerosol Science, 2:341-352, 1971.

28. Husar, R. Recent Developments in IN SITU Size Spectrum Measurements of Submicron Aerosols. In: Instrumentation for Measuring Air Quality, ASTM STP 555. American Society for Testing Materials, 1974, pp. 157-192, esp. pp. 164-165.

29. Gebhart, J., J. Bol, W. Heinze, and W. Letschert. A Particle-Size Spectrometer for Aerosols Utilizing Low-Angle Scattering of the Particles in a Laser Beam. Staub-Reinhalt Luft, 30 #6:5-14, 1970.

30. Model FM092-04G flowmeter. Aalborg Instruments and Controls, Inc., Monsey, New York.

31. Type FCR tungsten-halogen lamp, described in: Sylvania Photolamps, Publ. R-117. GTE/Sylvania Lighting Center, Danvers, Mass., 1974. See also High Brightness Quartz Halogen Filament Source 100 Watts-3000 K in: Catalog. Oriel Corporation of America, Stanford, CT., 1975, p. 59.

32. EMI Photomultipliers, Publ. P001/D75. EMI/Gencom Division, Plainview, New York, p. 5, 1975.

33. Nicodemus, F. Radiometry. In: Applied Optics and Optical Engineering, Vol. 4. Academic Press, New York, 1967, Ch. 8.

34. Reynolds, M. Radiometry. In: American Institute of Physics Handbook, Gray, D., Ed. McGraw-Hill, New York, 1957, p. 6-73.

35. Model 3024H-P, mW polarized He-Ne laser. Hughes Aircraft Company, Industrial Products Division (Laser Products), Carsbad, CA.

36. Sinclair, D. and W. Bell. Gas Laser Technology. Holt, Rinehart and Winston, New York, 1969, Ch. 4.

37. Anczurowski, E. and S. G. Mason. The Kinetics of Flowing Dispersions III. Equilibrium Orientations of Rods and Discs (Experimental). J. Colloid Int. Sci., 23:533-546, 1967.

38. Harris, Robert L. A Model for Deposition of Microscopic Fibers in the Human Respiratory System. Ph.D. thesis, School of Public Health, University of North Carolina at Chapel Hill, 1972.

39. Jeffery, G. B. The Motion of Ellipsoidal Particles Immersed in a Viscous Fluid. Proc. Roy. Soc. London, A102 #A715:161-179, November 1922.

40. Becker, R. Electromagnetic Fields and Interactions, English translation by F. Sauter, Vol. 1. Blaisdell, New York, 1964, pp. 102-107, and 123-125.

41. Tanford, C. Physical Chemistry of Macromolecules. Wiley, New York, 1961, p. 436.

42. Scheraga, H. A., J. T. Edsall, and J. O. Gadd. Double Refraction of Flow: Numerical Evauation of Extinction Angle and Birefringence as a Function of Velocity Gradient. J. Chem. Phys., 19: 1101-1103, 1951.

43. von Hippel, A. R. Dielectric Materials and Applications, MIT Technology Press, Cambridge, Mass., and John Wiley, N.Y., p. 313, 1954. Values given for the dielectric constant K range from 5.75 to 8.75 for commercial asbestos insulators. See also Keller, G. V. Electrical Properties of Rocks and Minerals, in Handbook of Physical Constants, S. P. Clark, Ed., Geol. Soc. of Am. Memior #97, N. Y., pp. 566-567, 1966, where dielectric constants of common silicates range around 7.

44. Hodkinson, J. R. Particle Sizing by Means of the Forward Scattering Lobe. Appl. Optics 5:839-843, 1966.

45. Gravatt, C. G., Jr. Real Time Measurements of the Size Distribution of Particles Matter by a Light Scattering Method. J. Air. Poll. Control Assoc., 23:1035, 1973.

46. Kerker, M. The Scattering of Light and Other Electromagnetic Radiation Academic Press, New York, 1969.

47. van de Hulst, H. C. Light Scattering by Small Particles. John Wiley, New York, 1957.

48. See Reference 46, pp. 266-269.

49. See Reference 46, pp. 414-429. The choice among several m dependences discussed there seems to be irrelevant to particles of nonideal shape, where discrepancies of 20-50% must be expected.

50. Polystyrene latex spheres, used as spherical calibration particles, were obtained in aqueous suspensions from Dow Diagnostics, Dow Chemical Co., P. O. Box 68511, Indianapolis, Indiana 46268. Their diameters were specified as 1.101 ± .0055 µm, 0.500 ± .0027 µm, and 0.234 ± .0026 µm and their refractive index as 1.5905 by the manufacturer.

51. Magnehelic gauge, model 2302. Dwyer Instruments Inc., Michigan City, Indiana.

52. Drierite, indicating anhydrous $CaSO_4$. W. A. Hammond Drierite Company, Xenia, Ohio.

53. Membrane filters, MF-Millipore, catalog no. AAWP-293-00 (0.8 μm pore size and 293 mm diameter) on inlet and catalog no. AAWP-142-00 (0.8 μm pore size and 142 mm diameter) on outlet. Millipore Corp. Bedford, Mass. 01730.

54. Optical Particle Counter. Model 245, sensitivity 0.5 μm, flow 0.1/1.0 CFM. Royco Instruments Inc., 141 Jefferson Drive, Menlo Park, Cal. 94025.

55. BGI Incorporation, 58 Guinan St., Waltham, Mass. 02154. See May, K. R. The Collision Nebulizer: Description, Performance and Application. J. of Aerosol Science, 4:235, 1973.

56. Nebulizer, stock #6515-823-8053, DeVilbiss Co., Somerset, Pa.

57. Spurny, K. R., C. Boose, D. Hochrainer and F. J. Monig. A Note on the Dispersing of Fibrous Powders. Ann Occup. Hyg., 19:85-87, 1976.

58. Two different scanning electron microscopes were used at different times. One was a model JSM 35, made by JOELCO, Tokyo, Japan. The other was a Cambridge Mark II, Cambridge-Imanco, Monsey, New York. The photographs in the text are from the Cambridge Mark II.

59. Olver, F. W. J. Bessel Functions of Integer Order. Ch. 9 of Abramowitz, M. and I. A. Stegun, eds. Handbook of Mathematical Functions. U. S. National Bureau of Standards, Applied Mathematics Series, 55. U. S. Government Printing Office, Washington, D. C., 1964 (tenth printing, Dec., 1972, with corrections).

60. Fowles, G. Introduction to Modern Optics. Holt, Rinehart and Winston, New York, 1975. p. 119.

61. Boron, S. and B. Waldie. Particle Sizing by Forward Lobe Scattered Intensity-Ratio Technique: Errors Introduced by Applying Diffraction Theory in the Mie Regime. Appl. Optics, 17: 1644-1648, 1978.

62. Asano, S. and G. Yamamanoto. Light Scattering by a Shperoidal Particle. Appl. Optics, 14:29-49, 1975.

63. Barber, P. and C. Yeh. Scattering of Electromagnetic Waves by Arbitrarily Shaped Dielectric Bodies. Appl. Optics 14:2864-2872, 1975.

64. Barber, P. and D. Wang. Rayleigh-Gans-Debye Applicability to Scattering by Nonspherical Particles. Appl. Optics 17:797-803, 1978.

APPENDIX A

THE IMITATION OF A FIBER BY TWO SPHERES

APPENDIX A

THE IMITATION OF A FIBER BY TWO SPHERES

Two small spherical particles are in a sampling volume of about 1mm^3, illuminated by a beam of monochromatic laser light. Two phototubes view the sampling volume from different orientations, chosen so that a single spherical particle would scatter equal intensities into the two detectors, but a fiber would not. As shown in Fig. 4, the two detectors have the same scattering angle θ, but different azimuthal angles ϕ.

The coherent light from two spherical scatterers interferes, and one detector may be at a point of constructive interference while the other is at a point of destructive interference. The maximum distance between two particles for which this effect is significant, however, is limited by the finite aperture of one detector. When the spacing between adjacent interference maxima is much smaller than the detector aperture, as it must be for a sufficiently large interparticle spacing, then the maxima and minima of the interference pattern will be averaged out.

The incident beam is described by a plane wave of unit amplitude which we can treat in scaler scattering theory:

$$E_i = e^{i\vec{k}_i \cdot \vec{r}} \tag{A1}$$

Scatterer A, at the origin, produces a scattered amplitude given in the farfield region by

$$E_{oA} = \frac{e^{ik_o r}}{r} f(\theta) \tag{A2}$$

The scattered amplitude from an identical scatterer B, displaced by $\vec{R}$ from A, is

$$E_{oB} = e^{i(\vec{k}_i - \vec{k}_o)\cdot\vec{R}} \frac{e^{ik_o r}}{r} f(\theta) \tag{A3}$$

The intensity I at a detector is proportional to the square of the sum of the amplitudes, (A4) $$I = \frac{2|f(\theta)|^2}{r^2} \left[1 + \cos(\vec{\kappa} \cdot \vec{R})\right] ,$$

with

(A5) $$\vec{\kappa} = \vec{k}_0 - \vec{k}_i \quad .$$

For two point detectors, in directions $\vec{k}_{01}$ and $\vec{k}_{02}$, an infinite ratio of intensities is possible. When the interference pattern described by Eq. (A4) is averaged over a finite detector size, encompassing a range of $\vec{\kappa}$, the amplitude of the modulation of the intensity by the cosine term is reduced, more so for larger values of R. We want to estimate R for a ratio of maximum to minimum intensity of, say, two to one for a particular detector. Eventually, we want to estimate an "excluded volume", from which a second particle must be excluded in order to avoid a false fiber count. This, in turn, will permit an estimate of a maximum permissible particle concentration, above which an unacceptable number of false fiber counts might occur.

Two typical detector geometries are shown in Fig. (A1). In one case the light from the scattering volume is collected by a lens of diameter 2 cm, at a distance of 8 cm; in the other case a longer-focal-length lens of the same diameter is used at a distance of 4 cm.

The analysis of the following paragraphs assumes interference of the amplitudes reaching each point of the detector-lens aperture from particles A and B. Were the photomultiplier cathode to be placed directly at this aperture, this would be exactly the case. On the other hand, one might imagine perfect, nonoverlapping, point images of particles A and B produced by the lens at different places on the photocathode, in which case interference between A and B could not occur. Imperfect optics, and internal reflections in the glass envelope of the phototube, make resolution of the images unlikely for particle separations much less than, say, 0.1 mm. Therefore, the following analysis is meant to correspond to a worst-case focus, in which the images of the two particles have complete overlap on the phototube's cathode. However, an analysis of an ideal optical system, whose resolution is limited only by diffraction at the lens aperture, still gives essentially the same result, as indicated in the last paragraph of this section.

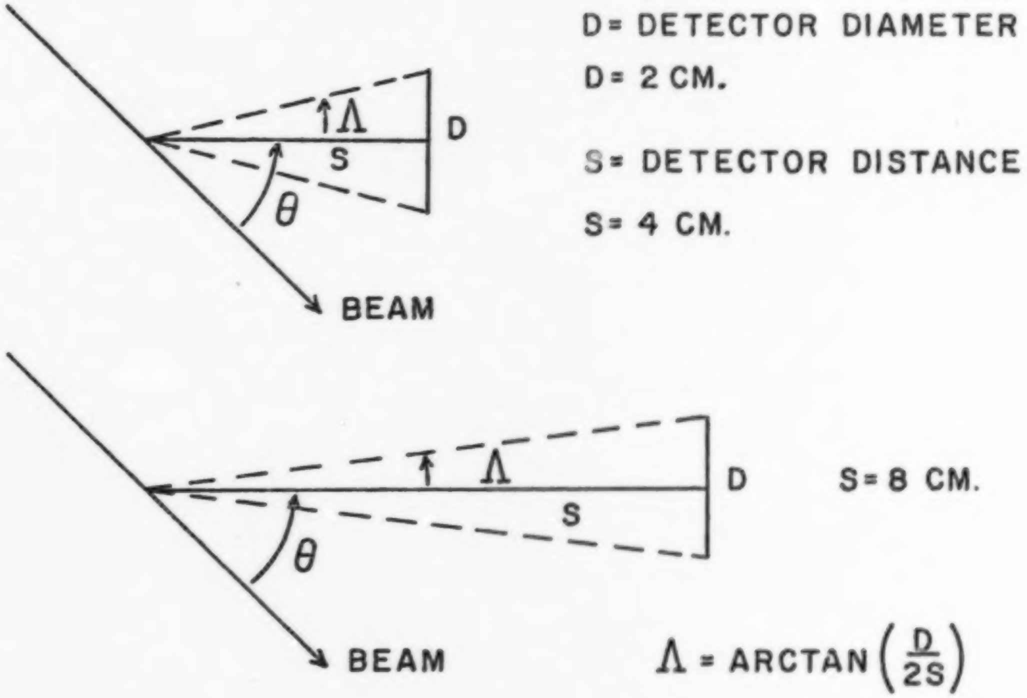

Fig. A1. Two light-collection geometries used in the fiber counter at different times. In the more common case the light was collected by a lens of 2 cm diameter at a distance of 8 cm from the sample volume. In the other case the distance was 4 cm.

For the analysis choose a coordinate system whose z axis lies parallel to the central ray of detector number one. The y-z plane is chosen to contain the incident wave vector $\vec{k}_i$, as well as the central scattered wave vector $\vec{k}_{01}$. This geometry is shown in Fig. A2. In terms of the angles defined in Fig. A2, the relevant wave vectors can be written in (x, y, z) component form

(A6) $$\text{incident:}\quad \vec{k}_i = k_o\,(0, -\sin\theta, \cos\theta)$$

$$\text{central, scattered:}\quad \vec{k}_{01} = k_o(0, 0, 1)$$

$$\text{difference:}\quad \vec{\kappa}_1 = \vec{k}_{01} - \vec{k}_i = k_o(0, \sin\theta, 1-\cos\theta)\,.$$

The first two wave vectors have been separated into magnitudes and unit vectors, but the most convenient form for the third one is not in such a form; the magnitude of $\vec{\kappa}_1$ is

(A7) $$\kappa_1 = 2k_o \sin\frac{\theta}{2}$$

The most general wave vector for scattering into an off-axis point on detector number one is

(A8) $$\vec{k}_o = k_o(\sin\lambda\,\cos\mu,\ \sin\lambda\,\sin\mu,\ \cos\lambda).$$

From Eq. (A8) and Fig. A2 it can be seen that λ is the angle between $\vec{k}_{01}$ and $\vec{k}_o$, and μ is the azimuthal angle, between the x axis and the projection of $\vec{k}_o$ onto x-y plane. The angle λ is generally restricted to be less than some maximum angle Λ related to the size of the detector and its distance from the scatterer. See Figs. A1 and A2. For the dimensions given in Fig. A1, it is adequate to approximate,

(A9) $$\sin\lambda \simeq \lambda,\ \cos\lambda \simeq 1.$$

With this approximation, Eq. (A8) can be written

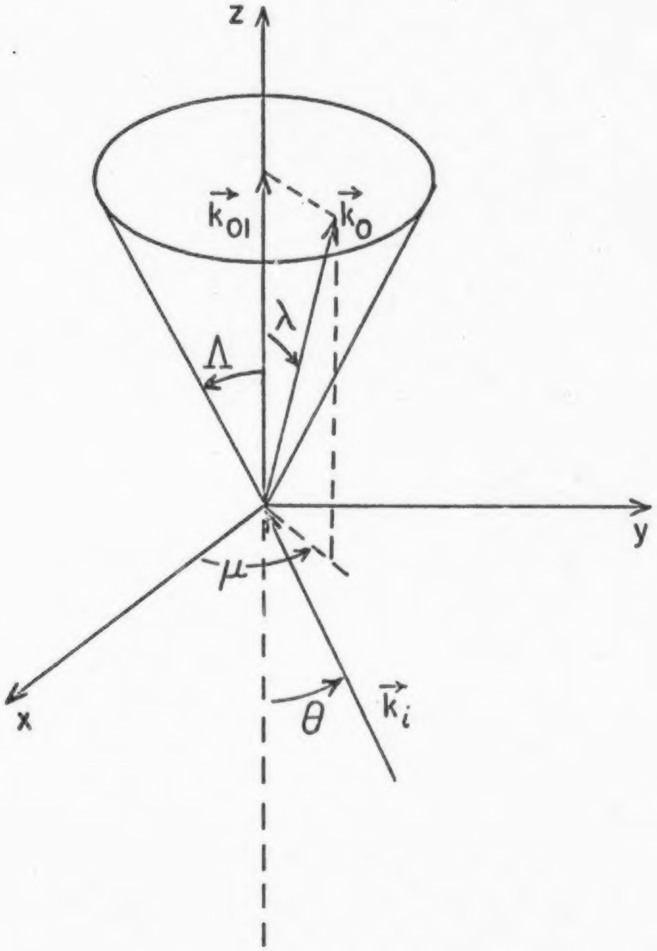

Fig. A2. Geometry for light collection by detector number one. The z axis is the detector's axis of circular symmetry. The y-z plane contains both the incident wave vector k_i and the central scattered wave vector k_{01}. The wave vector k_0 is directed toward a general point of the detector aperture, which includes angles $\lambda < \Lambda$.

(A10) $$\vec{k}_o = k_o\,(\lambda \cos \mu,\ \lambda \sin \mu,\ 1).$$

The change in wave number, for this general point on the detector, is

(A11) $$\vec{\kappa} = \vec{k}_o - \vec{k}_i = k_o\,(\lambda \cos \mu,\ \lambda \sin \mu + \sin \theta,\ 1 - \cos \theta).$$

Eq. (A4) can now be written, for a finite detector number one, as

(A12) $$I_1 = \frac{2|f(\theta)|^2}{r_1^{\,2}}\,(G + H)\ ,$$

in which we have neglected the small fractional variations of $| f(\theta) |^2$ and r^2 over the face of the detector, and defined

(A13) $$G = \int_0^{\Lambda} \lambda\, d\lambda \int_0^{2\pi} d\mu = \pi\Lambda^2$$

and

(A14) $$H = \int_0^{\Lambda} \lambda\, d\lambda \int_0^{2\pi} d\mu \cos(\vec{\kappa} \cdot \vec{R})\ .$$

If we let the angle between the z axis and $\vec{R}$ be α, and the azimuthal angle of $\vec{R}$ be β, relative to the coordinate system of Fig. A2, we can combine Eqs. (A11) and (A14) preparatory to carrying out the integration:

(A15) $$H = \int_0^{\Lambda} \lambda\, d\lambda \int_0^{2\pi} d\mu \cos\{\,(k_oR)\ (\lambda \sin \alpha \cos \beta \cos \mu + \lambda \sin \alpha \sin \beta \sin \mu + \sin \alpha \sin \beta \sin \theta + \cos \alpha - \cos \alpha \cos \theta)\,\}\ .$$

Eq. (A15) has the form,

(A16) $$H = \int_0^{\Lambda} \lambda\, d\lambda \int_0^{2\pi} d\mu \cos\{A\, \lambda \cos(\mu - \beta) + B\}\ ,$$

In which A and B are parameters independent of μ and λ ,

(A17) $$A = k_oR \sin \alpha = k_oR_1\ ,$$

and

$$(A18)\qquad B = k_oR\ (\sin\alpha\sin\beta\sin\theta + \cos\alpha - \cos\alpha\cos\ \theta) = \vec{\kappa}_1 \cdot \vec{R}.$$

The interference pattern appears in Eq. (A16) as the dependence of H upon the quantity B, but the effect is washed out by integrating over the oscillating term A. The component of the interparticle separation $\vec{R}$, relevant to washing out the interference pattern, is seen to be

(A19) R_s = length of component of $\vec{R}$ perpendicular to $\vec{\kappa}_{01}$.

An integral representation of the zero-order Bessel function is (59)

$$(A20)\qquad J_o(z) = \frac{1}{\pi}\int_0^{\pi} \cos(z\cos\theta)\ d\theta = \frac{1}{2\pi}\int_0^{2\pi} \cos\{z\cos(\mu - \beta)\}\ d\mu\ ,$$

whereas

$$(A21)\qquad \int_0^{2\pi} \sin\{z\cos(\mu - \beta)\}\ d\mu = 0.$$

Therefore,

$$(A22)\qquad H = 2\pi\cos B\int_0^{\Lambda} \lambda\, J_o(A\lambda)\ d\lambda.$$

Define new variables,

$$(A23)\qquad \gamma = A\ \lambda,\ \Gamma = A\ \Lambda,$$

and write

$$(A24)\qquad H = \frac{2\pi}{A^2}\{\cos B\}\int_0^{\Gamma} J_o(\gamma)\ d\gamma\ .$$

The integral in Eq. (A24) can be evaluated by using a relation for the deriatives of Bessel functions (59),

(A25) $$\frac{d}{dz} \{z\, J_1(z)\} = z\, J_0(z).$$

The result for the integral of interest is, therefore,

(A26) $$H = \frac{2\pi}{A^2} \{\cos B\}\Gamma \;\; J_1(\Gamma),$$

whereas, from Eqs. (A13) and (A23),

(A27) $$G = \frac{\pi\, \Gamma^2}{A^2} .$$

The ratio of the extreme intensities in the averaged interference pattern will be

(A28) $$Q = \frac{1 + 2\, J_1(\Gamma)/\Gamma}{1 - 2\, J_1(\Gamma)/\Gamma} \quad ,$$

which is a function of the single parameter

(A29) $$\Gamma = A\, \Lambda = k_o\, R_s \arctan \frac{D}{2S} \simeq \frac{k_o R_s D}{2S} \quad ,$$

now expressed in terms of geometry of Fig. A1. A table of $Q(\Gamma)$ is given as Table A1. For small z we can write (59)

(A30) $$J_1(z) = (\tfrac{1}{2}\, z)\;\; (1 - z^2/8 + \ldots) \quad ,$$

and hence, for small Γ, Q goes to infinity as

(A31) $$\lim_{\Gamma \to 0} Q(\Gamma) = 16/\Gamma^2.$$

Clearly, from Table A1, Q oscillates within ten percent of unity for values of Γ exceeding ten. Therefore, to avoid a false count we can conservatively require

(A32) $$R_s > \frac{20\ S}{k_0\ D}\ .$$

In our instrument k_0 is 10 micron $^{-1}$, D is 2 cm, and in the worst case S is 8 cm. Therefore, we require

(A33) $$R_s > 8 \text{ microns.}$$

The "excluded volume" for one detector is a cylinder of 8 microns radius, surrounding the central axis of the detector, and as long as the width of the sampling volume. If this width is about 1mm, the excluded volume is

(A34) $$V = \pi R_s^2 \cdot 1 = 2 \times 10^{-7} \text{ cm}^3$$

If the dust concentration is n cm^{-3}, the chance that a particle be accompanied by a second in the excluded volume is n V. The false fiber count due to this type of coincidence will then not exceed

(A35) $$N = n^2 V = (2 \times 10^{-7})\ n^2 \text{ cm}^{-3}$$

The instrument surely cannot count more than $n = 200 \text{ cm}^{-3}$, without very high coincidence losses. Even this extremely high n would produce a false fiber count not exceeding

(A36) $$N = 0.008 \text{ cm}^{-3}$$

Eq. (A28) shows that the condition of Eq. (A32) upon R_s amounts to requiring that

(A37) $$2\ J_1(\Gamma)\ /\ \Gamma \ll 1.$$

If we analyze the problem differently, assuming that a perfect entrance lens makes images of the two particles on the cathode of the phototube, we obtain the same condition as Eq. (A37), for negligible interference of the two scattered amplitudes. The diffraction of light by the lens of diameter D will produce for each particle's image, not a spot, but a diffraction pattern in which the amplitude falls off away from the center as (60)

$$E = 2E_0 \, J_1(\Gamma)/\Gamma \, . \tag{A38}$$

In this equation E_0 is the amplitude at the center of the pattern ($\Gamma = 0$) and Γ is given by the approximation of Eq. (A29), where R_s is the distance away from the center measured in the object plane. If the images of the particles overlap, there will be interference effects in the intensity. This will be negligible if the amplitude from one particle is small at the location of the other image. According to Eq. (A38), this condition exists if Eq. (A37) holds. The similarity of the results of the two different methods of analysis is guaranteed by the conservation of energy, because the first method, which yields quantitative results, calculates the total energy flux into the lens.

TABLE A1

Ratios of Extreme Intensities, $Q(\Gamma)$ *

Γ	$Q(\Gamma)$	Γ	$Q(\Gamma)$
0	∞	8	1.12
1	15.68	9	1.11
2	3.72	10	1.02
3	1.56	11	0.94
4	0.94	12	0.93
5	0.77	13	0.98
6	0.83	14	1.04
7	0.99	15	1.06

* from Eq. (A28) and Ref. (59)

APPENDIX B

A TEST OF RAYLEIGH-GANS-DEBYE THEORY

APPENDIX B

A TEST OF RAYLEIGH-GANS-DEBYE THEORY

The ability to discriminate fibrous aerosol particles from near-spherical particles by light scattering depends upon a general property of the scattering of waves from long, thin objects, whose dimensions are of the order of a wavelength. Generally, there is a relative maximum of the scattered intensity in the forward direction. A "scattering plane" is one containing the directions of the incident beam and a scattered light ray. The angular width of the forward maximum in the scattering plane A containing the particle's long axis will be smaller than in the scattering plane perpendicular to A.

Because exact theories of light scattering by particles a few μm in size do not yield simple analytic expressions for the scattered intensity, one cannot deduce the general property above from these theories. Moreover, the testing of proposed instrumental designs mathematically, before their construction, is prohibitively expensive in computer time for the exact treatment of nonspherical particles. Both of these considerations lead one to consider approximate scattering theories in which the dependence of the forward-scattered intensity maximum upon the shape of the scatterer is clearly exhibited.

One of the simplest approximations to calculate, and one which implies a direct relationship between particle shape and the angular dependence of the forward-scattered intensity, is the Rayleigh-Gans-Debye (RGD) scattering theory (46, 47). This theory produces simple analytic expressions for the scattered intensity from prolate ellipsoids of revolution, which can be used to model asbestos fibers. In general, the scattered intensity in this theory measures the Fourier transform of the scatterer's shape (the "form factor") for a particular wave number. The RGD theory treats polarization effects only very crudely, but they are not relevant to the general effect we are discussing. The RGD theory is easily calculated with only small expenditures of computer time, and it has been,thus,used in preliminary designs of the aerosol fiber counter.

One of the difficulties in using the RGD theory to calculate the scattering from asbestos is that it is an approximation, and one that is intended for use in a different case. The essence of the RGD approximation is that the electric field in the interior of the scatterer is equated to its value without the particle present. For a dielectric particle of refractive index m and "radius" a, illuminated by light having wavenumber k, this amounts to requiring that the following two conditions be satisfied:

$$(m - 1) \ll 1 \qquad \text{(B1)}$$

and

$$2\, k\, a\, (m - 1) \ll 1. \qquad \text{(B2)}$$

While there is really little choice but to use the RGD theory for modeling, the light scattering from nonspherical aerosols, Eqs. (B1) and (B2) do not apply to the cases of interest in asbestos aerosols, where m is about 1.5, k is about 10 μm^{-1}, and a is about 1 μm. Fortunately, experience with a few particular cases has shown that the general property of the RGD theory needed for fibrous aerosol monitors, the dependence of the shape of the forward-scattering lobe on the size and shape of the particle, persists even when Eqs. (B1) and (B2) are invalid.

Until the last few years, the particular cases in which RGD predictions could be tested were limited to spherical particles, for which the exact Mie theory was available (46,47). In particular, the predictions of the RGD theory for the angular shape of the forward scattering lobe, as it depended on the radius of the scatterer, were compared with the exact results of the Mie theory in judging the usefulness of the RGD theory for the aerosol fiber-counter project (2). See, for example, Fig. 26 in Section 5. Generally, the RGD predictions of the shape of the forward lobe, as distinct from the absolute intensity, seemed to be valid for spheres having refractive indices of 1.5 and radii of 1 μm, at least to the extent needed for modeling an aerosol counter. Similar comparisons of the Fraunhofer diffraction theory of scattering, which also predicts a very simple relationship between the shape of the forward-scattering lobe and the size of a spherical scatterer, have been published recently (61).

For nonspherical particles little has been available until the last few years for checking the validity of any approximate theory. Now, however, two advances published in 1975 make it possible to calculate exact scattering solutions for homogeneous, nonspherical scatterers, appropriate to modeling asbestos fibers. The recent solution of the vector wave equation in spheroidal coordinates has permitted exact scattering calculations for oblate and prolate spheroids (62). Also, the extended-boundary-condition (EBCM) of Barber and Yeh now provides a numerical technique which can be applied to the scattering from arbitrarily shaped homogeneous objects (63).

In order to strenghten the case for using RGD theory to predict the angular shape of the forward lobe in light scattering from fibers, a subcontract was let to EMtec Engineering, Inc., of Los Angeles,California, to carry out selected calculations with the EBCM, under the direction of Dr. Cavour Yeh. These cases were chosen to be typical of important situations to be encountered in the scattering of light from aspherical particles in the fiber counter. Another comparison of EBCM calculations and RGD predictions has just been published by Barber and Wang (64). They were interested in modeling the scattering of light by biological cells immersed in water, where Eq. (B1) is indeed valid ($m = 1.05$), but Eq. (B2) is not. Nevertheless, several of their results, as well as the EMtec results, reinforce our conclusion that the RGD theory predicts the angular shape of the forward lobe of the scattering quite well, even in cases where the absolute magnitude of the RGD-predicted intensity is incorrect because the conditions for its validity are not met.

The EBCM calculations by Yeh *et al.* of EMtec treated the 14 cases listed in Table B1. Prolate spheroids were used because they are especially convenient to model fibers in the RGD theory. Two sizes of prolate spheriods were selected for each orientation, in order to demonstrate the dependence of the width of the forward lobe on fiber length, in one scattering plane. Two orientations were chosen for each of the sizes, which together provided a fair demonstration of the idea from RGD theory that the angular scattering pattern can be interpreted in terms of the Fourier transform of the particle shape. Oblate spheroids were treated in one orientation and two sizes, because the RGD theory predicts that flat plates, as well as fibers, may produce highly asymmetric scattering patterns. Finally, a prolate spheroid of 2:1 aspect ratio was used to examine the validity of RGD predictions for less asymmetric particles. Each of these seven scattering situations was analyzed for both horizontal and vertical incident polarizations. The nomenclature used to describe the scattering geometry in each case is defined in Fig. B1 and in the following discussion. The notation used here is similar to that of Barber and Yeh, (63) and Barber and Wang, (64) with the exception that we define the length of the symmetry axis to be 2a and the diameter to be 2b for all cases, whereas, Barber et al use 2a for the length of the major axis for both prolate and oblate shapes. The incident beam of light travels in the +z direction. The orientation of the symmetry axis of the spheroid can be specified by the single angle α, between the symmetry axis and the z axis, if the x-z plane is chosen to include these two lines ($-\frac{1}{2}\pi < \alpha < +\frac{1}{2}\pi$), as shown for a prolate spheroid in Fig. B1-A. The scattered light travels in a direction specified by the usual spherical coordinate angles, θ and ϕ, as shown in Fig. B1-B. The polarization is described as vertical when the electric field is normal to the scattering plane, and horizontal when the electric field lies in the scattering plane. For the cases considered in Table B1, symmetry requires that the scattered polarization be the same as the incident polarization.

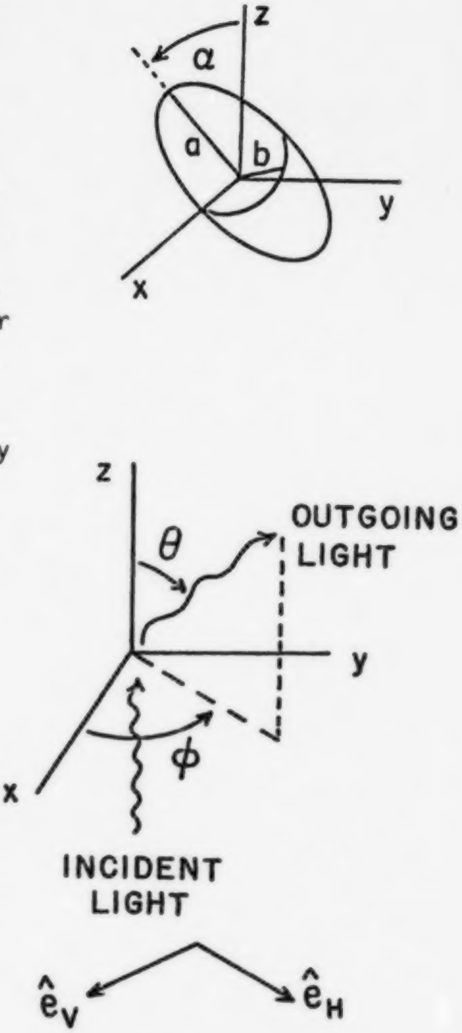

Fig. B1 Scattering Geometry

Because the operation of the fiber counter depends upon an effect that is not directly sensitive to polarization, and because the RGD theory does not even pretend to take proper account of polarization effects, the vertical and horizontal polarizations have been combined into a prediction of the scattering of unpolarized light. Thus, the EBCM cases A and C of Table B1 have been combined into a single prediction, case AC, for comparison with the RGD approximation. The RGD result is simple enough to present here in closed form as the differential scattering cross section: (46, 47)

(B3) $$\sigma = (2/9)\ a^2\ (k_0 b)^4\ (1 + \cos^2\theta)\ (m - 1)^2\ P(\theta,\phi),$$

where k_0 is the incident wave number and, for a spheroid oriented as in Fig. B1-A,

(B4) $$P(\theta,\phi) = \left[3\ (\sin u - u \cos)/u^3\right]^2 ,$$

(B5) $$u = 2\ k_0\ a\ \sin(\tfrac{1}{2}\theta)\ \left[\cos^2\beta + (b/a)^2 \sin^2\beta\right]^{\frac{1}{2}} ,$$

and

(B6) $$\cos\beta = -\cos\alpha\ \sin(\tfrac{1}{2}\theta) + \sin\alpha\ \cos(\tfrac{1}{2}\theta)\ \cos\phi .$$

The angle β in Eq. (B6) is the angle between the symmetry axis of the spheroid and the bisectrix of the scattering. The bisectrix is a line bisecting the angle between the scattering direction (θ,ϕ) and the backward direction $(\pi,0)$; it has angular coordinates $(\tfrac{1}{2}\theta + \tfrac{1}{2}\pi,\ \phi)$. In the RGD theory the scattered intensity is sensitive to the width of the particle in the direction of this bisectrix. When comparing various scattering directions having the same angle θ but differing angles in the forward lobe, the form factor $P(\theta,\phi)$ is a decreasing function of that width. It is this property upon which the shape discrimination of the fiber counter is based. If this effect persists, at least qualitatively, into the region of sizes and refractive indices relevant to fibrous aerosol counters, fiber discrimination by optical scattering is possible.

TABLE B1

EBCM CALCULATIONS OF SPHEROIDS*

Case	Symmetry Axis, 2a (μm)	Diameter 2b (μm)	Orientation α (degrees)	Incident Polarization V or H	Scattered Direction θ, ϕ (deg)
A	1.0	0.2	90	V	θ, 0
B	1.5	0.2	90	V	θ, 0
C	1.0	0.2	90	H	θ, 0
D	1.5	0.2	90	H	θ, 0
E	1.0	0.2	-45	V	θ, 0
F	1.5	0.2	-45	V	θ, 0
G	1.0	0.2	-45	H	θ, 0
H	1.5	0.2	-45	H	θ, 0
I	0.2	1.0	90	V	θ, 90
J	0.2	1.3	90	V	θ, 90
K	0.2	1.0	90	H	θ, 90
L	0.2	1.3	90	H	θ, 90
M	2.0	1.0	90	V	θ, 0
N	2.0	1.0	90	H	θ, 0

* In each case the index of refraction is 1.55, and the wavelength is 0.5 μm. Most of the cases (A, B, C, D, E, F, G, H, M, N) are prolate. Only four (I, J, K, L) are oblate spheroids.

The predictions of the RGD theory and the EBCM are compared, for seven cases of unpolarized incident radiation, in Fig. B2. In this figure the scattered intensity is plotted as the normalized cross section, following Barber et al. (63, 64). For prolate spheroids the normalized cross section is $(\sigma/\pi\ a^2)$, and for oblate spheroids it is $(\sigma/\pi\ b^2)$ in our notation. On these linear plots the features of the forward lobes, the peaks near $\theta = 0^0$, are emphasized, because the scattering for larger angles is quite small. For cases AC, BD, IK, JL, and MN, the forward lobe has mirror symmetry about 0^0 because of the special symmetry of the particle's orientation. If one concentrates on features that depend upon the shape of the forward lobe (i.e., the relative intensities at different angles), such as the angular width at half maximum, one finds fairly good agreement between the RGD predictions and the exact calculations. The agreement is better in general for small particles than for large, as one would expect from the nature of the RGD approximation. However, the agreement is also better for fibrous particles (cases AC, BD, EG, FH) than for flat particles (cases IK, JL) of for near spheres (case MN). Perhaps the thin, fibrous particles of this size range come closer to satisfying the condition of Eq. (B2), than do the thicker ones.

The data of Fig. B2 are reproduced in semilogarithmic plots in Fig. B3. These are useful for displaying similarities in the angular shapes of the forward lobes, because on a semilogarithmic scale two curves with the same functional form, except for a normalizing factor, appear to have the same shape, with only a relative vertical displacement. Adequate agreement between the RGD approximation and the exact EBCM calculations is indicated for our purposes in Fig. B3 if in the forward lobe the squares lie a constant distance above or below the continuous curve.

The agreement between the RGD approximation and the EBCM calculations for the small fiber of case AC is quite good; in fact, even the large-angle scattering looks quite similar in Fig. B3-case AC. The slightly longer fiber of case BD has a narrower forward lobe, as it should have, and a slightly more complicated scattering pattern in general. The backward peaks near 180^0 in RGD cases AC and BD correspond to a bisectrix at 90^0, the thin direction of the fiber for this orientation, and the EBCM calculations display a peak there also, although not as strikingly.

The cases EG and FH, for fibers having their axes at -45^{0} from the incident beam direction in the scattering plane, show that the idea of the scattered intensity's measuring the Fourier transform of the particle shape along the bisectrix direction has some validity even where Eqs. (B1) and (B2) do not hold. The slower falloff of the intensity with angle on the negative side of the beam (180-360^{0}) than on the positive side (0-180^{0}) is accounted for in the RGD theory by the fact that at a scattering angle of 315^{0} the bisectrix direction is along the minor axis of the spheroid, and it also seems to hold for the exact calculations.

The cases IK and JL show qualitative but less good agreement between the RGD and EBCM results for oblate spheroids. The width of the forward lobe does decrease with increasing particle dimension, but the RGD half-width seems to be consistently low.

The case MN was included to represent a token "near sphere" with an aspect ratio of only 2:1, and a rather large one. Here the two linear plots in Fig. B2, one with a full scale of 4 and the other with a full scale of 80, show that, despite the gross ratio of predicted absolute cross sections, the two forward lobes have more or less the same width. The semilogarithmic curves of Fig. B3, however, show that the detailed agreement between the RGD and EBCM predictions is very bad, for this case.

It would have been interesting to calculate more cases, but, given the results of those we have, it seems fair to say that for fibrous particles about one micron long the RGD approximation gives an adequate description of the scattering in the forward lobe, if one is interested primarily in ratios of intensities.

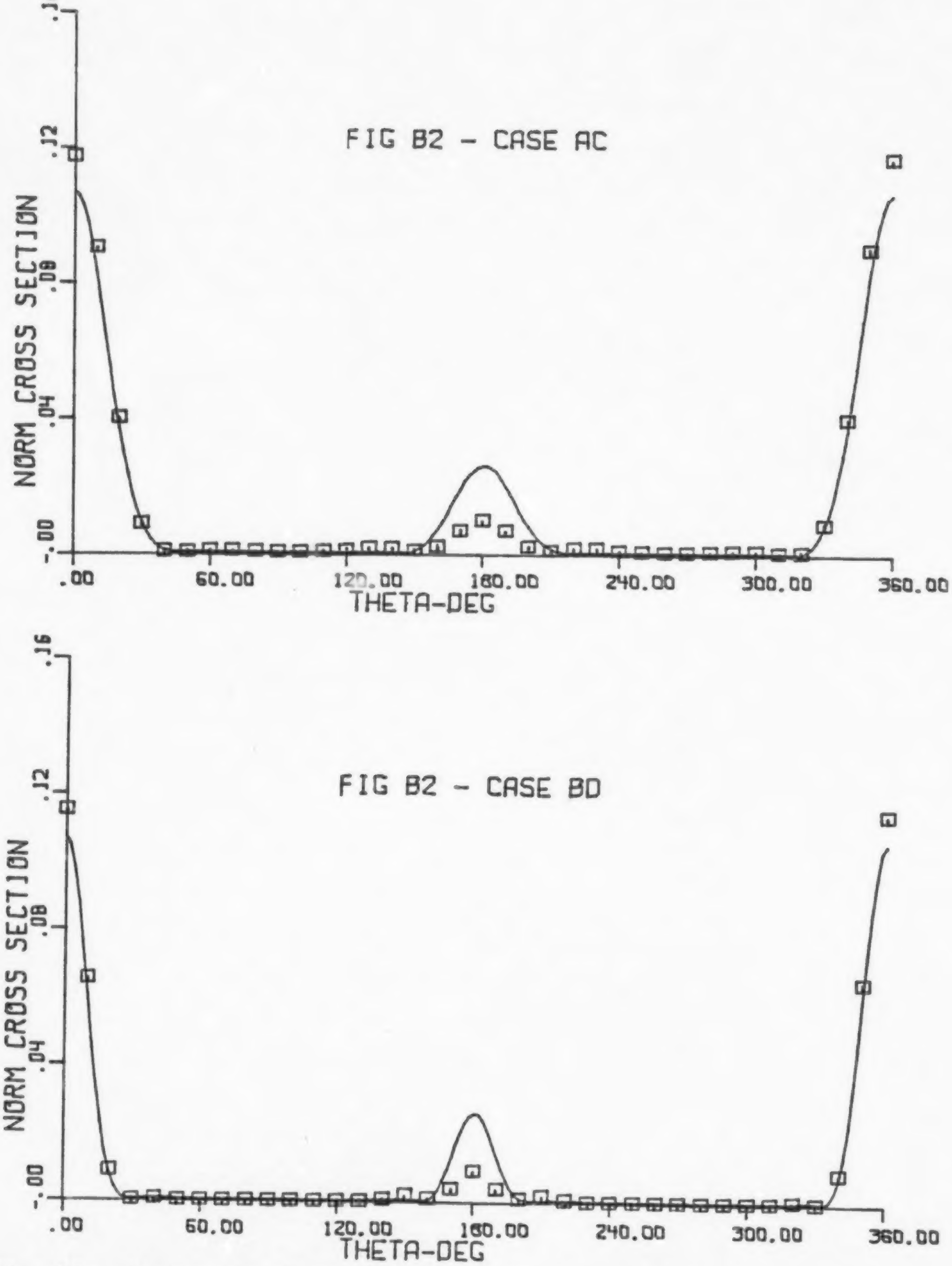

Fig. B2. Scattering of unpolarized light from spheroidal particles, for seven cases from Table B1. The lines give the RGD approximation, and the squares the exact EBCM calculations.

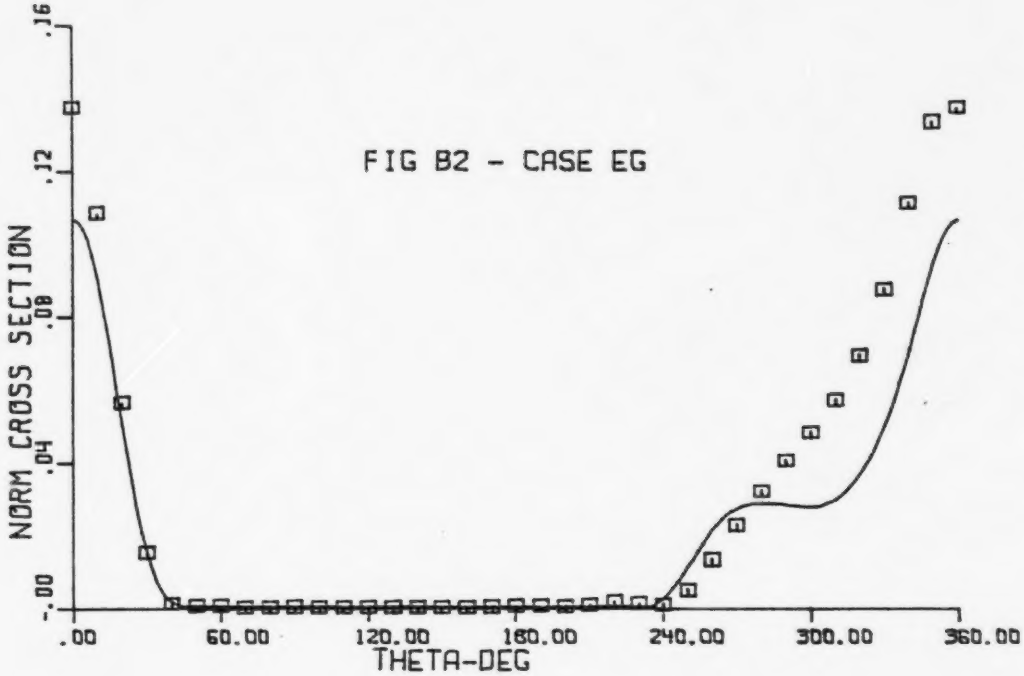

FIG B2 - CASE EG

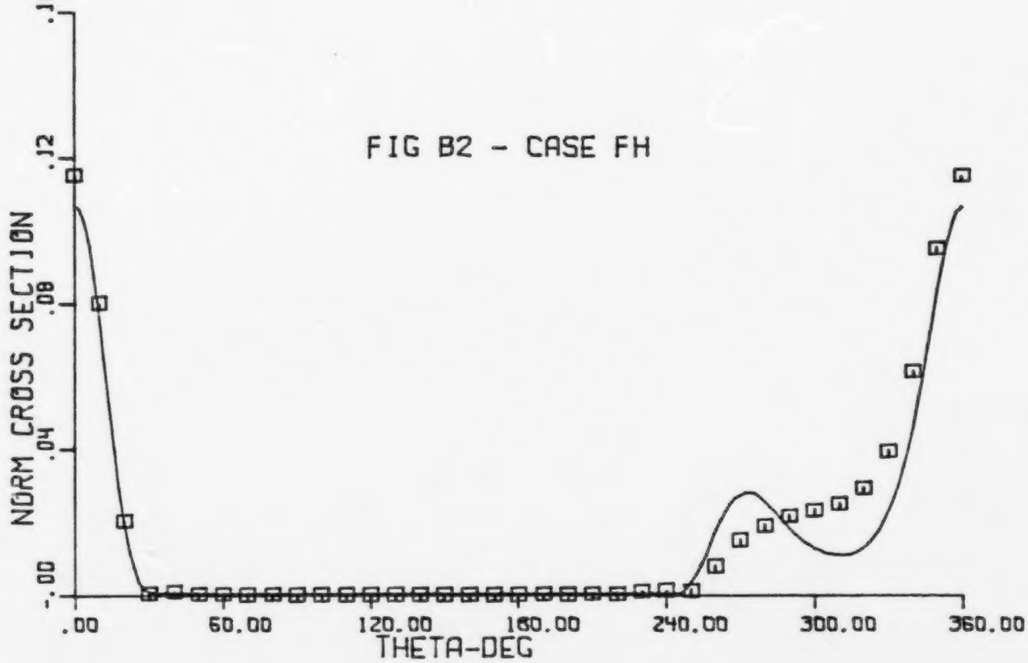

FIG B2 - CASE FH

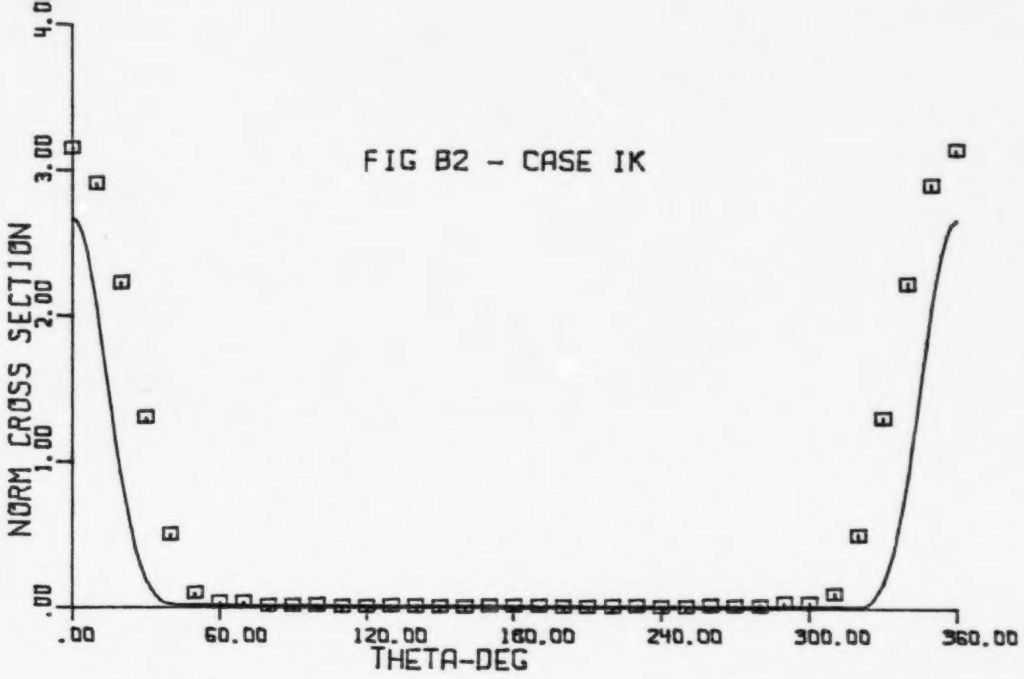

FIG B2 - CASE IK

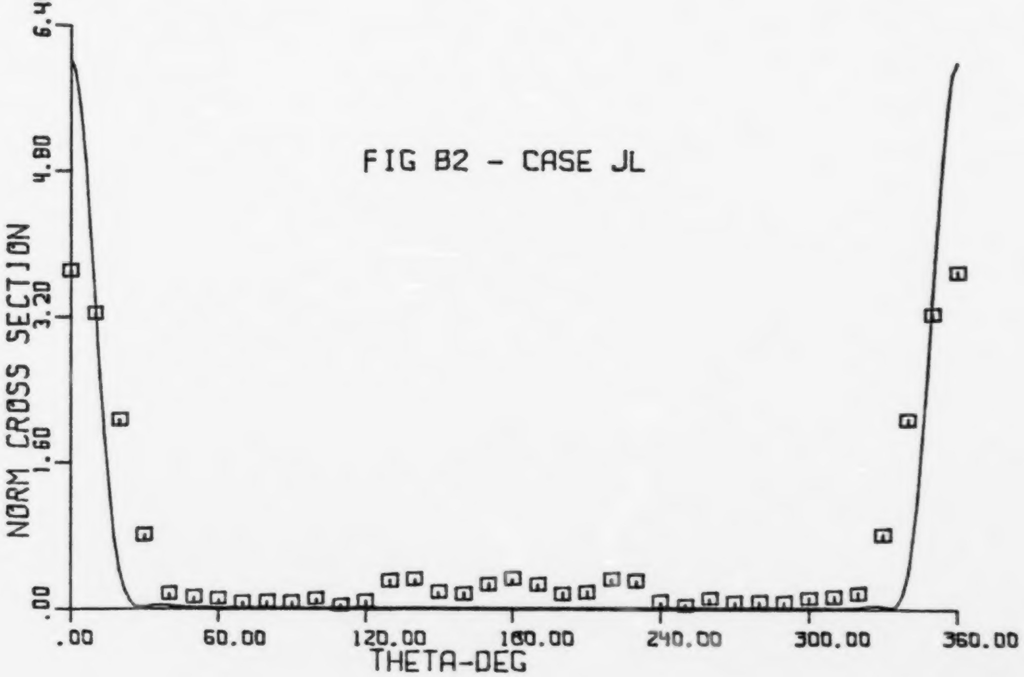

FIG B2 - CASE JL

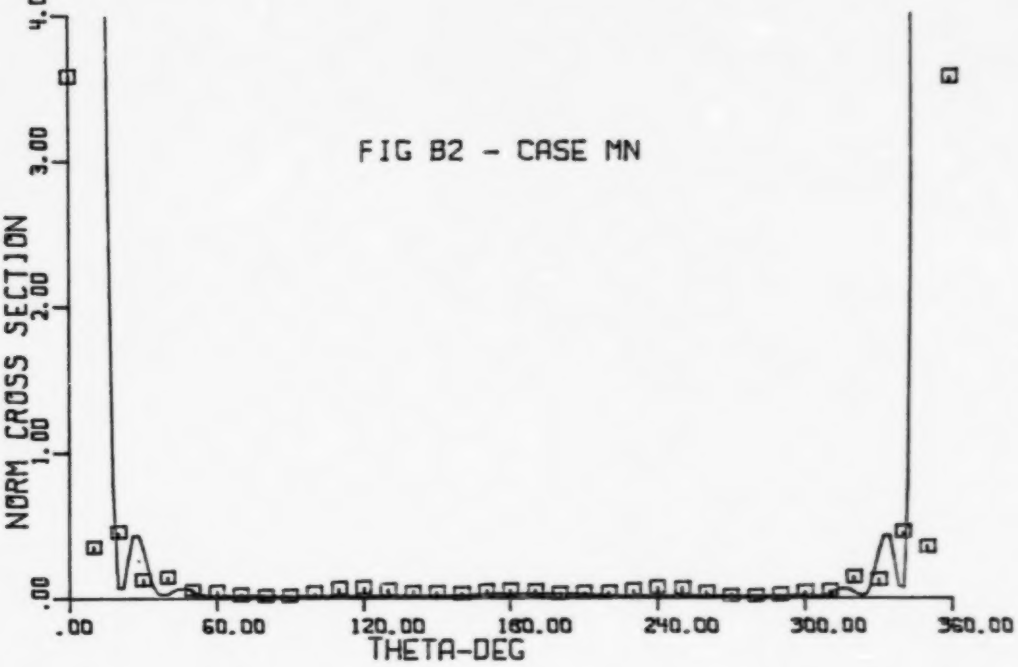
FIG B2 - CASE MN

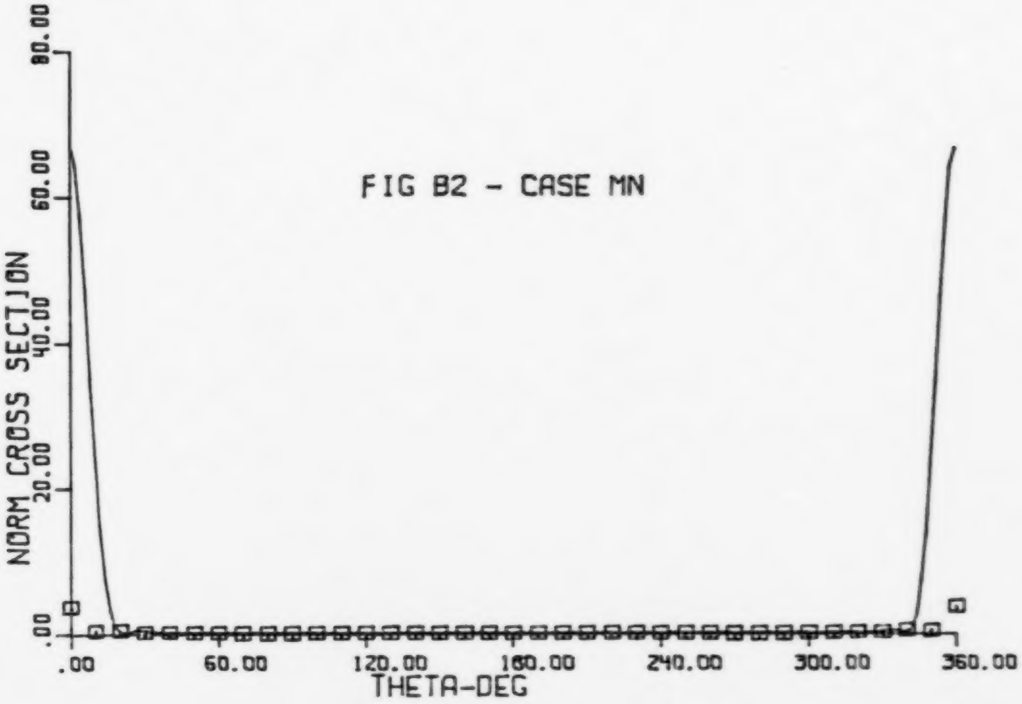
FIG B2 - CASE MN

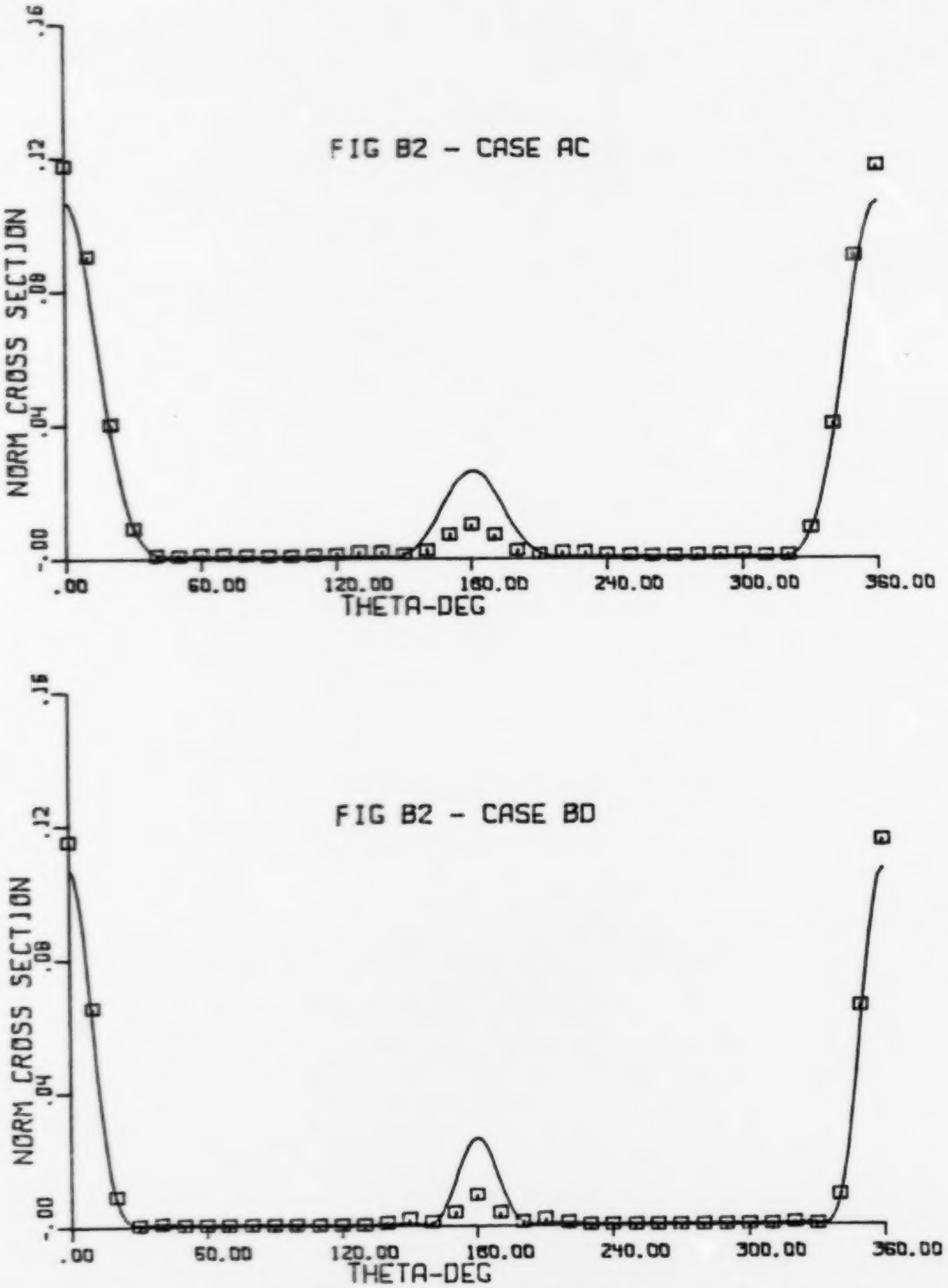

Fig. B3. A semilogarithmic comparison of the RGD approximation (lines) and the exact EBCM calculations (squares) for the same seven cases as in Fig. B2.

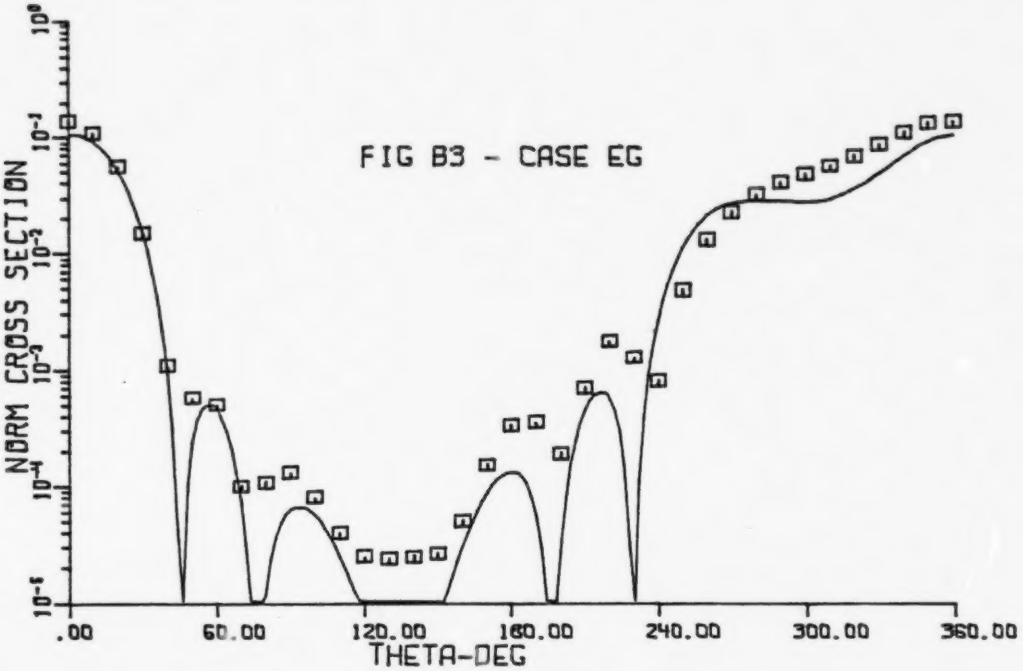
FIG B3 - CASE EG
NORM CROSS SECTION
10^{0}
10^{-1}
10^{-2}
10^{-3}
10^{-4}
10^{-5}
10^{-6}
.00
60.00
120.00
180.00
240.00
300.00
360.00
THETA-DEG

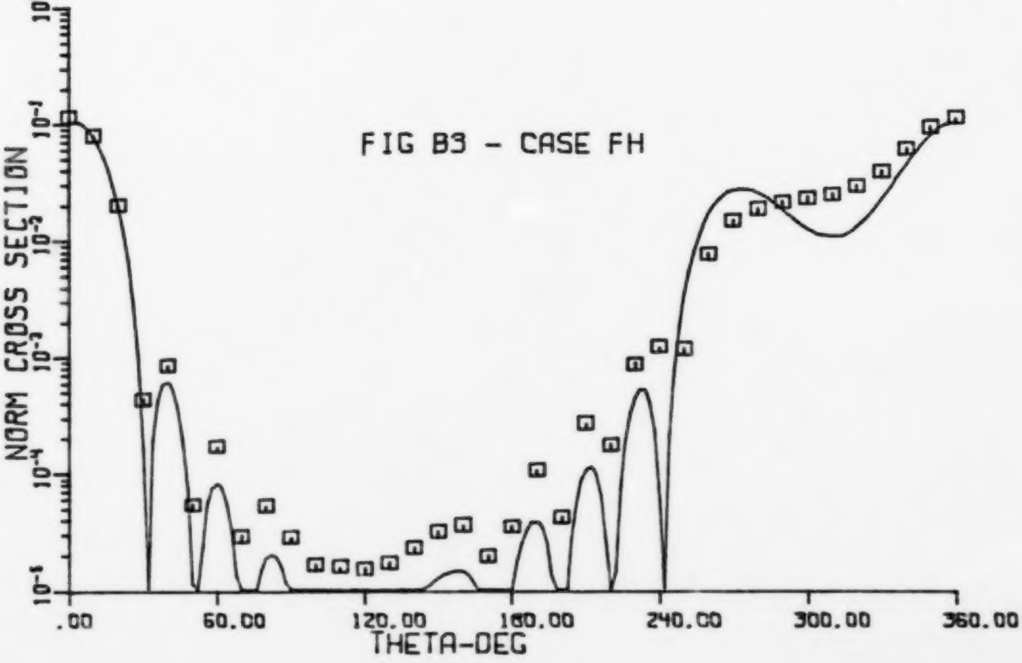
FIG B3 - CASE FH
NORM CROSS SECTION
10^{0}
10^{-1}
10^{-2}
10^{-3}
10^{-4}
10^{-5}
10^{-6}
.00
60.00
120.00
180.00
240.00
300.00
360.00
THETA-DEG

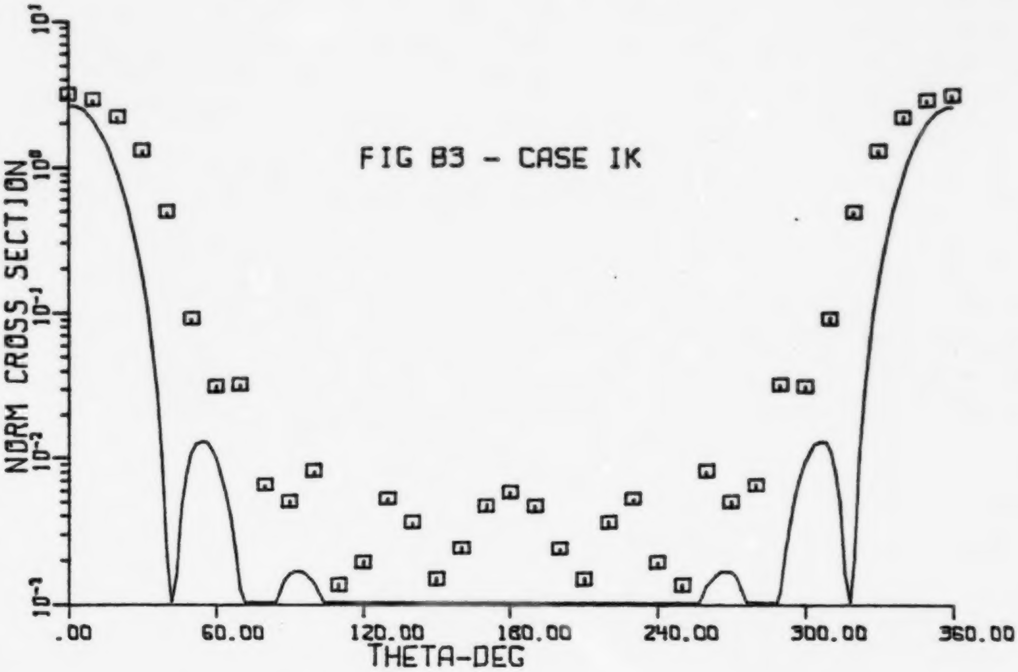

FIG B3 - CASE IK

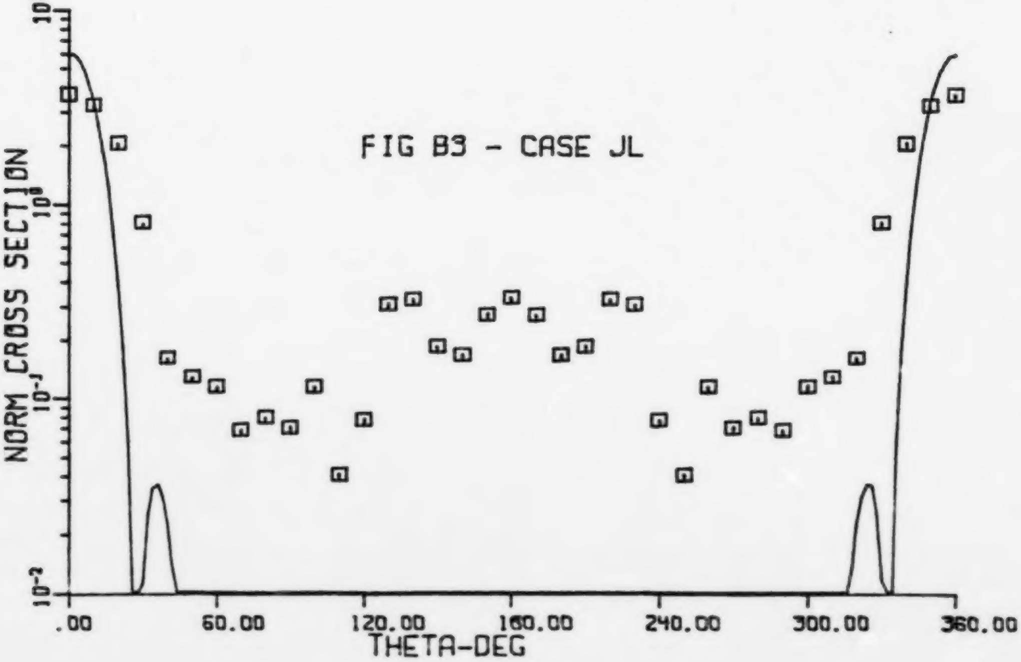

FIG B3 - CASE JL

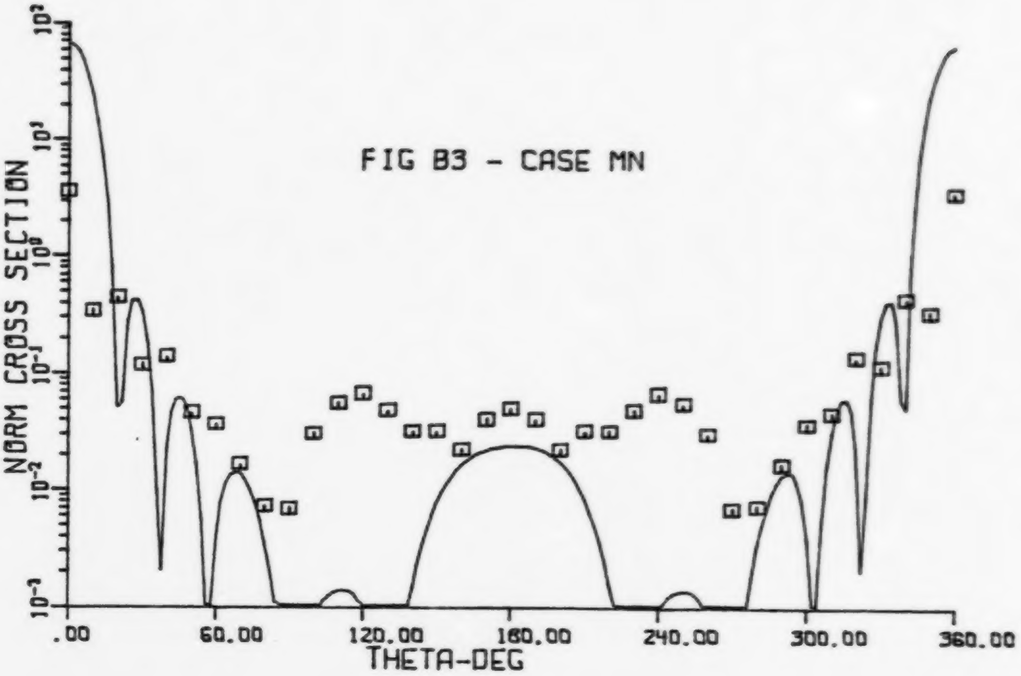

FIG B3 - CASE MN